QuantEXAFS: Bridging the gap between computational catalysis and XAS characterization communities using well-defined catalysts

By

RACHITA RANA

DISSERTATION

Submitted in partial satisfaction of the requirements for the degree of

DOCTOR OF PHILOSOPHY

in

Chemical Engineering

in the

OFFICE OF GRADUATE STUDIES

of the

UNIVERSITY OF CALIFORNIA

DAVIS

Approved:

Ambarish R. Kulkarni, Chair

Simon R. Bare

Bruce C. Gates

Coleman Kronawitter

Nir Goldman

Committee in Charge

2023

Dedicated to family and to ALL who supported and inspired.

CONTENTS

List of Figures

List of Tables

Abstract

QuantEXAFS: Bridging the gap between computational catalysis and XAS characterization communities using well-defined catalysts

The utilization of atomically dispersed catalysts (ADCs) is renowned for its ability to maximize metal efficiency and provide well-defined catalytic sites with increased uniformity. Although these advantages are commonly cited in the literature, a thorough investigation into the nature of these catalytic sites is imperative to comprehend their homogeneity and account for potential minority contributions. Typically, techniques such as scanning transmission electron microscopy (STEM) and x-ray absorption spectroscopy (XAS), along with additional methods like infrared spectroscopy (IR), are employed to study ADCs. While XAS is crucial for probing the local coordination environment, conventional analyses tools often yield averaged information rather than accurate specifics about these sites. Therefore, the development of methods that combine computational approaches with XAS becomes crucial for a comprehensive understanding of well-defined catalytic sites like ADCs, allowing for a more realistic assessment of their nature.

This project addresses a significant knowledge gap within the XAS literature by aiming to bridge the gap between the computational catalysis and experimental XAS communities. The outcome of my Ph.D. thesis work, the development of the QuantEXAFS method, serves as a significant contribution in bridging this gap. As the name suggests, QuantEXAFS is an automated tool designed for the quantitative analysis of EXAFS data, leveraging quantum chemistry tools such as density functional theory (DFT). This method was tested on various atomically dispersed catalysts, including platinum, and palladium supported on MgO, molybdenum, and platinum supported

on zeolites (ZSM-5). Ongoing studies involve applying QuantEXAFS to analyze reduced samples of atomically dispersed catalysts. This method not only eliminates user bias from conventional EXAFS fitting, thereby adding robustness to the approach, but it also facilitates fitting multiple scattering paths to longer ranges in R-space. QuantEXAFS has proven instrumental in identifying the true nature of catalytic sites by attributing realistic structures to experimental observations. This valuable information can be fed back into reaction barrier calculations and compared with experimentally observed results, such as apparent activation energy.

Moreover, QuantEXAFS extends its utility to quantify site heterogeneities in catalytic samples, we denote the name multi-site (MS) QuantEXAFS to this method. The incorporation of ab initio calculations into QuantEXAFS enables the theoretical calculation of Debye–Waller factors and facilitates their comparison. This enhancement contributes to the development of a comprehensive workflow for fitting EXAFS data, rendering it a more rigorous and accurate probe, particularly in the analysis of well-defined materials like atomically dispersed catalysts (ADCs).

Acknowledgments

In sincere appreciation, I extend my gratitude to Professors Ambarish Kulkarni and Simon Bare, whose unwavering guidance and support were instrumental throughout my Ph.D. Their encouragement as my Ph.D. advisors to explore new research directions and consistent efforts to enhance the quality of my work significantly contributed to my academic journey. I am deeply thankful for their mentorship, and I look forward to seeking their invaluable advice as I embark on future endeavors. Collaborating with and learning from Prof. Bruce Gates has been an enriching opportunity. Our interactions and discussions were not only stimulating but also provided valuable insights that greatly contributed to my academic growth. Additionally, I sincerely thank my other committee members, Prof. Coleman Kronawitter, and Dr. Nir Goldman, for their unwavering help and guidance throughout my Ph.D. This list is incomplete without Prof. Matteo Cargnello who has constantly challenged my thought process and helped me evolve as an experimentalist during my internship at Stanford. The collective support of all these mentors has been invaluable in shaping the trajectory of my research journey.

I would also like to express my appreciation to the entire Kulkarni Group at UC Davis – Chenghan, Artem, Jiawei, Trevor, Sudheesh, Saurabh, Kun-Lin, Rajat, Siddhartha, with special gratitude to Ty Sours and Sam Holton for their invaluable collaborations and assistance during my onboarding amidst the challenges of the COVID-19 pandemic.

The past few years with the Bare Group at SLAC have been remarkably enjoyable, filled with engaging discussions on project challenges and memorable group outings. Special thanks to Dr. Vila, Jiyun and Melissa for the insightful discussions. A big thanks to Adam Hoffman for his support, engaging in hour-long conversations on random science questions, patiently answering my inquisitive questions about beamline 10-2, and sharing insights about his favorite slide on the QuantEXAFS slide deck!

Another group that I'd like to thank is the Cargnello Group, specially, Baraa for helping me with the lab on-boarding, Chengshuang, Genni, Aruna, Sharadha, Pin-Hung and Steven for all the support. Another name to add to this list is, Yizhen for his contributions in conducting the experimental work that played a crucial role in testing QuantEXAFS during its initial phase. Special shoutout to Jorge for help in troubleshooting equipment issues during my experiments at SLAC. Niko has been an excellent lab buddy throughout the process of making atomically dispersed catalysts at UCD. I am also thankful to Prof. Sheima Khatib and Prof. Josh Howe for their valuable collaboration on the application of QuantEXAFS.

Thanks to the staff of the Chemical Engineering department for all their assistance. Specifically, thanks to Grace, Veronica, Bill, and, of course, Ryan. Sonali Das has been a great help with lab access, sharing beamtimes, and most importantly an incredible friend. Special thanks to Mellisa Mollaian for always being there.

Now on a more personal note, I extend my heartfelt thanks to my parents and entire family for their unwavering patience in understanding my career paths and passion for research. I am immensely grateful to Ms. Veronica Carvel, whose inspiration has left an indelible impact on shaping who I am today. A special appreciation goes to my constants– Deepali, Gill, Bose, Kritika, Avi, Kauser, Arvind, and everyone else. The list could go on, you know who you are. So, thank you all for everything!

Chapter 1

Introduction: Bridging the Gap between the X-ray Absorption Spectroscopy and the Computational Catalysis Communities in Heterogeneous Catalysis

Rachita Rana, Fernando D. Vila, Ambarish R. Kulkarni, Simon R. Bare

Some sections and figures for this chapter are adapted with permission from ACS Catal., 2022, 12, 13813–13830. Copyright 2023 American Chemical Society.

X-ray absorption spectroscopy (XAS) is a key technique within the heterogeneous catalysis community to probe the structure and properties of the active site(s)for a diverse range of catalytic materials. However, the interpretation of the raw experimental data to derive an atomistic picture of the catalyst requires modeling and analysis; the EXAFS data are compared to a model, and a goodness of fit parameter is used to judge the best fit. This EXAFS modeling can often be nontrivial and time-consuming; overcoming or improving these limitations remains a central challenge for the community. Considering these limitations, this chapter firstly, introduces the basics of XAS and DFT to the readers, secondly, it highlights how recent developments in analysis software, increased availability of reliable computational models, and application of data science tools can be used to improve the speed, accuracy, and reliability of EXAFS interpretation. In particular, this chapter emphasizes the advantages of combining theory and EXAFS as a unified technique that should be treated as a standard (when applicable) to identify catalytic sites and not two separate complementary methods. The goal of this chapter is provide a unified roadmap to foster collaborations between the theory and experimental catalysis communities and appreciate the applicability and scope of methods like QuantEXAFS.

This dissertation focuses on the merits of using and developing the QuantEXAFS workflow and its application to various atomically dispersed catalysts. This chapter will dive into the core concepts of XAS and DFT within the scope of QuantEXAFS and then Chapter 2 is the first application of QauntEXAFS workflow to platinum supported on MgO. Additionally, this chapter explains the details on categorization of EXAFS fit parameters by path in QauntEXAFS and all the related codes, databases of DFT-optimized structures used etc. Chapter 3, is another example of using QuantEXAFs and DFT calculation in direct combination with experimental characterizations. Furthermore, Chapter 4 will introduce the MS-QuantEXAFS apoach and its applicability in probing site heterogenities. Finally Chapter 5, offers my insights and reflections on the current state and future prospects of QuantEXAFS, providing a comprehensive overview of its implications and potential advancements. This chapter serves as a critical examination of the method's standing, bridging the gap between its present utility and the envisioned trajectory for further exploration in the field of catalysis and X-ray absorption spectroscopy.

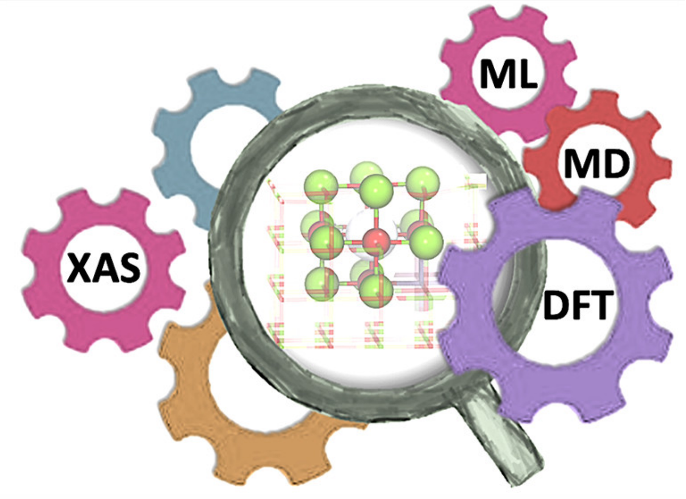

Figure 1.1. Concept of integrating theory and XAS

1.1 X-ray Absorption Spectroscopy and key concepts

Generation of core hole- When x-rays are incident on the sample and the energy of the x-ray is equal to or more than the binding energy of the electron (making XAS element specific) the electron in the atom is excited into higher energy orbitals that are unoccupied and then into continuum. Since this absorbed x-ray (1) is a photon, the excited electrons are called **photoelectron**.[1,2] The excitation of the electron creates an empty electron orbital called a hole and when these x-rays are energetic enough to excite a core-level electron (eg. 1s, 2s, 2p); a core-hole is generated. This excitation is short-lived (femto-seconds) and the core-hole is filled by an electron from a higher energy orbital of the absorbing atom. This transition happens with the release of energy alongside and this can be in the form of Auger emissions or fluorescence emissions or the formation of secondary electrons or photons.

Fluorescence radiation occurs when a core-hole is filled by an electron from a higher-energy orbital, releasing an X-ray. The energy of the emitted X-ray corresponds to the energy difference between the core-hole orbital and the orbital from which the electron jumps to fill the core-hole, making X-ray fluorescence energy element-specific. **Secondary electrons** or photons are emitted in a multi-step sequential filling of core-holes during the relaxation process, involving downward energy jumps of electrons between atomic shells.[2]

Auger electrons are generated when an electron from a higher-energy orbital fills the core-hole, leading to a subsequent energy loss and emission of another electron from the same or a different atomic shell. Forward and back scattering associated with the photoelectron is a significant phenomenon that underlies the origin of X-ray absorption fine structures (XAFS) in X-ray absorption spectroscopy (XAS). During X-ray incidence, a core hole is generated, and the presence of a neighboring atom causes the scattering of the photoelectron from the **absorber** to the neighboring atom and back-scattering to the absorbing atom. The returning photoelectron influences the amplitude of the photoelectron wave function, resulting in different measured absorption coefficients with and without these back-scattered photoelectrons. This comparison yields characteristic extended X-ray absorption fine structures (EXAFS), with oscillations caused by the interference of the photoelectron with itself due to neighboring atoms. Specifically, the EXAFS oscillations are due to quantum interference between the original outgoing photoelectron wave and parts of the wave which is backscattered from neighboring atoms. Also, the mean free path of the photoelectron makes EXAFS a probe of local structure. Constructive interference occurs when forward and backward scattering patterns are in-phase, leading to the peak of EXAFS spectra.[2]

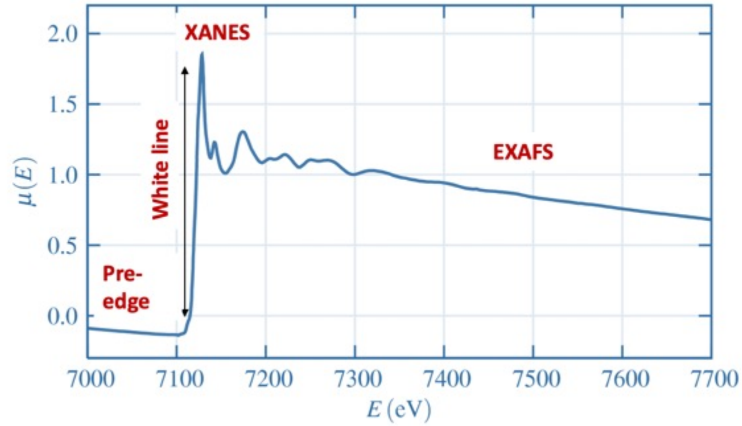

Figure 1.2. Regions of XAS spectra

1.1.1 X-ray Absorption Near Edge Structure

XANES is the part of the absorption spectra near the edge. XANES provides information about the electronic transitions and the local chemical environment of the absorbing atom. It is sensitive to the oxidation state, coordination geometry, and electronic structure of the absorbing atom. XANES region typically ranges from approximately -50 to +200 eV relative to the edge energy.Figure 1.2 shows the regions of XAS spectra.

1.1.2 Extended X-ray Absorption Fine Structure

The oscillatory part of the XAS spectrum is called Extended X-ray Absorption Fine Structure (EXAFS). EXAFS typically occurs beyond the absorption edge up to about 1000 eV or more. EXAFS spectral region is important to understand the local bonding environments of elements present in samples. This spectrum provides details about the types and quantities of atoms coordinating with the absorber atoms, the distances between them, and the level of disorder in their local molecular bonding (Figure 1.2). A simplisitic form of the EXAFS equation is shown in 1.1 below and all the terms are described. Additionally, the number of parameters defined in an EXAFS fit are governed by the Nyquist theorem Eq 1.4. Essentially, the theory used to correlate the amount of information in the original EXAFS signal to the information in Fourier transform spectrum is determined from the Nyquist theorem.

The EXAFS equation

$$\chi(k) = \frac{\chi_0(k)}{kR^2} \sum_j f_j(k) \exp[-2R_j/\lambda(k)] \cos[2kR_j + \delta_j(k)] \tag{1.1}$$

χ(k) is the EXAFS spectrum or the oscillatory part shown in Eq 1.2,

χ0(k) is the theoretical or normalized X-ray absorption spectrum,

k is the wave vector or the oscillation observed in EXAFS 1.3,

R is the interatomic distance,

f$_j(k)$ is the scattering amplitude,

λ(k) is the mean free path,

δ_j(k) is the phase shift.

$$\chi(k) = \frac{\mu(E) - \mu_0(E)}{\Delta\mu_0(E)} \tag{1.2}$$

$\mu(E)$ is the measured absorption coefficient, $\mu_0(E)$ is a smooth background function representing the absorption of an isolated atom, $\Delta\mu_0(E)$ is the measured jump in the absorption $\mu_0(E)$ at the threshold energy E_0.

$$k = \sqrt{\frac{2m(E - E_0)}{\hbar}} \tag{1.3}$$

E_0 is the absorption edge energy, m is the electron mass, $\hbar$ is the Plank's constant

$$N_{\mathrm{IP}} = \frac{2}{\pi}\Delta k \Delta R + 1 \tag{1.4}$$

N_{IP} is the number of independent points, Δk is the Fourier transformed data range, ΔR is the region used in EXAFS data analysis

1.2 Density Functional Theory

This dissertation predominantly features outcomes derived from atomistic simulations, employing Density Functional Theory (DFT) calculations. DFT aims to approximate solutions to the time-independent Schrödinger equation and is built upon the theorems provided by Kohn and Hohenberg. These theorems showcase that the ground state energy of a molecular system can be represented as a functional of electron density, thereby efficiently reducing the 3N dimensions of the Schrödinger equation to only three dimensions. To accomplish this, a set of single electron wave functions are solved ($\psi_i(r)$), these equations are known as the Kohn-Sham equations,[3]. Furthermore, through the minimization of this functional, the authentic electron density corresponding to the complete solution of the Schrödinger equation is acquired.

$$\left[\frac{-\hbar^2}{2m}\nabla^2 + V(r) + V_H(r) + V_{XC}(r)\right]\psi_i(r) = \epsilon_i \psi_i(r) \tag{1.5}$$

There are three potentials present in the Kohn-Sham Equation 1.5: $V(r)$, $V_H(r)$, and $V_{XC}(r)$. The first, $V(r)$ describes the interaction between each electron and the fixed atomic nuclei. The second potential known as the Hartree potential, describes the interactions between electrons using a mean-field approach that considers each electron interacting with the surrounding electron density at a given position r. Finally, the exchange-correlation potential ($V_{XC}(r)$), considers all additional quantum-mechanical effects and corrects for the self-interaction error in Hartree potential induced by the mean-field approximation (i.e., each electron is interacting with the surrounding electron density, which includes the electron itself).[3] $V_{XC}(r)$ potential is particularly significant to DFT, as many functionals exist of varying complexity that are more or less appropriate to use for a given atomic system(s). The class that only use the first derivative of the electron density in $V_{XC}(r)$ is known as the generalized gradient approximation (GGA), and many commonly used functionals are broadly labeled as GGAs. Hybrid functionals are more complicated forms of $V_{XC}(r)$ that consider electron exchange effects more rigorously than simple GGA.

1.3 Relevance of combining XAS and DFT

Owing to the inherent complexity of heterogeneous catalysts several complementary characterization approaches are routinely employed to probe the structure and properties of active site(s). Each piece of information is like a piece of a jigsaw puzzle, and it is only when we have most of the pieces assembled that we see the underlying picture clearly. There have been continued advances in these characterization techniques (especially transmission electron microscopy, nuclear magnetic resonance, and X-ray-based methods); their impact on catalysis science have been reviewed recently.[4–7] One such technique, X-ray absorption spectroscopy (XAS), has long held a strong foothold in the field.[8–17] This is due to the versatility of XAS to study a broad range of catalyst materials and reactions together with the wide geographic availability of XAS beamlines at synchrotrons (90 synchrotrons globally). These enablers, when combined with the ability of XAS to probe the local bonding environment of a specific element under reaction conditions, have resulted in XAS being applied to study a diverse range of heterogeneous catalysts. These include supported metal nanoparticles (including bimetallic), sub-nanometric clusters, atomically dispersed metals, and oxides, with supports that range from amorphous or semi-crystalline (e.g., carbon, silica, alumina, ceria and zirconia) to crystalline materials (e.g., zeolites, metal organic frameworks).[16–19]

In conjunction with other characterization techniques and kinetic measurements, XAS has played a prominent role in developing structure-property relationships and elucidating mechanistic pathways for various catalytic reactions.[20–24] Indeed, while X-ray absorption near edge structure (XANES) spectroscopy provides information about the electronic structure (e.g., the average oxidation state of a specific element in the experimental sample), extended X-ray absorption fine structure (EXAFS) spectroscopy probes the local bonding environment around the absorbing atom. Coupled with the easy ability to tune X-ray energies from 2 to 30 keV (covering the absorption edges of virtually all catalytically active elements) at the synchrotron, XAS is a versatile technique that is used to study a vast range of catalytic materials, including industrially relevant catalysts. The challenges and opportunities associated with using advanced XAS techniques for catalysis research have been recently reviewed.[6,24–27]

The underlying theory of EXAFS is well-established. As summarized in equation (1.1), the fine structure extracted from the experimentally measured spectrum is described as a sum of contributions of individual scattering paths to the overall signal. For a given set of scattering paths, "EXAFS modeling" involves identifying the values of the fitting parameters that minimize the error between the experiment and the modeled spectra.

The quality of experimental data and the associated uncertainties set an upper limit to the preciseness of the structural interpretation. However, depending on how the analysis is performed and the experimental sample of interest (e.g., uniform atomically dispersed vs. supported metal catalysts), one can access different degrees of information about the system. Thus, in addition to the technical aspects of data fitting (e.g., number of scattering paths, number of free variables, constraints used during fitting, etc.), the quality of an EXAFS interpretation depends significantly on the appropriateness of the models used for EXAFS analysis.[28]41

Depending on the specifics of the sample being analyzed, the EXAFS modeling procedure often results in non-integer coordination numbers. Although fractional coordination numbers are physically relevant for supported nanoparticle catalysts (as they represent the average coordination environment of all the metal atoms in the nanoparticle), such analyses have now become routine to determine the coordination environment of the metal in single atom catalysts (SACs).[29–31] As practiced today, the EXAFS analysis procedures are material-agnostic, i.e., similar fitting approaches and quality-of-fit metrics are used to study supported metal, zeolite, metal-organic framework, and SACs. As the nature of the active sites (e.g., isolated cations in SACs vs. step or terrace sites for metal nanoparticles) are inherently different among the various catalyst classes, it is useful to consider if developing material-specific EXAFS analysis approaches may be advantageous within the community 1.3.

Notwithstanding the shortcomings summarized above, there is no question that EXAFS analysis has been and will continue to be a cornerstone in our understanding of the structure of catalytically active sites. Specifically, even in its current form, EXAFS remains one of the most valuable techniques that provides quantitative information about averaged local coordination environment for the chosen element, especially under operating conditions of temperature, pressure, and gas flow or applied potential. However, as illustrated in Figure 1.4, various factors such as presence of multiple sites, anisotropy within similar sites, thermal effects, and particle size effects can contribute to non-uniformity of the bonding environments. Since the complexities of the experimental sample are typically not known a priori, it may be difficult using conventional EXAFS analysis by itself to determine the uniformity (or lack thereof) of the coordination environment.

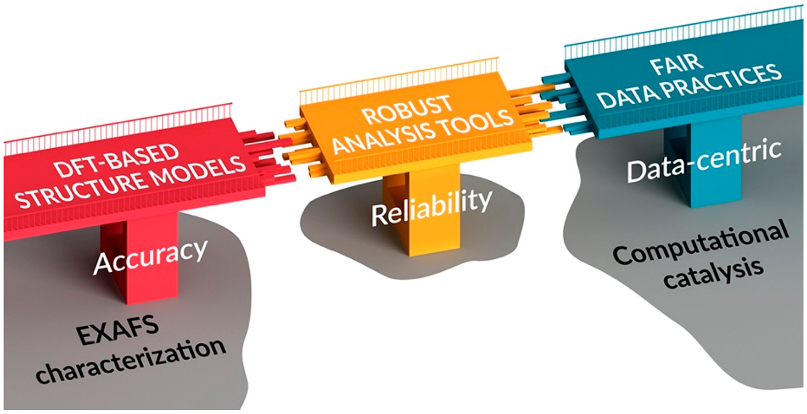

Figure 1.3. Bridging the gap between the computational catalysis and the EXAFS characterization communities to address the complexities associated with identifying active sites for various heterogeneous catalysts.

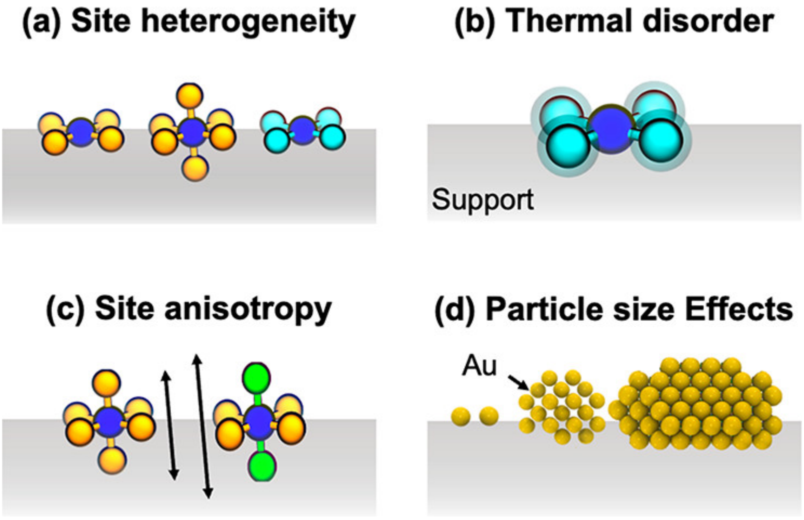

Figure 1.4. Experimental EXAFS measures the averaged coordination environment of an absorbing atom (blue). The averaged information may arise due to (a) heterogeneity of the sites due to differences in the number and/or type of neighboring atoms (denoted as yellow or cyan), (b) thermal vibrational effects, (c) anisotropy within similar sites (axial green atoms form a longer bond than the yellow neighbors), and (d) particle size effects (Au nanoparticle is shown as an example).

1.4 Example method for using DFT and XAS to identify catalytic sites

QuantEXAFS is theory-guided Python-based EXAFS analysis approach that uses the open-source Larch software for EXAFS preprocessing, analysis and fitting.[32] This method begins by creating an exhaustive database of DFT-optimized structures that can be used to model the experimental EXAFS.[33,34] While uniform atomically dispersed catalysts are more amenable by QuantEXAFS, this approach has been extended to more complex systems such as Pt/ZSM-5.[35] Although questions about the uniformity of the proposed Pt^{2+} site remain open, a key advantage of QuantEXAFS is the ability to compare the modeled EXAFS spectra of different types of sites (e.g., all possible Pt^{2+} vs. all possible $[PtOH]^{1+}$) rather than only considering a few plausible configurations. Figure 1.5 illustrates a set of categories that are discussed in the perspective article from which excepts for this section are taken. Where each category is compared on the basis of scalabilty of the EXAFS fitting approach and the specificity of the model used for fitting the EXAFS data.

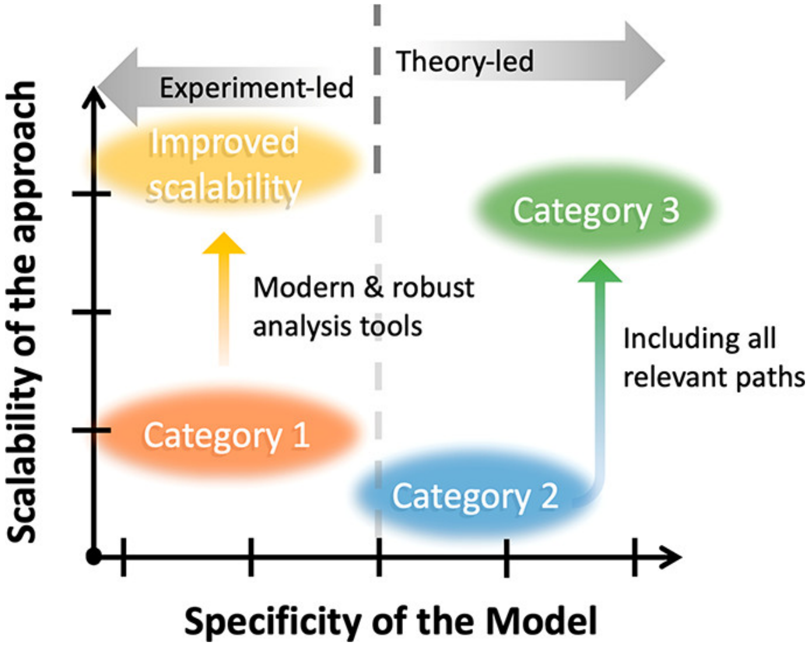

Figure 1.5. Two criteria (i.e., specificity of the model derived from EXAFS analysis and scalability of the fitting approach) are used to classify the published EXAFS literature into three distinct categories. While Category 1 studies provide structural information using conventional EXAFS fitting, both Category 2 and 3 studies use DFT-derived structures. The gray arrows emphasize that the role of theory depends significantly on the class of materials being investigated..

Overall, the evolution of EXAFS from the conventioanl two-step model (i.e., data collection step followed by model fitting and interpretation) to a real-time characterization technique may have far reaching impacts on the field of heterogeneous catalysis. Indeed, while structure-function relationships are well-established, less attention has been focused on elucidating the mechanism of catalyst synthesis. Recognizing that the overlap between of EXAFS analysis and theory (both DFT and machine learning) is especially well-suited for studying precisely synthesized materials, Figure 1.6 motivates one such interdisciplinary challenge for the researchers studying atomically dispersed catalysts.[36]

The heterogeneous catalysis community needs to identify challenging questions that can perhaps be addressed by combining the advances in XAS experiments and the continued collaborations with the theorists. Based on the recent developments in this arena, I am are confident that the next decade will provide unprecedented insights into physiochemical phenomena that currently remain inaccessible. Figure 1.6 represents the future perspective of combining theory and XAS for a data-centric future of catalysis.

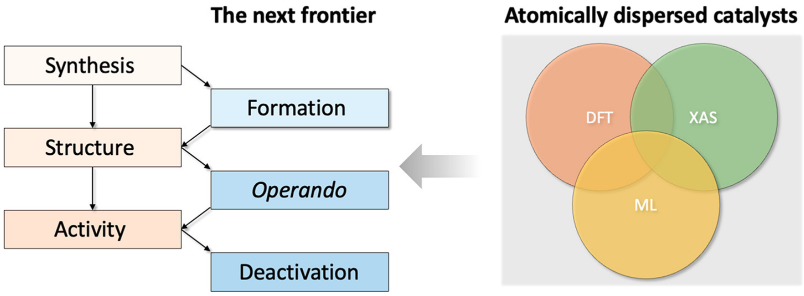

Figure 1.6. The advances in X-ray absorption spectroscopy, machine learning and density functional theory can be combined to elucidate the synthesis-structure-activity relationships for atomically dispersed materials.

1.5 References

[1] Mathew Newville. *Fundamental of XAFS.* Consortium for Advanced Radiation Sources University of Chicago, Chicago, IL, 2004.

[2] Ravel Bruce, Dean Hesterberg, and Shelly Kelly. *Analysis of Soils and Minerals Using X-ray Absorption Spectroscopy.* Soil Science Society of America, 2008.

[3] David S. Sholl and Janice A. Steckel. *Density Functional Theory: A Practical Introduction.* John Wiley & Sons, 2009.

[4] Peter Tieu, Xingxu Yan, Mingjie Xu, Phillip Christopher, and Xiaoqing Pan. Directly probing the local coordination, charge state, and stability of single atom catalysts by advanced electron microscopy: A review. *Small*, 17:2006482, 2021.

[5] Christopher Gordon, Lukas Lätsch, and Christophe Copéret. Nuclear magnetic resonance: A spectroscopic probe to understand the electronic structure and reactivity of molecules and materials. *J. Phys. Chem. Lett.*, 12:2072, 2021.

[6] Yiunan Xia, Charles T. Campbell, Beatriz Roldan Cuenya, and Manos Mavrikakis. Introduction: Advanced materials and methods for catalysis and electrocatalysis by transition metals. *Chem. Rev.*, 121:563, 2021.

[7] Xuning Li, Xiaofeng Yang, Junming Zhang, Yanqiang Huang, and Bin Liu. In situ/operando techniques for characterization of single-atom catalysts. *ACS Catal.*, 9:2521, 2019.

[8] Atsushi Beniya and Shougo Higashi. Towards dense single-atom catalysts for future automotive applications. *Nat. Catal.*, 2:590, 2019.

[9] Manoj B Gawande, Paolo Fornasiero, and Radek Zbořil. Carbon-based single-atom catalysts for advanced applications. *ACS Catal.*, 10:2231, 2020.

[10] Mi Yoo, Young-Sang Yu, Hyunwoo Ha, Siwon Lee, Jin-Seok Choi, Sunyoung Oh, Eunji Kang, Hyuk Choi, Hyesung An, Kug-Seung Lee, Jeong Young Park, Richard Celestre, Matthew A. Marcus, Kasra Nowrouzi, Doug Taube, David A. Shapiro, WooChul Jung, Chunjoong Kim, and Hyun You Kim. A tailored oxide interface creates dense pt single-atom catalysts with high catalytic activity. *Energy Environ. Sci.*, 13:1231, 2020.

[11] Yuanyuan Li, Matthew Kottwitz, Joshua L. Vincent, Michael J. Enright, Zongyuan Liu, Lihua Zhang, Jiahao Huang, Sanjaya D. Senanayake, Wei-Chang D. Yang, Peter A. Crozier, Ralph G. Nuzzo, and Anatoly I. Frenkel. Dynamic structure of active sites in ceria-supported pt catalysts for the water gas shift reaction. *Nat. Commun.*, 12:1, 2021.

[12] Lingzhe Fang, Soenke Seifert, Randall E. Winans, and Tao Li. Operando xas/saxs: Guiding design of single-atom and subnanocluster catalysts. *Small Methods*, 5:2001194, 2021.

[13] Joaquin Resasco, Leo DeRita, Sheng Dai, Joseph P Chada, Mingjie Xu, Xingxu Yan, Jordan Finzel, Sergei Hanukovich, Adam S Hoffman, George W Graham, Simon R Bare, Xiaoqing Pan, and Phillip Christopher. Uniformity Is Key in Defining Structure–Function Relationships for Atomically Dispersed Metal Catalysts: The Case of Pt/CeO2. *Journal of the American Chemical Society*, 142 (1):169–184, jan 2020. doi: 10.1021/jacs.9b09156.

[14] Max J. Hülsey, Bin Zhang, Zhirui Ma, Hiroyuki Asakura, David A. Do, Wei Chen, Tsunehiro Tanaka, Peng Zhang, Zili Wu, and Ning Yan. In situ

spectroscopy-guided engineering of rhodium single-atom catalysts for co oxidation. *Nat. Commun.*, 10:1330, 2019.

[15] Bidyut B Sarma, Philipp N Plessow, Giovanni Agostini, Patricia Concepción, Norbert Pfänder, Liqun Kang, Feng R Wang, Felix Studt, and Gonzalo Prieto. Metal-Specific Reactivity in Single-Atom Catalysts: CO Oxidation on 4d and 5d Transition Metals Atomically Dispersed on MgO. *Journal of the American Chemical Society*, 142(35):14890–14902, sep 2020. doi: 10.1021/jacs.0c03627.

[16] Maxwell W. Terban, Sanjit K. Ghose, Anna M. Plonka, Diego Troya, Pavol Juhás, Robert E. Dinnebier, John J. Mahle, Wesley O. Gordon, and Anatoly I. Frenkel. Atomic resolution tracking of nerve-agent simulant decomposition and host metal–organic framework response in real space. *Commun. Chem.*, 4:2, 2021.

[17] Sami Malola, Paavo Nieminen, Antti Pihlajamäki, Joonas Hämäläinen, Tommi Kärkkäinen, and Hannu Häkkinen. A method for structure prediction of metal-ligand interfaces of hybrid nanoparticles. *Nat. Commun.*, 10:3973, 2019.

[18] Henry J. Sokol, Amani M. Ebrahim, Stavros Caratzoulas, Anatoly I. Frenkel, and Julia A. Valla. In situ xafs, xrd, and dft characterization of the sulfur adsorption sites on cu and ce exchanged y zeolites. *J. Phys. Chem. C*, 126:1496, 2022.

[19] Lichen Liu and Avelino Corma. Metal catalysts for heterogeneous catalysis: From single atoms to nanoclusters and nanoparticles. *Chem. Rev.*, 118:4981, 2018.

[20] Seok Ki Kim, Hyun Woo Kim, Seung Ju Han, Sung Woo Lee, Jungho Shin, and

Yong Tae Kim. Mechanistic and microkinetic study of non-oxidative methane coupling on a single-atom iron catalyst. *Commun. Chem.*, 3:1, 2020.

[21] Eduardo Valle, Melis Duyar, Jonathan Snider, Samuel Regli, Magnus Rønning, Alessandro Gallo, and Thomas F. Jaramillo. In situ studies of the formation of mop catalysts and their structure under reaction conditions for higher alcohol synthesis: The role of promoters and mesoporous supports. *J. Phys. Chem. C*, 126:5575, 2022.

[22] Jiaqi Li, Anusheela Das, Qing Ma, Michael J. Bedzyk, Yosi Kratish, and Tobin J. Marks. Diverse mechanistic pathways in single-site heterogeneous catalysis: Alcohol conversions mediated by a high-valent carbon-supported molybdenum-dioxo catalyst. *ACS Catal.*, 12:1247, 2022.

[23] Hongfei Ma, Yalan Wang, Hao Zhang, Guoyan Ma, Wei Zhang, Yanying Qi, Terje Fuglerud, Zheng Jiang, Weiping Ding, and De Chen. Facet-induced strong metal chloride–support interaction over cucl 2 /γ-al 2 o 3 catalyst to enhance ethylene oxychlorination performance. *ACS Catal.*, 12:8027, 2022.

[24] Jingzheng Zhang, Bing An, Zhe Li, Yonghua Cao, Yiheng Dai, Wangyang Wang, Lingzhen Zeng, Wenbin Lin, and Cheng Wang. Neighboring zn-zr sites in a metal-organic framework for co2hydrogenation. *J. Am. Chem. Soc.*, 143:8829, 2021.

[25] Andrea Di Cicco, Gabriele Giuli, and Angela Trapananti. Synchrotron radiation science and applications. *Springer:Cham.*, 220:5846, 2021.

[26] Manoj B. Gawande, Katsuhiko Ariga, and Yusuke Yamauchi. Single-atom catalysts. *Small*, 17:2101584, 2021.

[27] Giovanni Di Liberto, Luis A. Cipriano, and Gianfranco Pacchioni. Universal principles for the rational design of single atom electrocatalysts? handle with care. *ACS Catal.*, page 5846, 2022.

[28] Yasuhiro Iwasawa, Kiyotaka Asakura, and Mizuki Tada. *XAFS Techniques for Catalysts, Nanomaterials, and Surfaces*. SpringerInternationalPublishing, 2021.

[29] Adriano Filipponi and Anrea Di Cicco. Gnxas: A softwear packega for advanced exafs miltiple-scattering calculations and data analysis. *Task Q.*, 4:575, 2000.

[30] Janis Timoshenko and Beatriz Roldan Cuenya. In situ/ operando electrocatalyst characterization by x-ray absorption spectroscopy. *Chem. Rev.*, 121:882, 2021.

[31] Edward A. Stern, Dale E. Sayers, and Farrel W. Lytle. Extended x-ray-absorption fine-structure technique. iii. determination of physical parameters. *Phys. Rev. B*, 11:4836, 1975.

[32] Mathew Newville. Larch: An analysis package for xafs and related spectroscopies. *J. Phys. Conf. Ser.*, 430:012007, 2013.

[33] Yizhen Chen, Rachita Rana, Tyler Sours, Fernando D. Vila, Shaohong Cao, Thomas Blum, Jiyun Hong, Adam S. Hoffman, Chia-Yu Fang, Zhennan Huang, Chunyan Shang, Chuanhao Wang, Jie Zeng, Miaofang Chi, Coleman X. Kronawitter, Simon R. Bare, Bruce C. Gates, , and Ambarish R. Kulkarni. A theory-guided x-ray absorption spectroscopy approach for identifying active sites in atomically dispersed transition-metal catalysts. *J. Am. Chem. Soc.*, 143 (48):20144–20156, 2021. doi: 10.1021/jacs.1c07116.

[34] Yizhen Chen, Rachita Rana, Zhennan Huang, Fernando D. Vila, Tyler Sours, Jorge E. Perez-Aguilar, Xiao Zhao, Jiyun Hong, Adam S. Hoffman, Xu Li,

Chunyan Shang, Thomas Blum, Jie Zeng, Miaofang Chi, Miquel Salmeron, Coleman X. Kronawitter, Simon R. Bare, Ambarish R. Kulkarni, and Bruce C. Gates. Atomically dispersed platinum in surface and subsurface sites on mgo have contrasting catalytic properties for co oxidation. *J. Phys. Chem. Lett.*, 2022. doi: 10.1021/acs.jpclett.2c00667.

[35] Noah Felvey, Jiawei Guo, Rachita Rana, Le Xu, Simon R. Bare, Bruce C. Gates, Alexander Katz, Ambarish R. Kulkarni, Ron C. Runnebaum, and Coleman X. Kronawitter. Interconversion of atomically dispersed platinum cations and platinum clusters in zeolite zsm-5 and formation of platinum gem-dicarbonyls. *J. Am. Chem. Soc.*, 144:13874, 2022.

[36] Rachita Rana, Fernando D. Vila, Ambarish R. Kulkarni, and Simon R. Bare. Bridging the gap between the x-ray absorption spectroscopy and the computational catalysis communities in heterogeneous catalysis: A perspective on the current and future research directions. *ACS Catalysis*, 12(22):13813–13830, 2022.

Chapter 2

A Theory-Guided X-ray Absorption Spectroscopy Approach for Identifying Active Sites in Atomically Dispersed Transition-Metal Catalysts

Y. Chen[#], R. Rana[#], T. Sours[#], F. D. Vila, S. Cao, T. Blum, J. Hong, A. S. Hoffman, C.-Y. Fang, Z. Huang, C. Shang, C. Wang, J. Zeng, M. Chi, C. X. Kronawitter, S. R. Bare, B. C. Gates and A. R. Kulkarni

[#]Authors contributed equally. My contributions to this work consist of theoretical predictions of the EXAFS and XANES spectra simulations – Figures 2.1, 2.4, 2.5, 2.6 and Tables 2.1, 2.2. All experimental work was performed by collaborators and the reaction barriers and phase diagrams were calculated by T. Sours.

Adapted with permission from J. Am. Chem. Soc., 2021, 143, 20144–20156.

2.1 Abstract

Atomically dispersed supported metal catalysts offer new properties and the benefits of maximized metal accessibility and utilization. The characterization of these materials, however, remains challenging. Using atomically-dispersed Pt supported on crystalline MgO (chosen for its well-defined bonding sites for Pt) as a prototypical example, in this work, we show how high-throughput density functional theory cal-

culations (for assessing all the potentially stable Pt sites) combined with automated EXAFS analysis can lead to unbiased identification of isolated, surface-enveloped platinum cations as the catalytic species for CO oxidation. The catalyst has been characterized by atomic-resolution imaging, EXAFS, and HERFD-XANES spectroscopies; the proposed Pt site are in full agreement with experiment. This theory-guided workflow leads to rigorously determined structural models and provides a more detailed picture of the structure of the catalytically active sites than what is currently possible with conventional EXAFS analysis. As this approach is efficient and agnostic to the metal, support, and catalytic reaction, we posit that it will be of broad interest to the materials characterization and catalysis communities.

2.2 Introduction

Atomically dispersed metals on reducible (CeO_2, TiO_2, Fe_3O_4) and nonreducible (Al_2O_3, MgO, ZrO_2) metal oxide supports have drawn wide attention recently as catalysts for a wide range of reactions including CO oxidation, water-gas shift, and other oxidations and reductions.[1–8] These catalysts offer the advantages of maximum accessibility of the metals, which are often expensive (e.g., Pt, Pd, Ir, Rh), and catalytic properties distinct from those of the conventional supported metal clusters and nanoparticles. Like most single transition metal (TM) atoms in organometallic complexes, those on metal oxide supports are positively charged, having properties that are strongly influenced by their surroundings.[9–12] These surroundings (bonding environments) are challenging to identify, because the support surfaces are inherently heterogeneous. Even when the most incisive experimental methods are used (e.g., aberration corrected scanning transmission electron microscopy (STEM), X-ray absorption spectroscopy (XAS), and probe molecule experiments with spectroscopies), the results often provide only average structural models of the dominant metal bonding environment; the possible contributions of minority catalytic species are often overlooked.[13] Common research approaches involve using experimentally determined structure parameters (e.g., bond lengths and coordination numbers from extended x-ray absorption fine structure (EXAFS) spectroscopy) with complementary information characterizing local geometry and electronic structure from x-ray absorption near-edge structure (XANES) spectra. These techniques are often combined to create plausible atomistic models that are subsequently investigated using density functional theory (DFT) calculations to derive quantitative structural and mechanistic insights.[7,14,15] More recent approaches have utilized machine learning techniques to gain structural information.[16] We emphasize that, as conventionally practiced, the initial development of atomistic models relies predominantly on thorough EXAFS modeling, which is often quite demanding and time intensive for the user, especially when multiple scattering paths are considered. Today's "hands-on" EXAFS modeling approaches fall short of determining the existence of multiple metal bonding environments—a central limitation in the field. Moreover, structures inferred for the sites may not be consistent with all the complementary experimental results. As atomically dispersed catalysts continue to be reported for new reactions, there is a clear potential scientific benefit to develop computationally guided approaches for characterization of these materials, specifically for the quantitative identification of the metal site environment(s).

As a point of departure from reported investigations, we now describe a theory-led workflow for characterizing atomically dispersed supported metal catalysts. Our approach combines state-of-the-art characterization techniques (high-angle annular dark field (HAADF) STEM, EXAFS spectroscopy, and high-energy resolution fluorescence detection (HERFD) XANES spectroscopy) with DFT-level theory for critical identification of the local environments for a prototypical catalyst—atomically

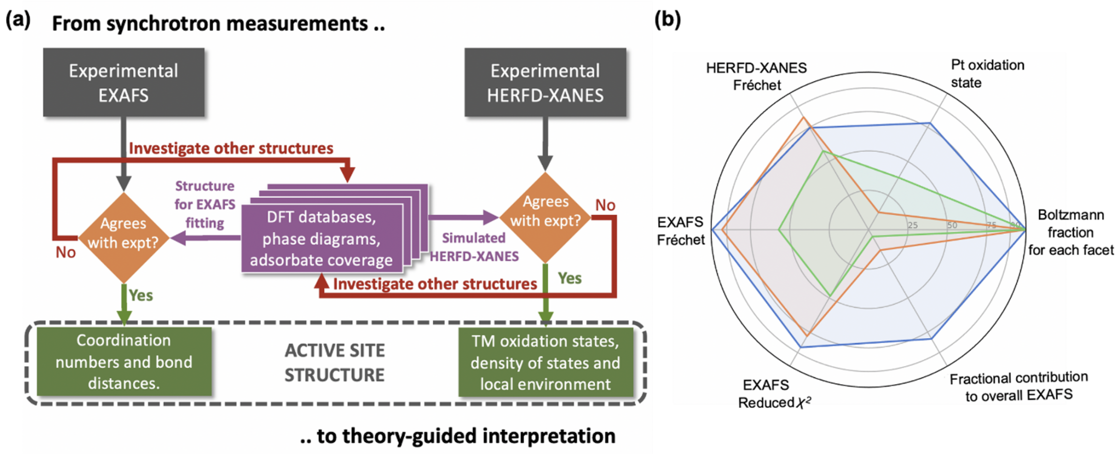

Figure 2.1. (a) Schematic representation of theory-guided workflow for identifying the Pt active sites stabilized within or on a MgO lattice. (b) Radar plot for the most stable [100], [100]Mg-vac, and [310] Pt configurations showing that the [100]Mg-vac/sub1 (blue) is more consistent with our experimental observations than [100]/sub0/$*O_2$ (orange) or [310]/pos1/$*O_2$ site (green). Structure models are presented in Figure 2.3.

dispersed Pt cations on MgO (Pt/MgO). We chose MgO as a prototypical support because it (a) is nonreducible, (b) consists of low-atomic-number elements for excellent contrast with Pt in STEM, and (c) is available as robust, high-area crystalline materials used in industrial catalysts.[5,10] These crystalline supports are expected to present limited numbers of sites for stable anchoring of isolated metal atoms, making Pt/MgO an excellent test case to exemplify our methodology. Figure 2.1a is a summary of our strategy that combines microscopy and conventional EXAFS analyses (Sections 2.3.1 and 2.3.2), large-scale DFT calculations (Section 2.3.3), automated DFT-based EXAFS analyses (Section 2.3.4), and FEFF-XANES spectroscopy (Section 2.3.5) to characterize Pt/MgO and identify the structure most consistent with data obtained through all the complementary techniques. As shown throughout this report, the outcome of this approach, represented as a radar plot (Figure 2.1b, details in Table 2.S1), identifies sub-surface Pt sites within MgO (denoted Pt^{+4}/[100]Mg-vac) to be the most populated sites for Pt atoms for this system. Although the approach is applied for atomically dispersed Pt/MgO (Section 2.3.6), we emphasize that the strategy is agnostic to the metal, the oxide support, and the reaction. To our best knowledge, this approach is unique in the field and represents a significant step forward towards the goal of comprehensive, validated integration of theoretical and experimental methods to describe the structure and catalytic function of isolated noble metal cations stabilized by a metal oxide support.

2.3 Results

2.3.1 Synthesis and structural characterization.

Atomically dispersed Pt on MgO, prepared from ethanol-water solutions of K_2PtCl_4 and slurried MgO powder, was calcined at 700 °C. Low Pt loadings (0.05 wt%) were targeted to minimize the number of different support surface sites that the Pt atoms occupy. TEM images and x-ray diffraction (XRD) patterns show that MgO was present as the cubic phase consisting of approximately 200-nm diameter crystallites; there was no XRD evidence of metallic Pt (Figure 2.S1). The calcined MgO was highly dehydroxylated, with only a weak OH band in the IR spectrum, at 3741 cm^{-1} (Figure 2.S2). HAADF-STEM images show atomically dispersed Pt in the absence of clusters or nanoparticles (Figure 2.2, Figure 2.S3). The bright spots in yellow circles (Figure 2.2a) show isolated Pt atoms along Mg columns in the (110) projection.[17] Intensity profiles along the X–Y line in Figure 2.2b (Figure 2.2c) confirm the isolation of the Pt atoms.

2.3.2 Conventional EXAFS analysis.

Pt L3-edge EXAFS spectra were modeled in Artemis[18] using traditional methods. The best-fit model comprises three scattering paths: Pt–O (2.05 ± 0.01 Å), with a

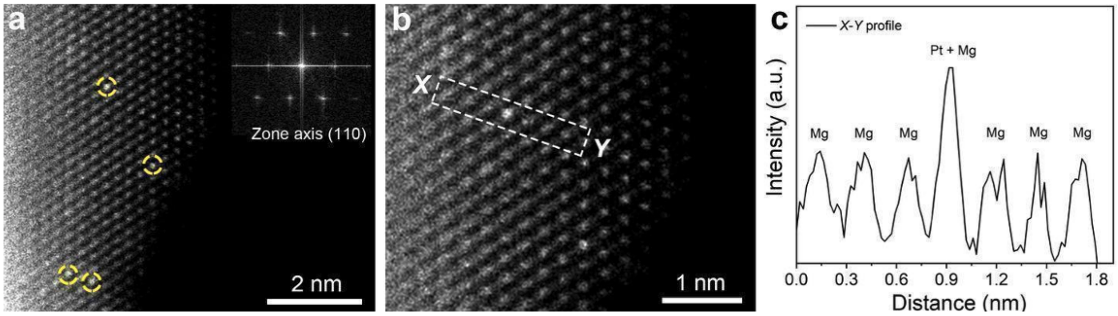

Figure 2.2. (a) HAADF-STEM image (along the (110) zone axis) showing that the MgO-supported Pt atoms (yellow circles) were atomically dispersed. (b) Higher magnification image showing a single isolated Pt atom, and (c) corresponding intensity profile from the X–Y line scan in panel b

coordination number (CN) of 6.7 ± 0.8, and two Pt–Mg (3.01 ± 0.04 and 3.15 ± 0.04 Å), with a total CN of 11 (Figures 2.S4-2.S6, Tables 2.S2-2.S4). Addition of a Pt–Pt scattering path (expected at ∼ 2.7 Å for Pt^0 clusters) resulted in non-meaningful results,[19] confirming the atomic dispersion of Pt demonstrated by HAADF-STEM. The continuous Cauchy wavelet transform (CCWT) heatmap of the sample (Figure 2.S7a) shows two main scattering features arising from short and long distances.[20] This analysis provides evidence that the longer features at 5 $Å^{-1}$ arise from a lower-Z scattering atom than Pt (i.e., Mg) as it does not match the features of the CCWT for Pt metal (Figure 2.S7b). The scattering feature with a short-distance, low-Z scattering component was best-modeled as a Pt–O path. The higher-R (distance) component was modeled as two Pt–Mg paths at longer distances. We emphasize that this conventional analysis of the modeled EXAFS data is insufficient to determine more than a single average, best-fit structure. Thus, it is difficult to define the actual bonding site. To address the possible presence of more than one significant supported Pt species and to exhaustively examine the possible Pt bonding environments, we developed an automated, high-throughput DFT-based workflow for EXAFS data fitting that reduces user intervention, and thereby improves the objectivity of the data interpretation.

2.3.3 A comprehensive library of DFT-optimized structures.

We used a theory-guided characterization approach to elucidate the local Pt bonding environment, that is, using DFT calculations (PBESol functional, implemented in VASP)[21] to create a comprehensive library of all plausible Pt/MgO structures. As summarized in Figure 2.3a-c, we considered three representative MgO facets (terrace sites: [100], Mg vacancy terrace sites: [100]Mg-vac, step sites: [310]), various adsorbates ($*$O, $*O_2$), vacancy types (O_{vac}, Mg_{vac}), and sub-surface Pt locations.[22] These structures spanning a wide range of local Pt environments were used to construct the temperature-dependent phase diagram (using pMuTT, harmonic approximation for vibrational entropy) for each site.[23] We chose to analyze each facet separately as the mechanism of Mg-vacancy formation (and therefore, Mg chemical potential (μ_{Mg})) during the high-temperature calcination is not known.

The phase diagrams in Figure 2.3d-f show the relative stabilities of various Pt sites (i.e., locations and adsorbate coverages) for the [100], [100]Mg-vac, and [310] facets. Our calculations for the stoichiometric [100] and [310] surfaces show that surface Pt ([100]/sub0/$*O_2$) and leading step edge ([310]/pos1/$*O_2$) sites are favored under our experimental conditions (T = 300 K, P_{O2} = 1 bar), respectively. Although the results demonstrate weaker O_2 binding for [100]/sub1 (O_2 desorption is predicted at T > 600 K), the unsaturated [310]/pos1 (orange gold triangles) and [310]/pos2 (orange gold squares, 0.1 eV less stable) sites are characterized by strong $*$O adsorption associated with the undercoordinated Pt atom. In contrast, no oxygen adsorption is predicted on the most stable [100]Mg-vac/sub1 structure at room temperature. Next, we compared the relative stabilities of Pt atoms at the surface and in sub-surface layers for

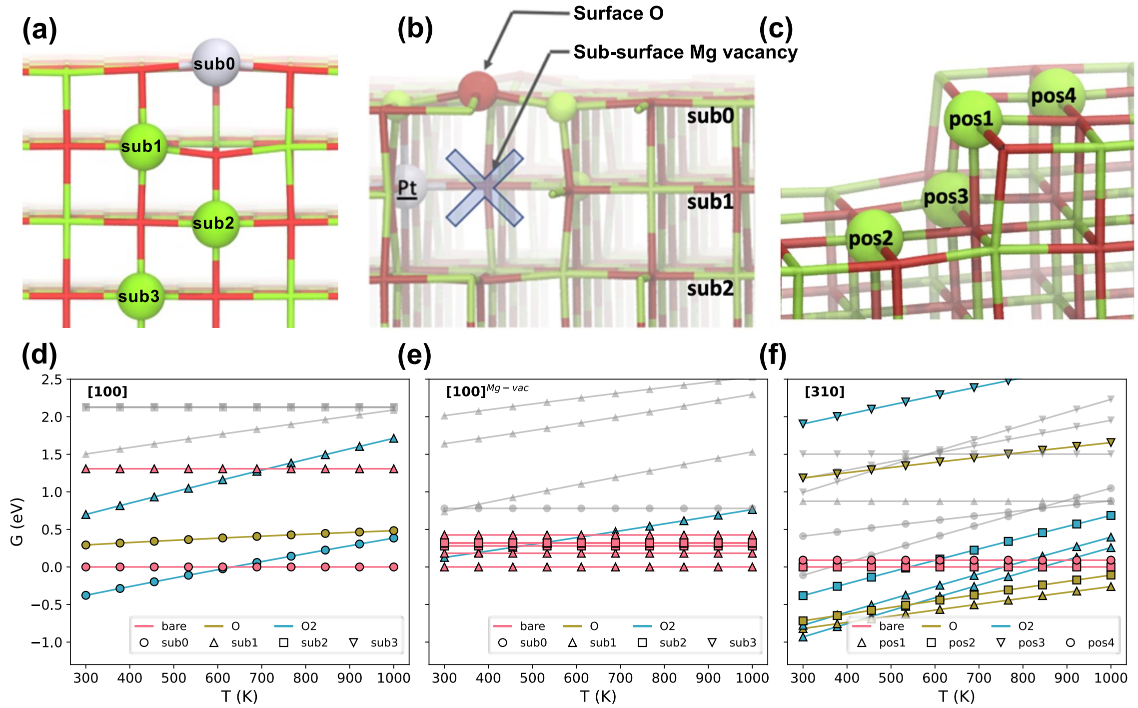

Figure 2.3. Atomistic models for the (a) [100], (b) [100]Mg-vac, and (c) [310] MgO facets considered in this study. Color scheme: Mg (green), O (red), Pt (grey). The corresponding temperature-dependent phase diagrams are summarized in (d), (e), and (f). Notation scheme for [100] and [100]Mg-vac MgO terraces: top surface (sub0), first (sub1), second (sub2), and third (sub3) sub-surface layers. For the [310] facet, we considered various step site positions including leading step edge (pos1), lower step edge (pos2), underneath step edge (pos3), and behind step edge (pos4). The phase diagrams were calculated relative to the most-stable "bare" Pt-configuration (i.e., without adsorbates). All DFT-optimized structures are available as an Atomic Simulation Environment (ASE) database file[24] in the Supporting Information.

the various MgO facets. Significantly, for the stoichiometric [100] facet, Pt sites in the first (second) sub-surface layer are 1.3 (2.1) eV less favorable energetically than those at the MgO surface (Figure 2.3d-f). Although surface Pt sites are preferred for the stoichiometric [100] surface (i.e., [100]/sub0, circles in Figure 2.3d), the calculations show that creation of a Mg-vacancy (denoted as [100]Mg-vac) changes the relative stabilities. Specifically, in contrast to that in the [100] facet, Pt substitution in the first sub-surface layer ([100]Mg-vac/sub1) is energetically more favorable than that in the surface layer (0.8 eV less stable, [100]Mg-vac/sub0) or the second sub-surface layer (0.3 eV less stable, [100]Mg-vac/sub2) (Figure 2.3d-f). These computational results are based on the PBESol functional; similar calculations with other functionals (RPBE/D3(BJ) and PBE/D3(BJ)) did not qualitatively change the trends (Figure 2.S8).

2.3.4 Automated DFT-based workflows for fitting EXAFS data with improved thoroughness and objectivity.

Although conventional EXAFS modeling indicates high Pt–O and Pt–Mg CNs and the absence of a Pt–Pt contribution, we emphasize that this “hands-on” approach is limited to analyzing a few plausible, average scattering paths and does not identify a specific bonding configuration. This approach is therefore not sufficient to characterize the possible anisotropy of the individual Pt–O and Pt–Mg contributions. To overcome this limitation, we used the open-source X-ray analysis package Larch to perform EXAFS analysis of all 47 DFT-optimized structures mentioned above.[25] The DFT-optimized structures were used “as-is” in the fitting, with fixed CNs and spatial orientations of Mg and O atoms in the fitting. In contrast to the typical approach whereby the average nearest-neighbors fits (described by the average bond lengths and CNs) are used to create structural models, we considered all relevant scattering paths (> 250 in some cases) for each DFT-optimized structure. Notwithstanding the increased sophistication of this approach, it provides a typical EXAFS fit for each candidate structure in a few minutes, without user intervention.

As the contribution of each scattering path to the total EXAFS depends on various parameters, it is important to limit the total number of variables in the

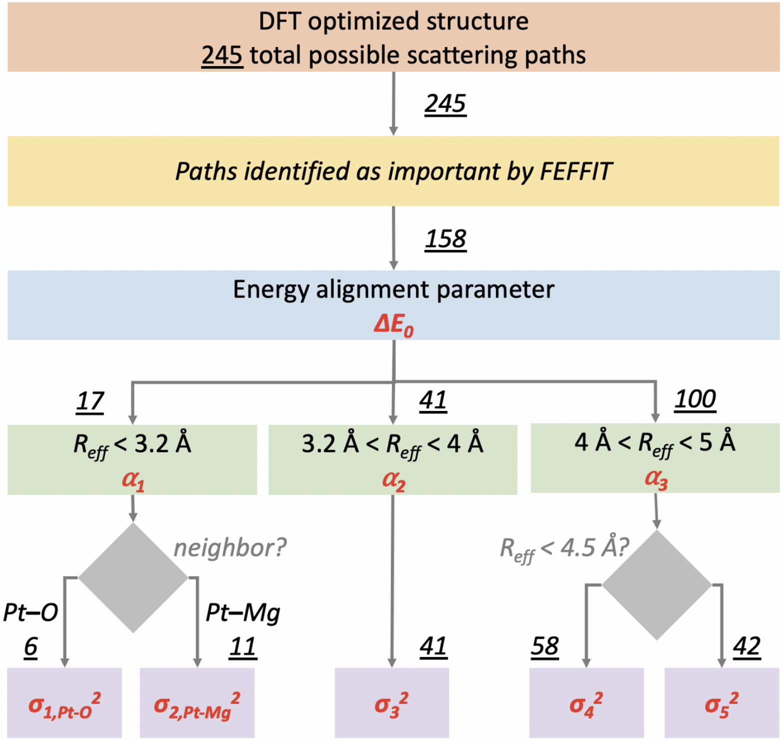

Figure 2.4. Flow-chart for hierarchically classifying all the possible paths into categories. The underlined numbers show the number of paths in the hierarchical classification approach, and the text in red identifies fitted parameters.

fitting. This efficiency is achieved by (1) hierarchically classifying the individual paths into distinct categories based on their effective scattering distances (R_{eff}) and the identity of the scattering atom (if $R_{eff} < 3.2$ Å) and (2) limiting the number of EXAFS variables optimized across each category. Specifically, for each DFT-optimized structure, our algorithm uses the following EXAFS fitting parameters: one energy alignment parameter (denoted as $\Delta E0$); a single value is used for all paths three distance scaling parameters, α_1, α_2, and α_3, one each for three different R_{eff} ranges, where $R_{eff,optimized} = \alpha_i \times R_{eff,DFT}$ and five mean square variations in path lengths that depend on the scatterer identity (e.g., $\sigma^2_{1,Pt-O}$ and $\sigma^2_{1,Pt-Mg}$ if $R_{eff} < 3.2$ Å) and the effective scattering distance (e.g., σ^2_3, σ^2_4, σ^2_5). The hierarchical classification is summarized in Figure 2.5 and Table 2.1. The details of this approach and strategy of this categorization are discussed in the Supporting Information.

Table 2.1. Summary of hierarchical approach used to classify all possible scattering paths into five different categories. Only 9 parameters (shown in red) are optimized in the automated EXAFS analyses.

Category	**Classification criterion**	**Number of paths**	**Variables**		
1	$R_{eff} < 3.2$ Å and Pt–O scatter	6	ΔE_0	α_1	$\sigma^2_{1,Pt-O}$
2	$R_{eff} < 3.2$ Å and Pt–Mg scatter	11			$\sigma^2_{1,Pt-Mg}$
3	3.2 Å $< R_{eff} <$ 4 Å	41		α_2	σ^2_3
4	4 Å $< R_{eff} <$ 4.5 Å	58		α_3	σ^2_4
5	4.5 Å $< R_{eff} <$ 5 Å	42			σ^2_5

The scattering path classification scheme described above ensures that (1) the constraints on the number of fitting parameters (calculated on the basis of the Nyquist criterion) are not violated and (2) physically relevant characteristics of scattering paths (e.g., different mean square variations in path length, that is, $\sigma^2_{1,Pt-O}$ and $\sigma^2_{1,Pt-Mg}$ for Pt–O and Pt–Mg scatterers) are faithfully captured. The use of DFT structures enables modeling of the longer effective scattering distances (~ 5 Å), including contributions from multiple scattering paths using distance-dependent fitting parameters (e.g., σ_i^2, and α_i) without overfitting the data. These points are well-illustrated by our analyses for the [100]Mg-vac/sub1 site (Figure 2.4), whereby only 9 parameters (Table 2.1 and 2.2) are used to model all 158 unique scattering paths.

Table 2.2. Optimized values of the 9 fitting parameters for the [100]Mg-vac/sub1 site.

Category	**ΔE_0 (eV)**	**α_i**	**10^3 x σ_i^2 (Å^2)**	**$R_{eff,optimized}$ (Å^2)**
1	4.8 ± 1.9	0.994 ± 0.005	3.2 ± 1.0	2.01, 2.01, 2.02, 2.03, 2.04, 2.05
2			6.7 ± 1.6	2.96, 2.97, 2.98, 2.98, 2.99, 2.99, 3.00, 3.00, 3.01, 3.01, 3.02
3		0.987 ± 0.011	6.3 ± 7.0[a]	3.40 – 3.79[b]
4		0.996 ± 0.001	6.2 ± 5.4[a]	4.02 – 4.40[c]
5			5.3 ± 4.3[a]	4.59 – 4.98[d]

The above fitting workflow was repeated for each unique DFT structure. In addition to the reduced-χ^2 metric (commonly used by the XAS community), we quantified the agreement between the experimental and simulated EXAFS spectra for each DFT structure by using the Fréchet distance in R-space for the magnitude portions of the data and the model (denoted as δF, which measures the similarity between two curves). The histogram in Figure 2.5a shows the reduced-χ^2 of the EXAFS fit corresponding to each DFT structure, along with the Fréchet distance (a lower value is better), corresponding to each structure. In general, we observed that the [100]Mg-vac structures (blue bars in Figure 2.5a) are in better agreement with experiment (reduced-$\chi^2 < 20$, $\delta F < 2$). Although some of the [100] and [310] Pt configurations (e.g., [100]/sub1 and [310]/pos3/$*O_2$) show satisfactory agreement with experimental EXAFS (reduced-$\chi^2 < 35$, $\delta F < 4.5$), our DFT calculations show these configurations to be highly unstable (1.5 eV and 0.99 eV, respectively).

This interplay between thermodynamic stability of a structure and its consistency with the EXAFS data is quantitatively illustrated by comparing the quality of the EXAFS fits with the DFT-calculated Boltzmann fractions (at 300 K) (Figure 2.5b). Unsurprisingly, only the most stable structures ([100]/sub0/$*O_2$ (orange circle), [100]Mg-vac/sub1 (blue triangle), and [310]/pos1/$*O_2$ (green triangle)) were observed in any significant number (based on Boltzmann distributions). The EXAFS fits corresponding to the three stable Pt configurations are presented in Figure 2.5c-e, showing that the [100]Mg-vac/sub1 ($CN_{Pt-O} = 6$, $CN_{Pt-Mg} = 11$) model agrees most closely with experiment. Specifically, although the [100]/sub0/$*O_2$ structure agrees satisfactorily with the Pt–O scattering path (CNPt-O = 7), the Pt–Mg path is underestimated, corresponding to the much lower Pt–Mg contribution (CN_{Pt-Mg} = 8). We emphasize that the [310]/pos3 site (as suggested by Sarma et al.)[26] has coordination numbers similar to those characterizing [100]Mg-vac/sub1, but it does not agree well with the EXAFS data (Figure 2.S10). These results demonstrate that both the effects of coordination number (i.e., [100]/sub0/$*O_2$ vs. [100]Mg-vac/sub1) and the local spatial orientation of the scattering atoms (i.e., [310]/pos3 vs. [100]Mg-vac/sub1) are captured in our EXAFS fitting approach. At this stage, it is useful to highlight an additional advantage of our EXAFS fitting procedure, with [100]Mg-vac/sub1 used as an illustrative example. Instead of using the average Pt–O (and/or Pt–Mg) distances and coordination numbers as the fitting parameters (as done conventionally), in our approach each individual Pt–O (total 6 for [100]Mg-vac/sub1 as an example) and Pt–Mg (total 11) scattering path is considered separately. This procedure allows us to capture the anisotropies of the local bonding environment, as indicated by the DFT-calculated bond lengths. Overall, we considered 158 total paths, which included single, double, and multiple scattering paths (involving up to 5 scattering atoms), using only use 9 fitting variables (Tables 2.1 and 2.2) to achieve unprecedented agreement with the experimental EXAFS across the entire R-range (Figure 2.5g). As the entire workflow relies on physically motivated models, it is possible to bolster the self-consistency between DFT structures and EXAFS fits. Beyond providing good models for the EXAFS fits, the DFT calculations also provide force constants that can be used to generate ab-initio vibrational mean-square relative displacements for the EXAFS (i.e., σ^2).[27–29] Specifically, the values for σ^2 for Pt–Mg (0.005 Å^2) and Pt–O (0.003 Å^2) obtained from DFT-calculated harmonic frequencies are consistent with the results of the EXAFS fitting (Pt–Mg: 0.0067 ± 0.001 Å^2, Pt–O: 0.0032 ± 0.001 Å^2). This point highlights the uniqueness of our approach: (1) the DFT-optimized structures are used to perform an objective, thorough EXAFS fitting, and (2) the EXAFS fitting parameters (themselves determined using the automated Python workflows) are consistent with independently calculated thermal disorders (from DFT vibrations). This level of detail has not been reported for any atomically dispersed catalysts, and we posit that it represents a significant step forward in automated analysis, self-consistent interpretation of EXAFS data.

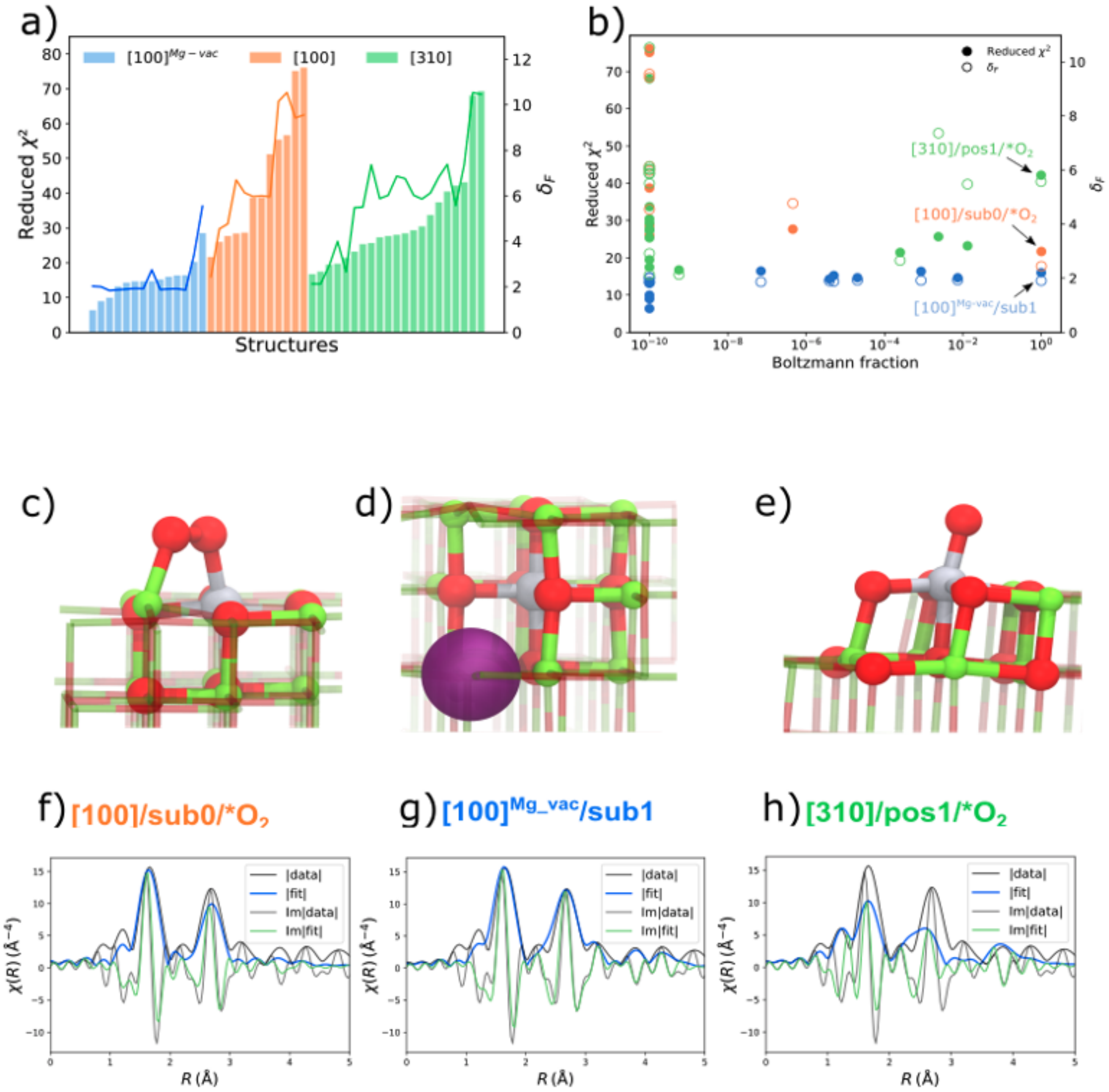

Figure 2.5. (a) Reduced-χ^2 and Fréchet distance (δ_F) of EXAFS analysis for all the DFT-optimized structures, (b) Boltzmann fraction calculations for all facets. The DFT optimized geometries of the most stable (c) [100]/sub0/$*O_2$ (d) [100]Mg-vac/sub1, and (e) [310]/pos1/$*O_2$ structures are shown with the corresponding EXAFS fits in (f), (g), and (h) showing the magnitude (fit: blue, experiment: black) and imaginary portions (fit: green, experiment: black) of Fourier transforms. The k-range of 2.2–12.5 Å^{-1} and the R-range of 1.0–5.0 Å were used for the fits. Colors: Mg (green), O (red), Pt (grey). The purple sphere in (d) represents the sub-surface Mg-vacancy.

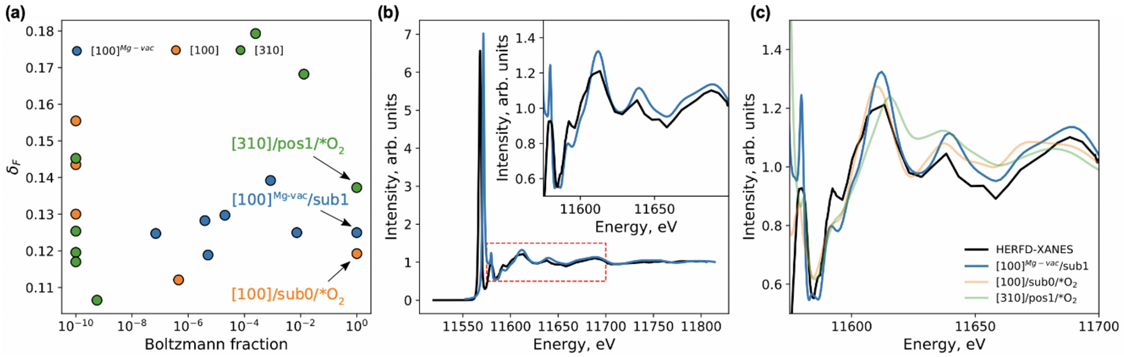

Figure 2.6. (a) Fréchet distances from comparison of HERFD-XANES data with FEFF-simulated XANES and DFT-calculated Boltzmann fractions. (b) Simulated and experimental XANES spectra for [100]Mg-vac/sub1. Inset (dashed red box) shows the region of the spectra from 11575–11700 eV. (c) Comparison of FEFF-simulated XANES spectra of the most stable structures from each facet ([100]Mg-vac/sub1, [100]/sub0/$*O_2$, and [310]/pos1/$*O_2$) with HERFD-XANES data from 11575–11700 eV.

2.3.5 XANES evidence of structure.

In addition to the EXAFS, we also consider the XANES data (Figure 2.S11; data characterizing reference compounds are shown for comparison). XANES spectra provide evidence of the Pt electronic structure, as the intensity of the white line at the Pt L3 edge is a measure of the unoccupied d-states and occupied p-states (2p3/2 → 5d3/2 or 5d5/2).[30] The oxidation state of the supported Pt is close to that of Pt^{4+} in $H_2Pt(OH)_6$ and markedly different from that of the Pt^{2+} in $Pt(acac)_2$ (acac = acetylacetonato, $[C_5H_7O_2]^-$) and Pt^0 in Pt foil (Figure 2.S11). These data imply that isolated Pt^{4+} was present in six-coordinate octahedral geometry in cation vacancy sites, consistent with the STEM and EXAFS data. To account for charge balance, one Pt^{4+} in an MgO sub-surface site requires one Mg^{2+} vacancy, which implies a Pt-Mg coordination number of 11 and not 12, consistent with the EXAFS analyses. These results further agree with DFT-calculated Bader charges that show consistent oxidation states for the sub-surface Pt^{4+} with one Mg vacancy and the Pt^{4+} in $H_2Pt(OH)_6$ (q_{Bader} = +1.35e and +1.41e, respectively). These values are much higher than q_{Bader} = +0.86e for the Pt^{2+} in $Pt(acac)_2$.

We also collected HERFD-XANES spectra; HERFD-XANES minimizes the limitations of energy resolution affected by core-hole lifetime broadening and beamline optics in conventional XANES.[31] A comparison of the HERFD and conventional XANES data (Figure 2.S11) shows the advantages of HERFD in resolving near-edge features including (a) the stable near-zero signal in the pre-edge; (b) strong intensities and sharpness without a long tail characterizing the white line; and (c) the clear resonance feature with little broadening beyond the white line. The HERFD-XANES data provide insight into the catalyst structure beyond what is determined by the EXAFS data and DFT-guided analysis.[32] The HERFD-XANES data were compared with FEFF-simulated XANES spectra based on the aforementioned DFT-determined structures (Figure 2.6).[33,34] The agreement between experimental and simulated XANES spectra (quantified using the Fréchet distance (δ F)) is compared with the thermodynamic stability (Figure 2.6a) of various Pt sites. Figure 2.6b, c show a comparison of the experimental HERFD and the FEFF simulations for each of the most stable structures predicted from DFT-calculated Boltzmann fractions: [100]/sub0/$*O_2$ (99.2%), [100]Mg-vac/sub1 (99.9 %), and [310]/pos1/$*O_2$ (98.4%). The FEFF results were shifted 4.5 eV and scaled to match the normalized experimental results for values $>$ 11650 eV. Of all the stable structures, both [100]/sub0/$*O_2$ and [100]Mg-vac/sub1 show good agreement with the experimental XANES; however, by comparing the corresponding EXAFS spectra in Figure 2.6f and g, we see that the Mg-vacancy provides a notable improvement over [100]/sub0/$*O_2$. Although some [310] structures are more consistent with experiment than these ($\delta F < 0.125$), they are significantly less stable (Boltzmann fraction $< 10^{-9}$), and, we infer, unlikely to exist. The most stable [310] structures show poor agreement with experiment (Figure 2.6c (green)). Taking together the unique combination of EXAFS and HERFD-XANES fits of [100]Mg-vac/sub1 and the DFT-predicted stability, our results show that the Pt/MgO catalyst is well-characterized as an atomically dispersed Pt^{4+} ion embedded in the first subsurface layer (sub1) located adjacent to a Mg-vacancy site. As shown in Figure 2.S12, our HERFD-XANES analyses and DFT calculations do not identify the exact location of the Mg-vacancy site; we used the most stable structure, Mg-vacancy in the surface layer (sub0) for further analysis. To analyze the origin of the various features in the HERFD, Figure 2.S13 shows the locally projected, l-dependent density of states (l-DOS) of the [100]Mg-vac/sub1 site. Overall, the Pt L3 HERFD spectra resemble the Pt d-DOS, as indicated by the vertical dashed lines. The white line is composed largely of Pt d-DOS with a small contribution from the O p-DOS, with its position being largely insensitive to the local disorder. The second peak (∼ 9 eV above the Fermi level) shows contributions from both the O and Mg atoms as well as the local Pt s-DOS, indicating that this feature corresponds to non-local states and arises at least in part from bonding of Pt to the near-neighboring atoms (Figure 2.S13).

2.3.6 CO oxidation catalyzed by Pt/MgO.

We characterized the Pt/MgO as a catalyst for CO oxidation as a probe reaction. The light-off curves (Figure 2.7a) show that the reaction became readily measurable at approximately 180 °C, with the CO conversion reaching nearly 100% at 280 °C under our conditions. Separate experiments were carried out to determine reaction rates (turnover frequencies, TOF, rates per Pt atom) from data obtained at low conversions (<5%), which were shown to be differential by the linear dependence of conversion on inverse space velocity at temperatures of 180–200 °C (Figure 2.7b,c). An Arrhenius plot (Figure 2.7d) indicates an apparent activation energy of 79 ± 2 kJ mol^{-1}. Data showing conversion as a function of time onstream in the flow reactor under steady-state conditions (Figure 2.S14) indicate that the catalyst was stable, retaining its activity for as long as it was onstream (48 h) at 210 °C. The catalyst remained white in color after use. The HAADF-STEM images of used Pt/MgO samples (after three light-off experiments) show that Pt was still atomically dispersed (Figure 2.S15), even at a high temperature (300 °C). As further checks of the catalyst stability, we recorded in-operando HERFD-XANES data during CO oxidation at 210 °C (Figure 2.S16), demonstrating unchanged spectra.

This catalytic probe reaction provided yet another opportunity to verify the identity of the support sites for Pt. Figure 2.7e shows trends in CO adsorption for the stable [100]Mg-vac/sub1 Pt terrace site at various temperatures. Unsurprisingly, stronger CO adsorption was found for the undercoordinated Pt site (i.e., [100]/sub0);

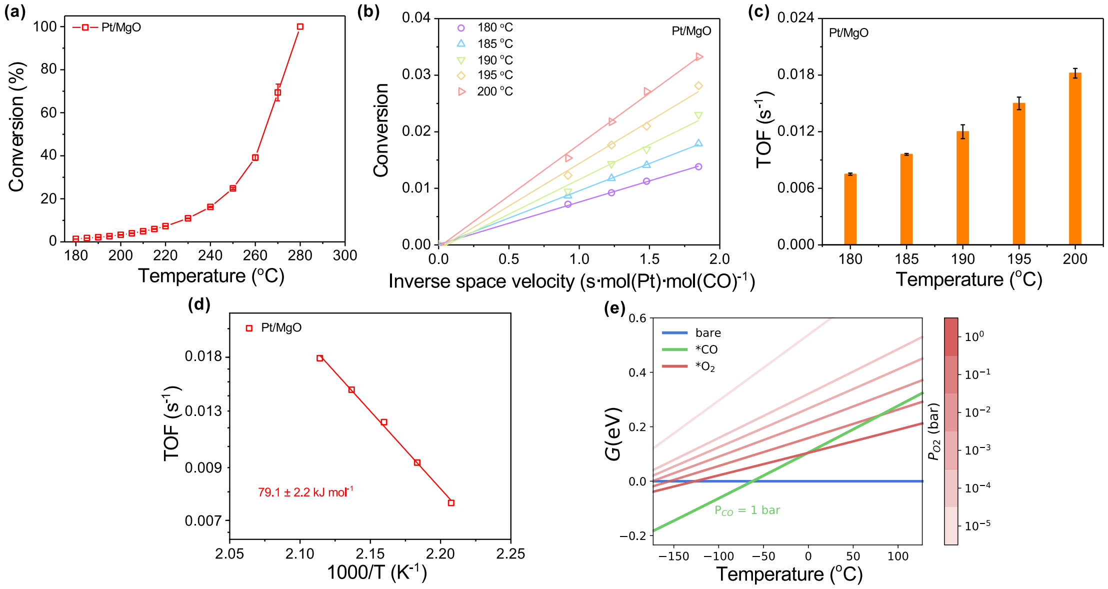

Figure 2.7. (a) Light-off curve characterizing CO oxidation catalyzed by Pt/MgO. Error bars represent standard deviation determined from three independent measurements. The once-through plug-flow reactor was heated from room temperature at a rate of 2 °C/min to 300 °C. The feed was 5.0% CO in helium flowing at 4.0 mL (NTP)/min + 5.0% O_2 in helium flowing at 16.0 mL (NTP)/min; the catalyst mass was 100 mg. (b) Demonstration of differential conversion at various temperatures. Low-conversion (<5%) data were obtained under the conditions stated in a, except that the feed gas was 5.0% CO in helium flowing at 5.0, 6.0, or 8.0 mL (NTP)/min + 5.0% O_2 in helium flowing at 20.0, 24.0, or 32.0 mL (NTP)/min; the catalyst mass was 100 mg. (c) TOF values determined from slopes of lines in b, with errors. (d) Arrhenius plot. (e) DFT-calculated CO and O_2 adsorption at various temperatures and O_2 partial pressures.

we predicted CO adsorption at temperatures as high as about 83 °C (Figure 2.S17). In contrast, the sub-surface Pt site ([100]Mg-vac/sub1) is characterized by weaker CO binding (0.25 eV at 83 °C); no CO adsorption was predicted at room temperature. The trends for the [100]Mg-vac/sub1 site are consistent with (1) our IR experiments that do not show significant CO uptakes at room temperature (Figure 2.S18) and (2) Sarma's report[26] of low-temperature (-163 °C) IR spectra of CO on a sample similar to ours; a 2166 cm^{-1} ν_{CO} band was observed, agreeing within error with our calculated frequency (2141 cm^{-1}).

It is significant, and a challenge to our interpretation, that our Pt/MgO catalyst, which consists of sub-surface, highly coordinated Pt sites, does not bind CO at room temperature but nonetheless is catalytically active for CO oxidation. Thus, we turned to DFT calculations (RPBE/D3-BJ functional, nudged elastic band and dimer method for barriers) to investigate various possible mechanisms of CO oxidation on the [100]Mg-vac/sub1 site, and the two most favorable mechanisms are shown in Figure 2.8. Indeed, our calculations show that the insertion of CO into the surface-bound O_2 is the rate limiting step—the calculated enthalpic barrier (105.3107.4 kJ/mol) is in satisfactory agreement with experimentally determined apparent activation energies (Figure 2.8a); similar carbonate species were proposed by Sarma et al.[26] for Pt at the step site on MgO. The addition of the subsurface Pt and Mg vacancy activates the bound O_2 and allow for CO insertion to form the intermediate carbonate. Charge density difference plots showing the change in the electronic structure of the $*O_2$ compared to pristine MgO are shown in Figure 2.S19. Although the role of the Pt atom in this mechanism differs greatly to what has been reported by Sarma, the calculated free energy barrier at 300 °C in this work is slightly lower (169 kJ/mol compared to 173 kJ/mol[26]). Additionally, a similar Eley–Rideal mechanism has been seen in a MgO/Ag system.[35] A second mechanism consisting of the abstraction of a surface oxygen by CO to form an oxygen vacancy as the rate limiting step is shown in Figure 2.8b. The similarity of the free energy barrier of these two mechanisms (170.2 kJ/mol versus 168.8 kJ/mol) make it challenging to discern which mechanism is more favorable and both appear reasonable according to our calculations.

A pertinent question is whether the catalyst underwent structural changes under the conditions of CO oxidation catalysis. The EXAFS data recorded after catalysis were not substantially different from those observed before, with [100]Mg-vac/sub1

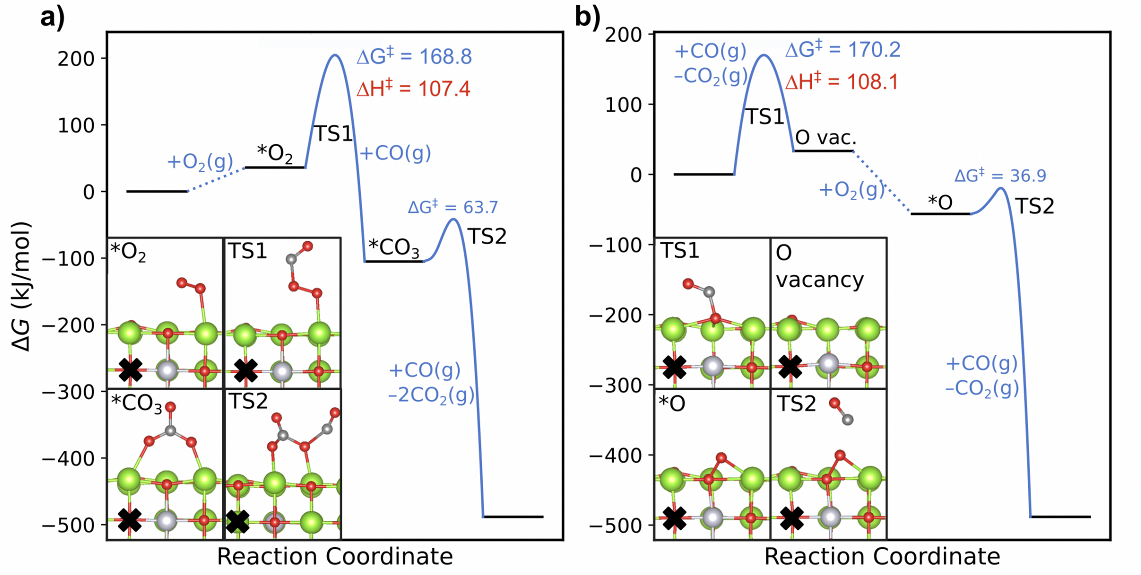

Figure 2.8. Reaction free energy diagrams for CO oxidation on [100]Mg-vac/sub1 surface at 300 °C. Mechanism a) consists of an Eley–Rideal type mechanism with the formation of a carbonate intermediate, while mechanism b) proceeds through the formation of an oxygen vacancy above the subsurface Pt. Calculated free energy (blue) and enthalpic (red) barriers are annotated for each transition state. Insets show the optimized structures of the key intermediate species with the location of the Mg vacancy marked with a black cross (colors: Mg, green; O, red; Pt, light grey; C, dark grey).

again emerging as the best-fit model of the EXAFS spectra (Figure 2.S20). This comparison in in line with the catalyst performance data, indicating that the MgO-supported platinum sites are stable under CO oxidation conditions.

2.4 Discussion

The intense recent attention paid to atomically dispersed supported metal catalysts reflects the promise of catalysts with valuable new properties and the prospect that some will be so simple in structure as to propel significant advances in the understanding of surface catalysis broadly at the atomic level.[9,36] Some literature reflects the notion that these catalysts are straightforward to understand because the metals are atomically dispersed[36], but this view overlooks the intrinsic complexity of the supports and the need to incorporate the metal–support combinations in realistic models of the catalysts. Thus, there is a motivation to work with metal–support-site combinations that are nearly unique and can be understood in depth. Consequently, researchers have been motivated to use crystalline metal oxides as supports and to use low metal loadings to create catalysts that can be approximated as isolated metals in unique, stable surroundings. The characterization data presented here validate that approach. They have a high degree of internal consistency and show that the structure of the catalyst consisting of Pt in a loading of only 0.05 wt% on crystalline MgO powder is well represented with a single, stably encapsulated—yet still catalytically active—structure that meets the criterion of near structural uniqueness. A full set of complementary experimental characterizations combined with theoretical verification was needed to test the hypothesis that such a catalyst could be characterized structurally with some confidence. The DFT-guided EXAFS fitting approach described here represents, we posit, a substantial advance in the characterization of such catalysts. Although previous approaches represent attempts to develop DFT models that are motivated by results of conventional EXAFS analyses, we instead used a library of DFT-optimized Pt structures to identify the single best representation of the all the experimental results (e.g., EXAFS, HERFD-XANES, IR spectra of adsorbed CO, and catalytic kinetics) collected in this investigation. Going forward, we anticipate that further development of this combination of characterization techniques will help guide the choice of metal–support combinations to advance the field of atomically dispersed supported metal catalysts; help advance the understanding of the broad class of supported catalysts; and help guide the development of new and improved methods for understanding of even more complex surface structures.

2.5 Experimental and Computational Methods

2.5.1 Synthesis of Pt/MgO samples.

MgO powder (1000 mg, US Research Nanomaterials) with a manufacturer-specified specific surface area of 25 m2/g was dispersed in 250 mL of ethanol in a 500-mL beaker with magnetic stirring. Aqueous K_2PtCl_4, 20 mL of 0.25 mM solution, and 40 mL of ethanol were transferred into the stirred beaker through a syringe pump at a rate of 5 mL/h. The resultant solid was collected by centrifugation, washed with distilled water, and then dried overnight in air in an oven at 80 °C. The resultant powder was calcined in flowing O_2 (10 mL(NTP)/min) and N_2 (40 mL(NTP)/min) as the temperature was ramped from room temperature to 120 °C and held for 2 h to remove any residual water and organics. The sample was then further calcined in a mixture of flowing O_2 (10 mL(NTP)/min) and N2 (40 mL(NTP)/min) as the temperature was ramped at a rate of 5 °C/min until a final temperature of 700 °C was reached, which was held for 4 h.

2.5.2 X-ray absorption spectroscopy.

XAS was carried out at beamlines 4-1 and 6-2 at the Stanford Synchrotron Radiation Lightsource (SSRL). At beamline 4-1, which is a side station on a 20-pole wiggler beamline, the ring SPEAR3 was operated in top-off mode with a storage ring energy of 3 GeV and 500 mA stored current. A Si double-crystal (220) monochromator was detuned by 20–25% of maximum intensity to minimize harmonics at the Pt L3 edge. XAS data were collected in fluorescence yield mode with a 30-element germanium solid-state detector array with samples pressed into a pellet at 25 °C. For energy calibration, a Pt foil reference was placed between the ion chambers upbeam and downbeam of the sample so that its spectrum was measured simultaneously with that of the sample.

At beamline 6-2, which is fed by a 56-pole, 0.9 Tesla wiggler, high-energy resolution fluorescence detection HERFD XANES experiments were conducted with a liquid-nitrogen-cooled double-crystal Si (311) monochromator to select the energy of the incident beam. A Rowland circle spectrometer (radius 1 m) equipped with three spherically bent Si (800) analyzers and a silicon drift detector were used to select the Pt-Lα emission line. A Pt foil was scanned in the transmission mode for initial energy calibration. For ex-situ HERFD-XANES experiments, the sample was pressed into a pellet at 25 °C. In each in-operando HERFD-XANES experiment, approximately 50 mg of catalyst sample was loaded into a flow-through cell, a Kapton tube (i.d. = 2.8 mm), connected to a treatment gas line.[37] The compositions of effluent gases flowing from the cell were measured with an online mass spectrometer (Hiden HPR20). The Pt/MgO was first heated in helium flowing at 20 mL(NTP)/min as the temperature was ramped from room temperature to 210 °C at a rate of 5 °C/min. Then the feed gas was switched to a mixture of CO flowing at 0.2 mL(NTP)/min + O_2 flowing at 0.8 mL(NTP)/min + helium flowing at 19 mL(NTP)/min with the sample in the cell held at 210 °C for 1 h as CO oxidation catalysis took place. Thereafter, the reactor was cooled to room temperature and the gas feed switched to helium flowing at 20 mL(NTP)/min. HERFD-XANES spectra were collected periodically during all these steps.

2.5.3 IR spectroscopy.

Transmission IR spectra of powder samples in the ν_{O-H} region were determined with a Bruker IFS 66v/S spectrometer with a resolution of 4 cm^{-1}. Approximately 10 mg of sample was loaded between two KBr windows, and spectra were recorded at room temperature with the sample under vacuum, with an average of 256 scans per spectrum. IR spectra of samples with adsorbed CO were determined with approximately 40 mg of sample pressed into a wafer loaded into a cell (In-situ Research Instruments, South Bend, IN) that served as a flow reactor fed with various gases, and transmission spectra of catalysts in the presence of these gases were recorded with a liquid-nitrogen-cooled MCT detector.

2.5.4 CO oxidation catalysis in a conventional laboratory plug-flow reactor.

The catalyst samples were evaluated for CO oxidation in a once-through plug-flow reactor, with products analyzed with an online mass spectrometer (Hiden Analytical HPR20) equipped with a secondary electron multiplier detector used in multiple ion detection mode. Samples of catalyst powder (100 mg) that had passed through a 40 to 60 mesh sieve were loaded into a quartz tube reactor (i.d. = 4 mm), with the upstream and downstream sections packed with quartz wool. In experiments to determine light-off curves for CO oxidation, the feed was a mixture of 5.0% CO in helium flowing at 4.0 mL(NTP)/min + 5.0% O_2 in helium flowing at 16.0 mL(NTP)/min; the pressure was atmospheric. The reactor was heated from room temperature at a rate of 2 °C/min with the gases flowing and then held at 300 °C for 20 min before the reactor was cooled down. In a separate flow reactor system, near-steady-state conversion data were obtained under the conditions stated in the preceding paragraph, except that the feed gas was a mixture of 5.0% CO in helium flowing at 5.0, 6.0, or 8.0 mL(NTP)/min + 5.0% O_2 in helium flowing at 20.0, 24.0, or 32.0 mL(NTP)/min. Catalytic reaction rates were calculated from low (differential) conversions (<5%) determined at temperatures in the range of 180–200 °C. In experiments determining the dependence of conversion on time on stream, the samples were kept on stream for up to 48 h to demonstrate stability at 210 °C; the feed was 5.0% CO in helium flowing at 4.0 mL(NTP)/min and 5.0% O_2 in helium flowing at 16.0 mL(NTP)/min.

2.5.5 Scanning transmission electron microscopy.

STEM imaging experiments were performed on a JEOL 200CF (NEOARM) transmission electron microscope with an acceleration voltage of 200 kV. The specimens were prepared by a direct dispersion of powder samples on lacey carbon grids. The HAADF images were acquired with a convergence angle of 28.5 mrad and an inner collection angle of 55 mrad.

2.5.6 Transmission electron microscopy.

TEM images of as-prepared sample powders loaded onto copper grids were recorded with a Hitachi H-7700 microscope at an acceleration voltage of 100 kV.

2.5.7 X-ray diffraction crystallography

XRD patterns of the samples were collected on a Philips X'Pert Pro Super diffractometer with a monochromatized Cu Kα radiation source and a wavelength of 0.1542 nm.

2.5.8 Inductively coupled plasma mass spectrometry.

The Pt loadings in the catalysts were determined by inductively coupled plasma mass spectrometry with a Thermo Scientific XSERIES 2 instrument.

2.5.9 DFT calculations.

Periodic DFT calculations were performed using the projector augmented wave method as implemented in the Vienna ab initio simulation package (VASP).[21] Energies were calculated using a 500 eV plane-wave cutoff with a $2 \times 1 \times 1$ Monkhorst-Pack k-point grid. A range of generalized gradient approximation functionals (PBE, RPBE, and PBESol) were used. Electronic energies were converged to 10^{-6} eV, and all structures were relaxed until the forces were less than 0.05 eV/Å. The finite displacement method (0.02 Å) was used to calculate the entropic and zero-point energy corrections. For CO oxidation mechanism calculations, a 400 eV plane-wave cutoff was used with the RPBE functional, and dispersion corrections were considered with the DFT-D3 method with Becke-Johnson damping. Barriers were calculated using the climbing image nudged elastic band and dimer methods.

2.5.10 Conventional XAS data analysis.

The EXAFS and XANES data were analyzed with the Demeter package18. Preprocessing of data included alignment, edge calibration, deglitching, normalization, background subtraction, and conversion of data into a chi file for data fitting, performed with Athena. The energy at the Pt L3 edge, determined by the first inflection point of the absorption edge data characterizing the reference Pt foil, was calibrated to the reported energy, 11564.0 eV. EXAFS data were modeled with the Artemis package in Demeter. The continuous Cauchy wavelet transform (CCWT)[20] was performed on the extracted EXAFS to visualize the data and assess how many scattering paths would be needed to fit the data. Larch[25] was used to perform the CCWT on EXAFS spectra at the Pt L3 edge characterizing Pt/MgO samples and Pt foil.

2.5.11 Automated DFT-based fitting of EXAFS data.

The EXAFS data were analyzed with the open-source X-ray Larch package.[25] Data processing, such as alignment, edge calibration, deglitching, normalization, and background subtraction, was performed using the Python interface to Larch. The DFT-optimized structures were used to generate a feff.inp file using an in-house code. These feff.inp files were run in Larch, with FEFF used for generating scattering paths. The code uses Matplotlib for plotting the fitting results.

2.5.12 FEFF and DOS modeling.

All HERFD simulations used DFT-optimized (PBE-D3) structures and were performed with FEFF 9 using SCF and FMS cutoff radii of 6 and 9 Å, respectively, which ensured convergence of the spectra.[33,34] The representative atomic potentials were chosen to reproduce chemical distinguishability for each atom type. On the basis of our experience with Pt-containing samples, we chose not to use a core-hole in the calculations.[38,39] To properly simulate HERFD rather than the default XANES in FEFF, we also removed 1.8 eV from the default core-hole lifetime broadening of 5.2 eV. The self-energy was modeled using the density-dependent MPSE (many-pole self-energy) dielectric function approach based on a weighted average of the atomic loss functions.[40] Moreover, to provide converged results up to about 200 eV above the edge, the maximum angular momenta for the site basis set were raised to 5, 4, and 4 for Pt, O, and Mg, respectively. Further, vibrational disorder was added using single-scattering Debye-Waller factors based on a correlated Debye model. The Debye temperature for this model was estimated for each system using average force constants for the first-shell Pt–O bonds obtained from the DFT structural simulations.[27,28]

2.6 References

[1] Joaquin Resasco, Leo DeRita, Sheng Dai, Joseph P Chada, Mingjie Xu, Xingxu Yan, Jordan Finzel, Sergei Hanukovich, Adam S Hoffman, George W Graham, Simon R Bare, Xiaoqing Pan, and Phillip Christopher. Uniformity Is Key in Defining Structure–Function Relationships for Atomically Dispersed Metal Catalysts: The Case of Pt/CeO2. *Journal of the American Chemical Society*, 142 (1):169–184, jan 2020. doi: 10.1021/jacs.9b09156.

[2] Leo DeRita, Joaquin Resasco, Sheng Dai, Alexey Boubnov, Ho Viet Thang, Adam S Hoffman, Insoo Ro, George W Graham, Simon R Bare, Gianfranco Pacchioni, Xiaoqing Pan, and Phillip Christopher. Structural evolution of atomically dispersed Pt catalysts dictates reactivity. *Nature Materials*, 18(7):746–751, 2019. doi: 10.1038/s41563-019-0349-9.

[3] Yifeng Zhu, Simuck F Yuk, Jian Zheng, Manh-Thuong Nguyen, Mal-Soon Lee, Janos Szanyi, Libor Kovarik, Zihua Zhu, Mahalingam Balasubramanian, Vassiliki-Alexandra Glezakou, John L Fulton, Johannes A Lercher, Roger Rousseau, and Oliver Y Gutiérrez. Environment of Metal–O–Fe Bonds Enabling High Activity in CO2 Reduction on Single Metal Atoms and on Supported Nanoparticles. *Journal of the American Chemical Society*, 143(14):5540–5549, apr 2021. doi: 10.1021/jacs.1c02276.

[4] Zailei Zhang, Yihan Zhu, Hiroyuki Asakura, Bin Zhang, Jiaguang Zhang, Maoxiang Zhou, Yu Han, Tsunehiro Tanaka, Aiqin Wang, Tao Zhang, and Ning Yan. Thermally stable single atom Pt/m-Al2O3 for selective hydro-

genation and CO oxidation. *Nature Communications*, 8(1):16100, 2017. doi: 10.1038/ncomms16100.

[5] Adam S Hoffman, Louise M Debefve, Shengjie Zhang, Jorge E Perez-Aguilar, Edward T Conley, Kimberly R Justl, Ilke Arslan, David A Dixon, and Bruce C Gates. Beating Heterogeneity of Single-Site Catalysts: MgO-Supported Iridium Complexes. *ACS Catalysis*, 8(4):3489–3498, apr 2018. doi: 10.1021/acscatal.8b00143.

[6] Yongwoo Kwon, Tae Yong Kim, Gihun Kwon, Jongheop Yi, and Hyunjoo Lee. Selective Activation of Methane on Single-Atom Catalyst of Rhodium Dispersed on Zirconia for Direct Conversion. *Journal of the American Chemical Society*, 139(48):17694–17699, dec 2017. doi: 10.1021/jacs.7b11010.

[7] Lulu Li, Xin Chang, Xiaoyun Lin, Zhi-Jian Zhao, and Jinlong Gong. Theoretical insights into single-atom catalysts. *Chem. Soc. Rev.*, 49(22):8156–8178, 2020. doi: 10.1039/D0CS00795A.

[8] Sharon Mitchell and Javier Pérez-Ramírez. Single atom catalysis: a decade of stunning progress and the promise for a bright future. *Nature Communications*, 11(1):4302, 2020. doi: 10.1038/s41467-020-18182-5.

[9] Yizhen Chen, Hanlei Sun, and Bruce C Gates. Prototype Atomically Dispersed Supported Metal Catalysts: Iridium and Platinum. *Small*, 17(16):2004665, apr 2021. doi: https://doi.org/10.1002/smll.202004665.

[10] Maria Flytzani-Stephanopoulos and Bruce C Gates. Atomically Dispersed Supported Metal Catalysts. *Annual Review of Chemical and Biomolecular Engineering*, 3(1):545–574, jun 2012. doi: 10.1146/annurev-chembioeng-062011-080939.

[11] Manoja K Samantaray, Valerio D'Elia, Eva Pump, Laura Falivene, Moussab Harb, Samy Ould Chikh, Luigi Cavallo, and Jean-Marie Basset. The Comparison between Single Atom Catalysis and Surface Organometallic Catalysis. *Chemical Reviews*, 120(2):734–813, jan 2020. doi: 10.1021/acs.chemrev.9b00238.

[12] Ruixuan Qin, Kunlong Liu, Qingyuan Wu, and Nanfeng Zheng. Surface Coordination Chemistry of Atomically Dispersed Metal Catalysts. *Chemical Reviews*, 120(21):11810–11899, nov 2020. doi: 10.1021/acs.chemrev.0c00094.

[13] Bruce C Gates. Atomically Dispersed Supported Metal Catalysts: Seeing Is Believing. *Trends in Chemistry*, 1(1):99–110, 2019. doi: https://doi.org/10.1016/j.trechm.2019.01.004.

[14] Selina K Kaiser, Zupeng Chen, Dario Faust Akl, Sharon Mitchell, and Javier Pérez-Ramírez. Single-Atom Catalysts across the Periodic Table. *Chemical Reviews*, 120(21):11703–11809, nov 2020. doi: 10.1021/acs.chemrev.0c00576.

[15] Yubing Lu, Jiamin Wang, Liang Yu, Libor Kovarik, Xiwen Zhang, Adam S Hoffman, Alessandro Gallo, Simon R Bare, Dimosthenis Sokaras, Thomas Kroll, Vanessa Dagle, Hongliang Xin, and Ayman M Karim. Identification of the active complex for CO oxidation over single-atom Ir-on-MgAl2O4 catalysts. *Nature Catalysis*, 2(2):149–156, 2019. doi: 10.1038/s41929-018-0192-4.

[16] Janis Timoshenko and Anatoly I Frenkel. "Inverting" X-ray Absorption Spectra of Catalysts by Machine Learning in Search for Activity Descriptors. *ACS Catalysis*, 9(11):10192–10211, nov 2019. doi: 10.1021/acscatal.9b03599.

[17] S J Pennycook and D E Jesson. High-resolution Z-contrast imaging of

crystals. *Ultramicroscopy*, 37(1):14–38, 1991. doi: https://doi.org/10.1016/0304-3991(91)90004-P.

[18] B Ravel and M Newville. ATHENA, ARTEMIS, HEPHAESTUS: data analysis for X-ray absorption spectroscopy using IFEFFIT. *Journal of Synchrotron Radiation*, 12(4):537–541, jul 2005. doi: 10.1107/S0909049505012719.

[19] Lichen Liu, Miguel Lopez-Haro, Christian W Lopes, Chengeng Li, Patricia Concepcion, Laura Simonelli, Jose J Calvino, and Avelino Corma. Regioselective generation and reactivity control of subnanometric platinum clusters in zeolites for high-temperature catalysis. *Nature Materials*, 18(8):866–873, 2019. doi: 10.1038/s41563-019-0412-6.

[20] Manuel Munoz, Pierre Argoul, and Francois Farges. Continuous Cauchy wavelet transform analyses of EXAFS spectra: A qualitative approach. *American Mineralogist*, 88(4):694–700, apr 2003. doi: 10.2138/am-2003-0423.

[21] G Kresse and J Hafner. Ab initio molecular dynamics for liquid metals. *Physical Review B*, 47(1):558–561, jan 1993. doi: 10.1103/PhysRevB.47.558.

[22] Stefano Prada, Livia Giordano, and Gianfranco Pacchioni. Charging of Gold Atoms on Doped MgO and CaO: Identifying the Key Parameters by DFT Calculations. *The Journal of Physical Chemistry C*, 117(19):9943–9951, may 2013. doi: 10.1021/jp401983m.

[23] Jonathan Lym, Gerhard R Wittreich, and Dionisios G Vlachos. A Python Multiscale Thermochemistry Toolbox (pMuTT) for thermochemical and kinetic parameter estimation. *Computer Physics Communications*, 247:106864, 2020. doi: https://doi.org/10.1016/j.cpc.2019.106864.

[24] Ask Hjorth Larsen, Jens Jørgen Mortensen, Jakob Blomqvist, Ivano E Castelli, Rune Christensen, Marcin Dułak, Jesper Friis, Michael N Groves, Bjørk Hammer, Cory Hargus, Eric D Hermes, Paul C Jennings, Peter Bjerre Jensen, James Kermode, John R Kitchin, Esben Leonhard Kolsbjerg, Joseph Kubal, Kristen Kaasbjerg, Steen Lysgaard, Jón Bergmann Maronsson, Tristan Maxson, Thomas Olsen, Lars Pastewka, Andrew Peterson, Carsten Rostgaard, Jakob Schiøtz, Ole Schütt, Mikkel Strange, Kristian S Thygesen, Tejs Vegge, Lasse Vilhelmsen, Michael Walter, Zhenhua Zeng, and Karsten W Jacobsen. The atomic simulation environment—a Python library for working with atoms. *Journal of Physics: Condensed Matter*, 29(27):273002, 2017. doi: 10.1088/1361-648X/aa680e.

[25] Matthew Newville. Larch: An Analysis Package for XAFS and Related Spectroscopies. *Journal of Physics: Conference Series*, 430(1):0–7, 2013. doi: 10.1088/1742-6596/430/1/012007.

[26] Bidyut B Sarma, Philipp N Plessow, Giovanni Agostini, Patricia Concepción, Norbert Pfänder, Liqun Kang, Feng R Wang, Felix Studt, and Gonzalo Prieto. Metal-Specific Reactivity in Single-Atom Catalysts: CO Oxidation on 4d and 5d Transition Metals Atomically Dispersed on MgO. *Journal of the American Chemical Society*, 142(35):14890–14902, sep 2020. doi: 10.1021/jacs.0c03627.

[27] Fernando D Vila, J J Rehr, H H Rossner, and H J Krappe. Theoretical x-ray absorption Debye-Waller factors. *Physical Review B*, 76(1):14301, jul 2007. doi: 10.1103/PhysRevB.76.014301.

[28] Fernando D Vila, Scott T Hayashi, and John J Rehr. Efficient Calculation of the Negative Thermal Expansion in ZrW2O8 , 2018.

[29] James E Penner-Hahn. X-ray Absorption Spectroscopy. In *eLS*. John Wiley 'I&' Sons, Ltd, may 2005. ISBN 9780470015902. doi: https://doi.org/10.1038/npg.els.0002984.

[30] Hemma Mistry, Farzad Behafarid, Simon R Bare, and B Roldan Cuenya. Pressure-Dependent Effect of Hydrogen Adsorption on Structural and Electronic Properties of Pt/γ-Al2O3 Nanoparticles. *ChemCatChem*, 6(1):348–352, jan 2014. doi: https://doi.org/10.1002/cctc.201300783.

[31] Adam S Hoffman, Dimosthenis Sokaras, Shengjie Zhang, Louise M Debefve, Chia-Yu Fang, Alessandro Gallo, Thomas Kroll, David A Dixon, Simon R Bare, and Bruce C Gates. High-Energy-Resolution X-ray Absorption Spectroscopy for Identification of Reactive Surface Species on Supported Single-Site Iridium Catalysts. *Chemistry – A European Journal*, 23(59):14760–14768, oct 2017. doi: https://doi.org/10.1002/chem.201701459.

[32] Florian Maurer, Jelena Jelic, Junjun Wang, Andreas Gänzler, Paolo Dolcet, Christof Wöll, Yuemin Wang, Felix Studt, Maria Casapu, and Jan-Dierk Grunwaldt. Tracking the formation, fate and consequence for catalytic activity of Pt single sites on CeO2. *Nature Catalysis*, 3(10):824–833, 2020. doi: 10.1038/s41929-020-00508-7.

[33] John J Rehr, Joshua J Kas, Micah P Prange, Adam P Sorini, Yoshinari Takimoto, and Fernando Vila. Ab initio theory and calculations of X-ray spectra. *Comptes Rendus Physique*, 10(6):548–559, 2009. doi: https://doi.org/10.1016/j.crhy.2008.08.004.

[34] John J Rehr, Joshua J Kas, Fernando D Vila, Micah P Prange, and Kevin

Jorissen. Parameter-free calculations of X-ray spectra with FEFF9. *Physical Chemistry Chemical Physics*, 12(21):5503–5513, 2010. doi: 10.1039/B926434E.

[35] Anders Hellman, Simon Klacar, and Henrik Grönbeck. Low temperature co oxidation over supported ultrathin mgo films. *Journal of the American Chemical Society*, 131(46):16636–16637, 2009. doi: 10.1021/ja906865f.

[36] Melike Babucci, Adisak Guntida, and Bruce C Gates. Atomically Dispersed Metals on Well-Defined Supports including Zeolites and Metal–Organic Frameworks: Structure, Bonding, Reactivity, and Catalysis. *Chemical Reviews*, 120 (21):11956–11985, nov 2020. doi: 10.1021/acs.chemrev.0c00864.

[37] Adam S Hoffman, Joseph A Singh, Stacey F Bent, and Simon R Bare. In situ observation of phase changes of a silica-supported cobalt catalyst for the Fischer–Tropsch process by the development of a synchrotron-compatible in situ/operando powder X-ray diffraction cell. *Journal of Synchrotron Radiation*, 25(6):1673–1682, nov 2018. doi: 10.1107/S1600577518013942.

[38] Fernando D Vila, John J Rehr, Shelly D Kelly, and Simon R Bare. Operando Effects on the Structure and Dynamics of PtnSnm/γ-Al2O3 from Ab Initio Molecular Dynamics and X-ray Absorption Spectra. *The Journal of Physical Chemistry C*, 117(24):12446–12457, jun 2013. doi: 10.1021/jp403931z.

[39] F Vila, J J Rehr, J Kas, R G Nuzzo, and A I Frenkel. Dynamic structure in supported Pt nanoclusters: Real-time density functional theory and x-ray spectroscopy simulations. *Physical Review B*, 78(12):121404, sep 2008. doi: 10.1103/PhysRevB.78.121404.

[40] J J Kas, J Vinson, N Trcera, D Cabaret, E L Shirley, and J J Rehr. Many-pole

model of inelastic losses applied to calculations of XANES. *Journal of Physics: Conference Series*, 190(1):12009, 2009. doi: 10.1088/1742-6596/190/1/012009.

2.7 Supporting Information

Table 2.S1. Radar Plot Scoring Metrics

Structure	**HERFD-XANES Fréchet**	**Pt oxidation state**	**Boltzmann fraction for each facet (%)**	**Fractional contribution to overall EXAFS (%)**	**EXAFS Reduced-χ^2**	**EXAFS Fréchet**
[100]$^{\text{Mg-vac}}$/sub1	75	78	100	80	86	99
[100]/sub0/*O_2	83	13	100	15	78	93
[310]/pos1/*O_2	58	39	100	5	72	36

Each metric in the radar plot is determined computationally and is given a score from 0–100 to show how well the metric compares with the corresponding experimental result. The metrics are scored as: **HERFD-XANES Fréchet:** Percentile score of Fréchet distance for all FEFFsimulated XANES spectra compared with HERFD-XANES data (shown in Figure 2.S12); 0 represents the highest calculated Fréchet distance (worst match with experiment), and 100 represents the lowest Fréchet distance (best match with experiment). **Pt oxidation state:** Deviation of Pt oxidation state from +4 as determined from Bader charge analysis compared to $H_2Pt(OH)_6$ reference. **Boltzmann fraction for each facet:** DFT-calculated Boltzmann fraction relative to each facet ([100], [100]Mg-vac, and [310]) at 300 K as presented in the phase diagrams of Figure 2.3e-f. **Fractional contribution to overall EXAFS:** Contribution of the most stable structure from the 3 facets to the EXAFS data (see Figure 2.S20 for further discussion). **EXAFS Fréchet and Reduced-χ^2:** Percentile scores of Fréchet distances and Reduced-χ^2 values for EXAFS simulations.

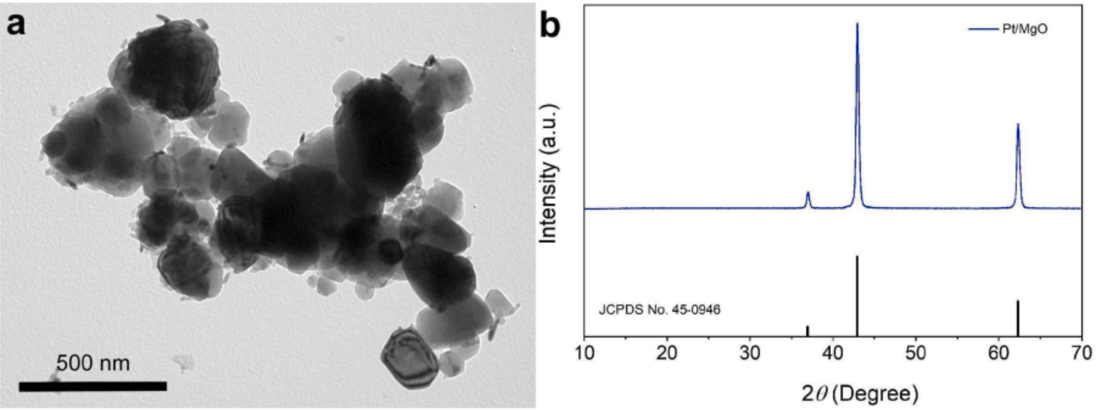

Figure 2.S1. TEM image and XRD pattern of Pt/MgO.

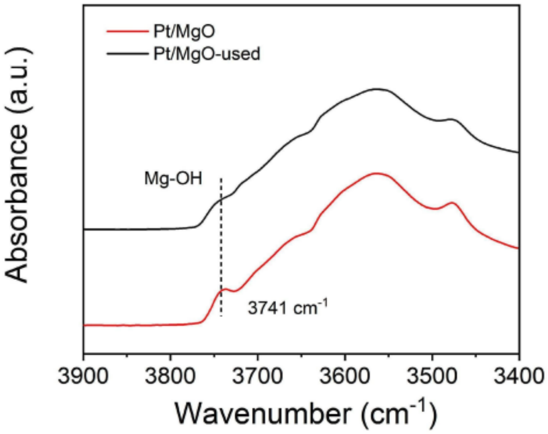

Figure 2.S2. IR spectra of ν_{O-H} region of Pt/MgO and the sample after use as a CO oxidation catalyst in three independent light-off experiments.

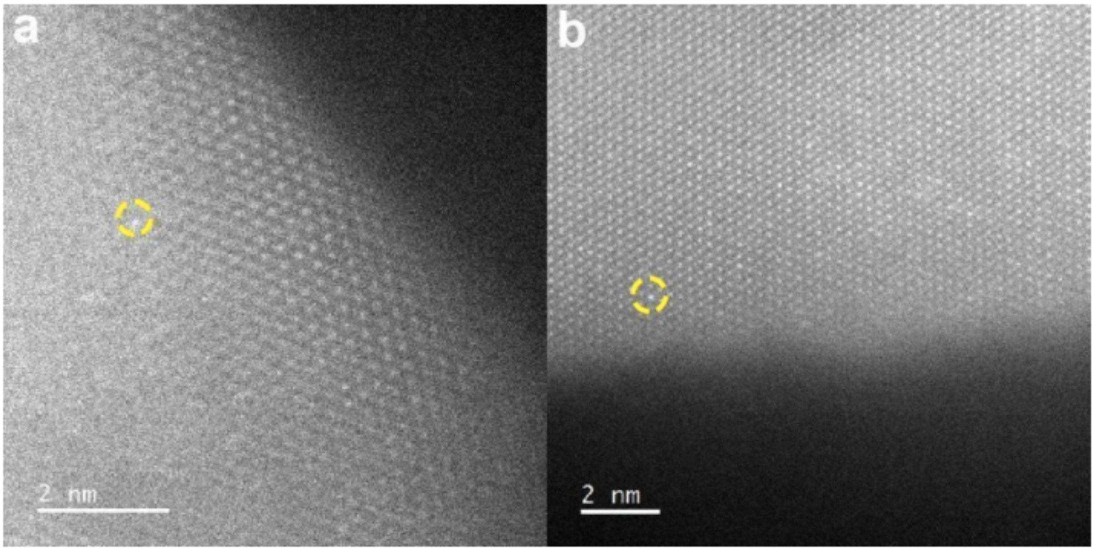

Figure 2.S3. Multiple HAADF-STEM images of Pt/MgO samples showing that the MgO supported platinum (yellow circles) was atomically dispersed.

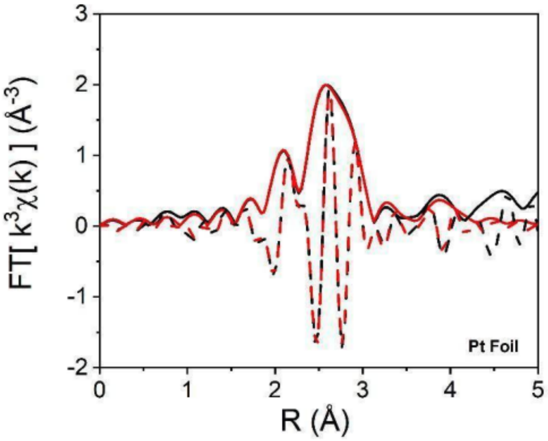

Figure 2.S4. EXAFS data at Pt L3 edge and EXAFS modelling of platinum foil. The data and the fits are shown in black and red, respectively. The magnitude and the imaginary portions of the Fourier transforms are shown as solid and dashed lines, respectively (k2-weighted).

Table 2.S2. Summary of EXAFS fit parameters for Pt foil reference.

Sample	Shell	CN^a	R^a (Å)	$\Delta\sigma^2$ (x10^3)^a (Å^2)	$\Delta E_0{}^a$ (eV)	$S_0{}^2$	R-factor
Pt foil	Pt–Pt$_1$	12.0	2.76 (0.00)	4.2 (0.3)	7.8 (0.6)	0.79 (0.06)	1.0 %
	Pt–Pt$_2$	6.0	3.91 (0.01)	6.4 (1.1)			

[a] *CN*, coordination number; *R*, distance between absorber and scatterer atoms; $\Delta\sigma^2$, disorder term; ΔE_0, inner potential correction. Details of data analysis for Pt foil: *k* range: 3.65–13.76 Å^{-1}; *R* range: 1–4.2 Å. Error is reported inside the parentheses (accuracies).

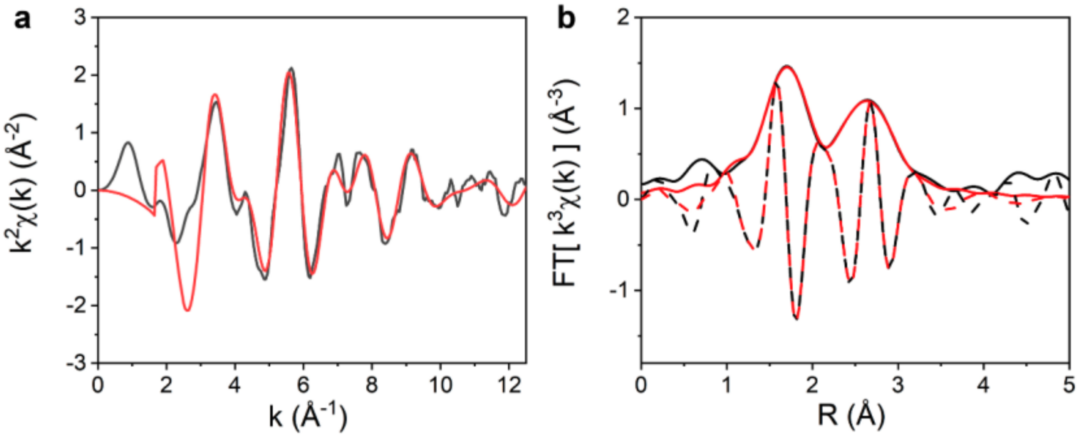

Figure 2.S5. EXAFS collected at the Pt L3 edge characterizing the Pt/MgO sample [black] and the best-fit EXAFS model (3-scattering path) representing the data [red] presented in the k2-weighted (a) EXAFS and (b) magnitude and imaginary components of the Fourier transform.

Table 2.S3. Best fit mdoel characterizing Pt L3 edge EXAFS of Pt/MgO sample.

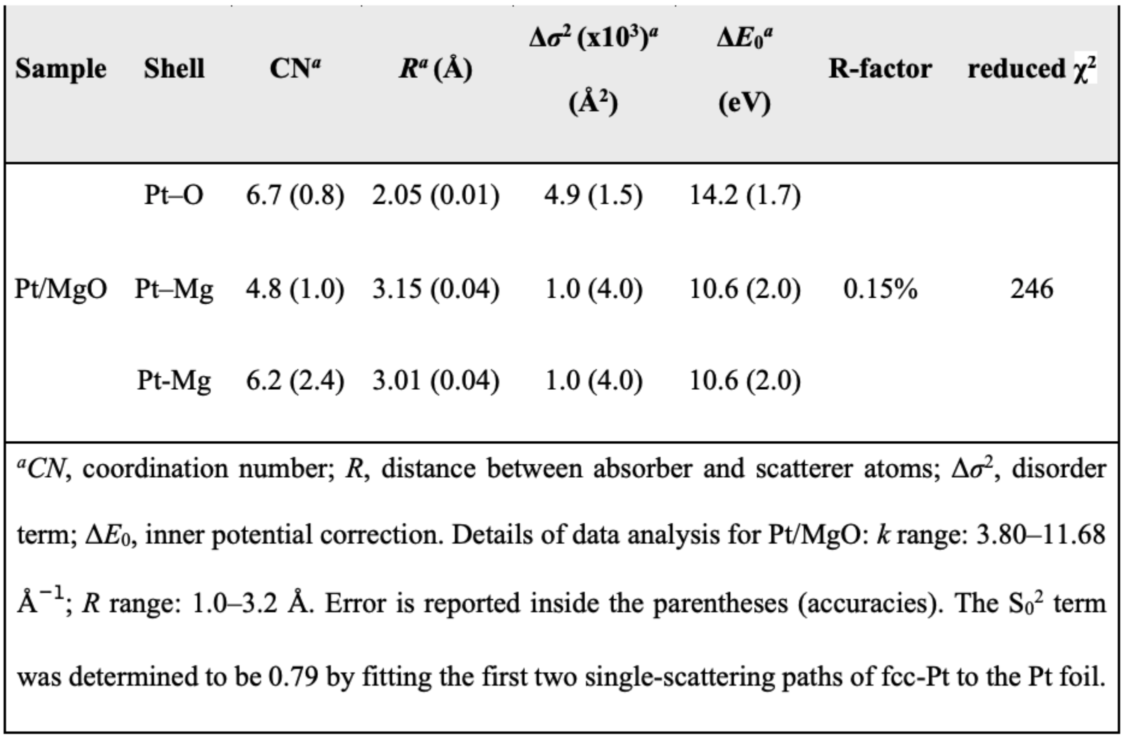

Sample	**Shell**	**CN**^{a}	$\boldsymbol{R}^a$ **(Å)**	$\boldsymbol{\Delta\sigma^2}$ **(x10^3)**^{a} **(Å^2)**	$\boldsymbol{\Delta E_0}^a$ **(eV)**	**R-factor**	**reduced χ^2**
Pt/MgO	Pt–O	6.7 (0.8)	2.05 (0.01)	4.9 (1.5)	14.2 (1.7)	0.15%	246
	Pt–Mg	4.8 (1.0)	3.15 (0.04)	1.0 (4.0)	10.6 (2.0)		
	Pt-Mg	6.2 (2.4)	3.01 (0.04)	1.0 (4.0)	10.6 (2.0)		

[a] *CN*, coordination number; *R*, distance between absorber and scatterer atoms; $\Delta\sigma^2$, disorder term; ΔE_0, inner potential correction. Details of data analysis for Pt/MgO: *k* range: 3.80–11.68 Å^{-1}; *R* range: 1.0–3.2 Å. Error is reported inside the parentheses (accuracies). The S_0^2 term was determined to be 0.79 by fitting the first two single-scattering paths of fcc-Pt to the Pt foil.

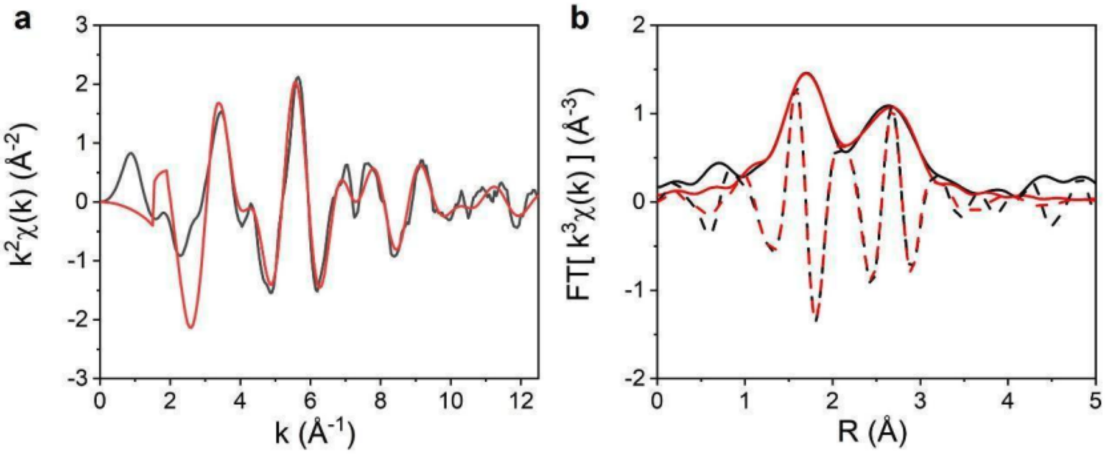

Figure 2.S6. EXAFS collected at the Pt L3 edge characterizing the Pt/MgO sample [black] and the 2-scattering path EXAFS model representing the data [red] presented in the k2-weighted (a) EXAFS and (b) magnitude and imaginary components of the Fourier transform.

Table 2.S4. 2-scattering path EXAFS model characterizing the Pt L3 edge EXAFS of the Pt/MgO sample.

Sample	**Shell**	**CN**^{a}	R^a (Å)	$\Delta\sigma^2$ (x10^3)^a (Å^2)	$\Delta E_0{}^a$ (eV)	**R-factor**	**reduced** χ^2
Pt/MgO	Pt–O	7.0 (0.7)	2.05 (0.01)	5.4 (1.3)	13.8 (1.4)	0.47%	194
	Pt–Mg	12.3 (1.5)	3.05 (0.01)	8.0 (1.6)	8.9 (1.2)		

^{a}*CN*, coordination number; *R*, distance between absorber and scatterer atoms; $\Delta\sigma^2$, disorder term; ΔE_0, inner potential correction. Details of data analysis for Pt/MgO: *k* range: 3.80–11.65 Å^{-1}; *R* range: 1.0–3.2 Å. Error is reported inside the parentheses (accuracies). The $S_0{}^2$ term was determined to be 0.79 by fitting the first two single-scattering paths of fcc-Pt to the Pt foil.

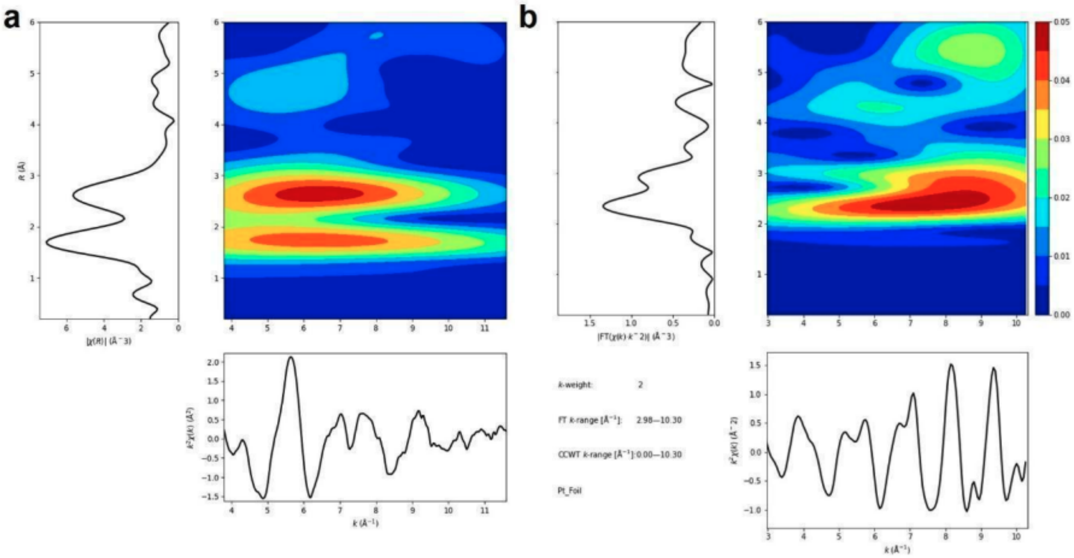

Figure 2.S7. k2-weighted CCWT of (a) Pt/MgO sample (k2-weighted EXAFS of the sample presented in the bottom plot. A k-range of 3.80-11.65 $\mathring{A}^{-1}$ was used to generate the magnitude of the Fourier transform, left plot.); (b) Pt foil (k2-weighted EXAFS of the sample presented in the bottom plot. A k-range of 2.98-10.30 $\mathring{A}^{-1}$ was used to generate the magnitude of the Fourier transform, left plot).

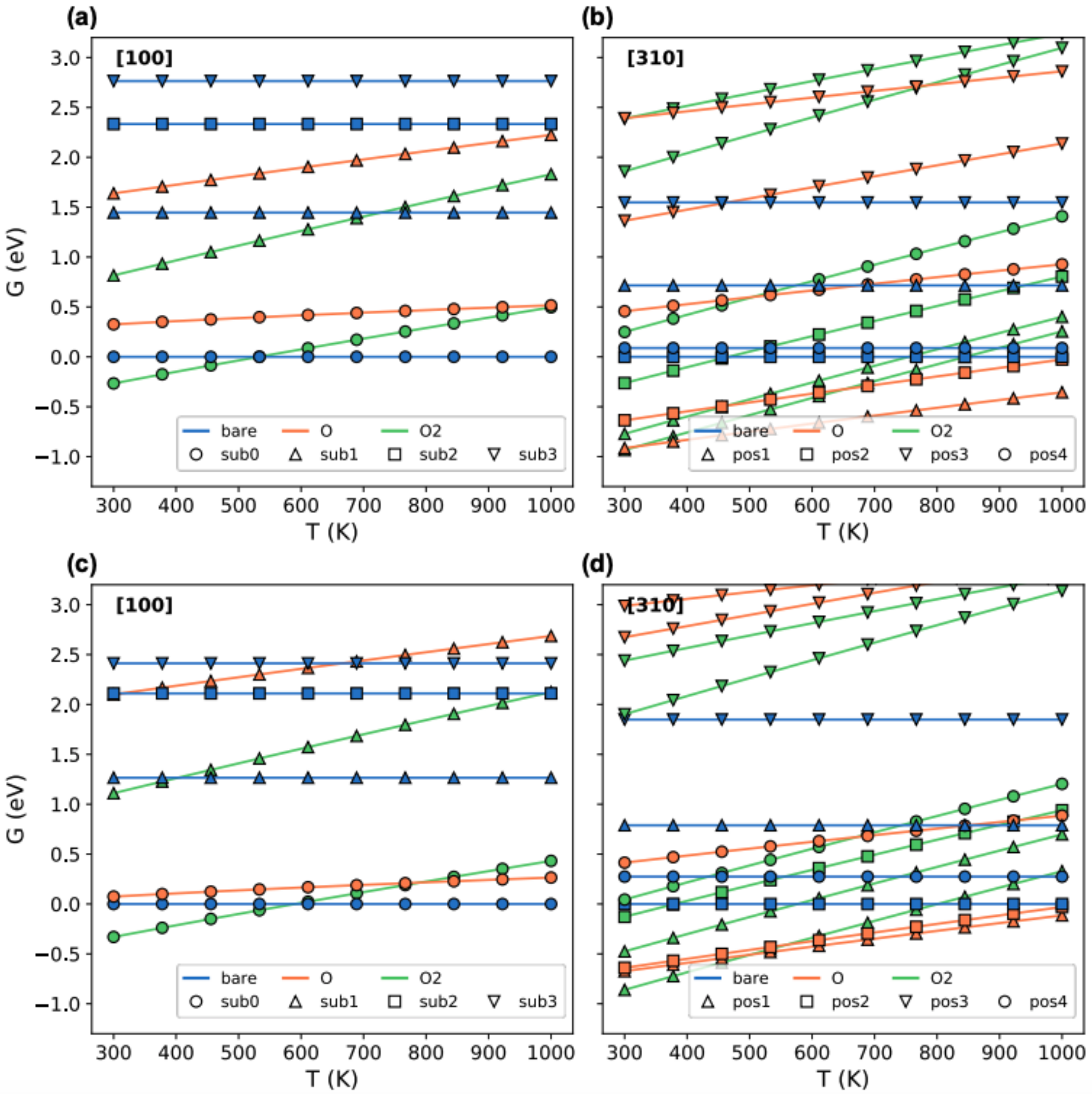

Figure 2.S8. PBE-D3BJ calculated temperature-dependent phase diagrams for (a) [100] and (b) [310] structures. RPBE-D3BJ calculated temperature-dependent phase diagrams for (c) [100] and (d) [310] structures.

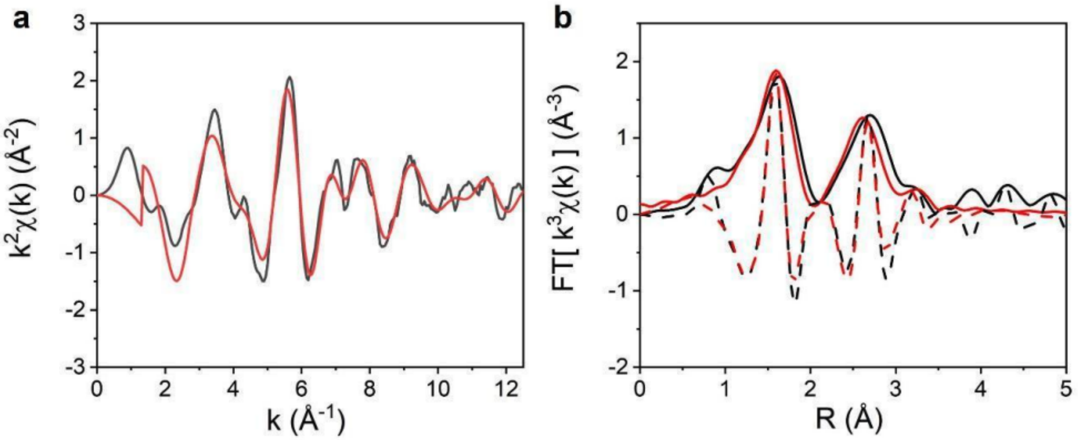

Figure 2.S9. EXAFS collected at the Pt L3 edge characterizing the Pt/MgO sample [black] and the fits performed using [100]Mg-vac DFT structure representing the data [red] presented in the k2-weighted (a) EXAFS and (b) magnitude and imaginary components of the Fourier transform.

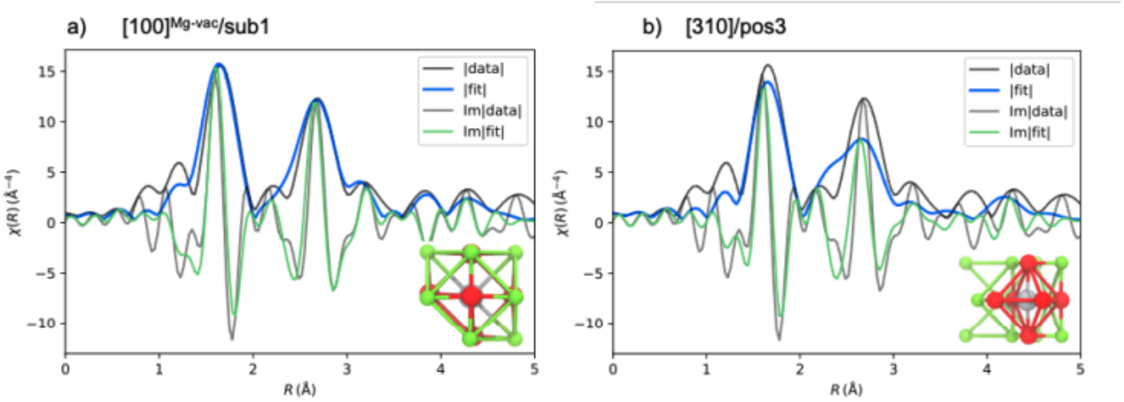

Figure 2.S10. Illustration of the capability of our fitting approach to capture the anisotropic behavior of structures with the same coordination number (Pt-O = 6 and Pt-Mg = 11). R-space EXAFS fits of (a) [100]Mg-vac/sub1 and (b) [310]/pos3 showing the magnitude and imaginary portions of experimental results in black and the magnitude and imaginary portions of the model in blue and green, respectively. The k-range of 2.2–12.5 Å^{-1} and the R-range of 1.0–5.0 Å were used for the fits. Colors: Mg (green), O (red), Pt (grey).

Table 2.S5. The EXAFS fitting parameters using [100]Mg-vac/sub1 as the DFT model structure.

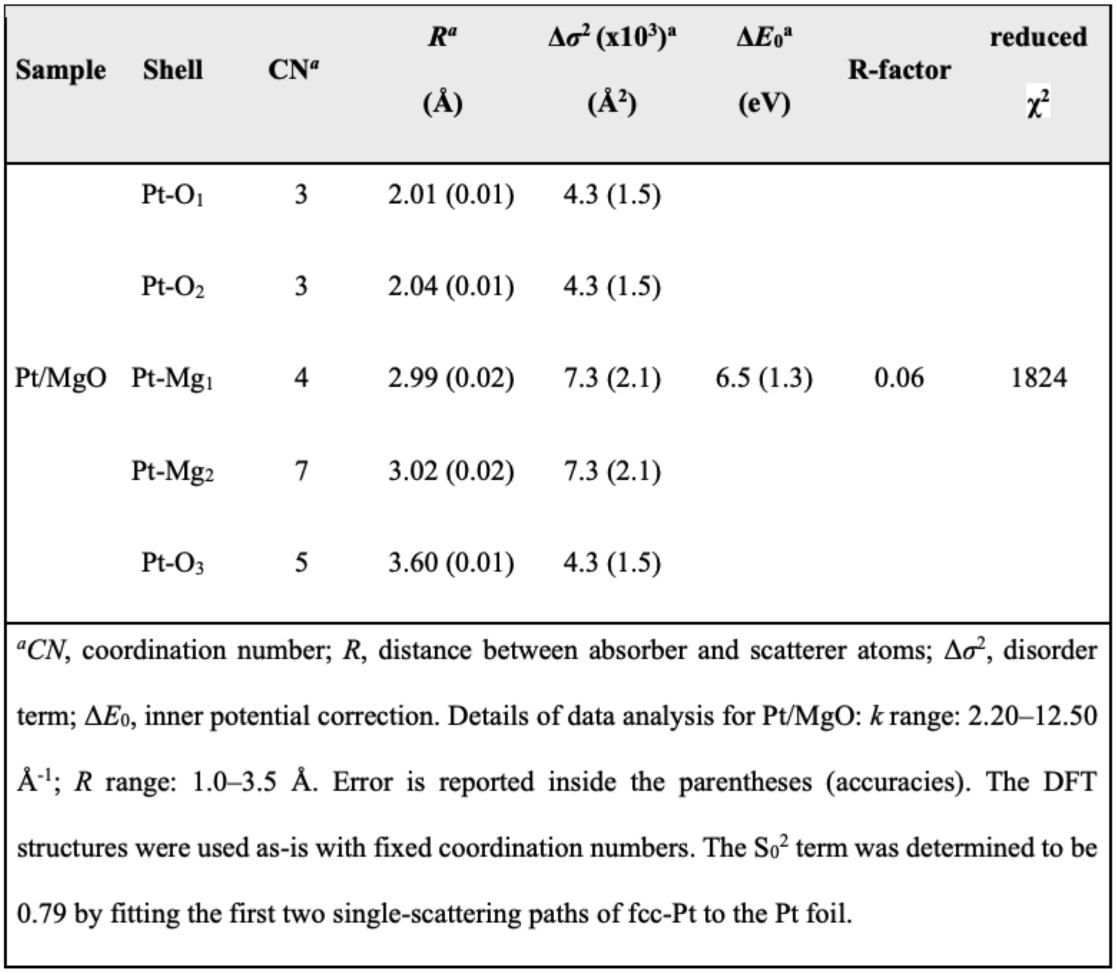

Sample	Shell	CN^a	R^a (Å)	$\Delta\sigma^2$ (x10^3)^a (Å^2)	ΔE_0^{a} (eV)	R-factor	reduced χ^2
Pt/MgO	Pt-O_1	3	2.01 (0.01)	4.3 (1.5)	6.5 (1.3)	0.06	1824
	Pt-O_2	3	2.04 (0.01)	4.3 (1.5)			
	Pt-Mg_1	4	2.99 (0.02)	7.3 (2.1)			
	Pt-Mg_2	7	3.02 (0.02)	7.3 (2.1)			
	Pt-O_3	5	3.60 (0.01)	4.3 (1.5)			

^{a}*CN*, coordination number; *R*, distance between absorber and scatterer atoms; $\Delta\sigma^2$, disorder term; ΔE_0, inner potential correction. Details of data analysis for Pt/MgO: *k* range: 2.20–12.50 Å^{-1}; *R* range: 1.0–3.5 Å. Error is reported inside the parentheses (accuracies). The DFT structures were used as-is with fixed coordination numbers. The S_0^2 term was determined to be 0.79 by fitting the first two single-scattering paths of fcc-Pt to the Pt foil.

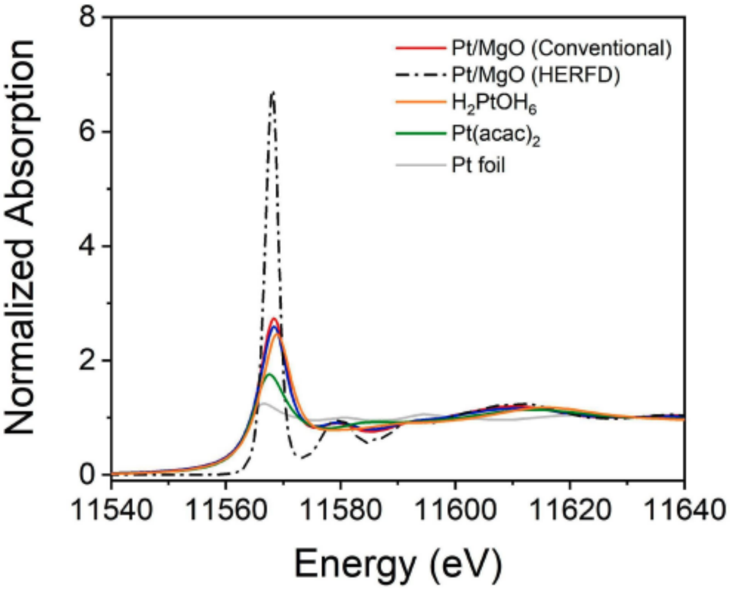

Figure 2.S11. HERFD-XANES spectrum at the Pt L3 edge of Pt/MgO (black dash dot line) and conventional XANES spectra at the Pt L3 edge of Pt/MgO (red line); $H_2Pt(OH)_6$ (orange line); $Pt(acac)_2$ (green line); and Pt foil (grey line). Data were obtained at room temperature under static conditions.

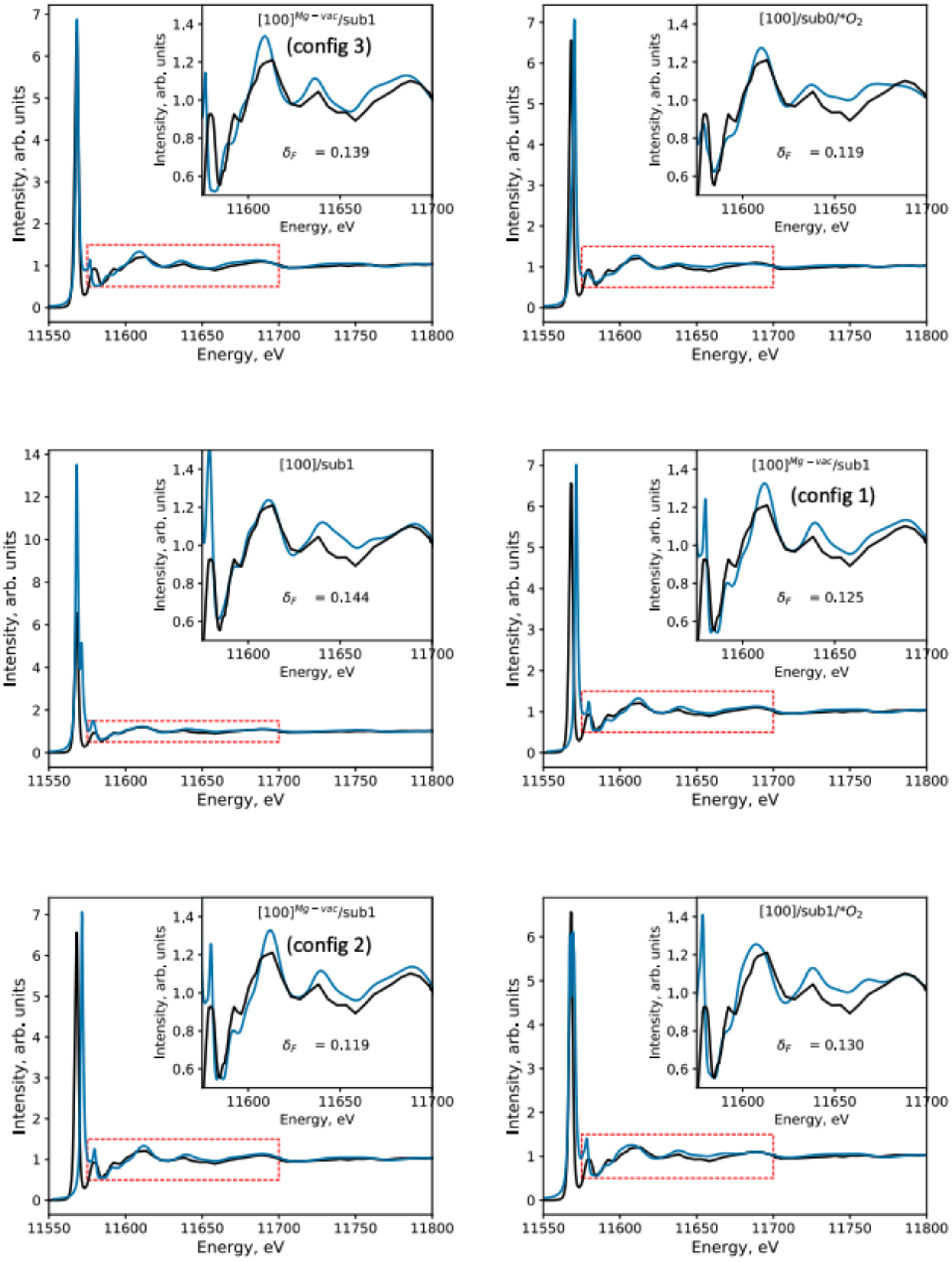

Figure 2.S12. FEFF-simulated XANES spectra (blue) and experimental HERFD-XANES results (black) for feasible DFT-calculated structures. Insets denote the region from 11575–11700 eV (dashed red box).

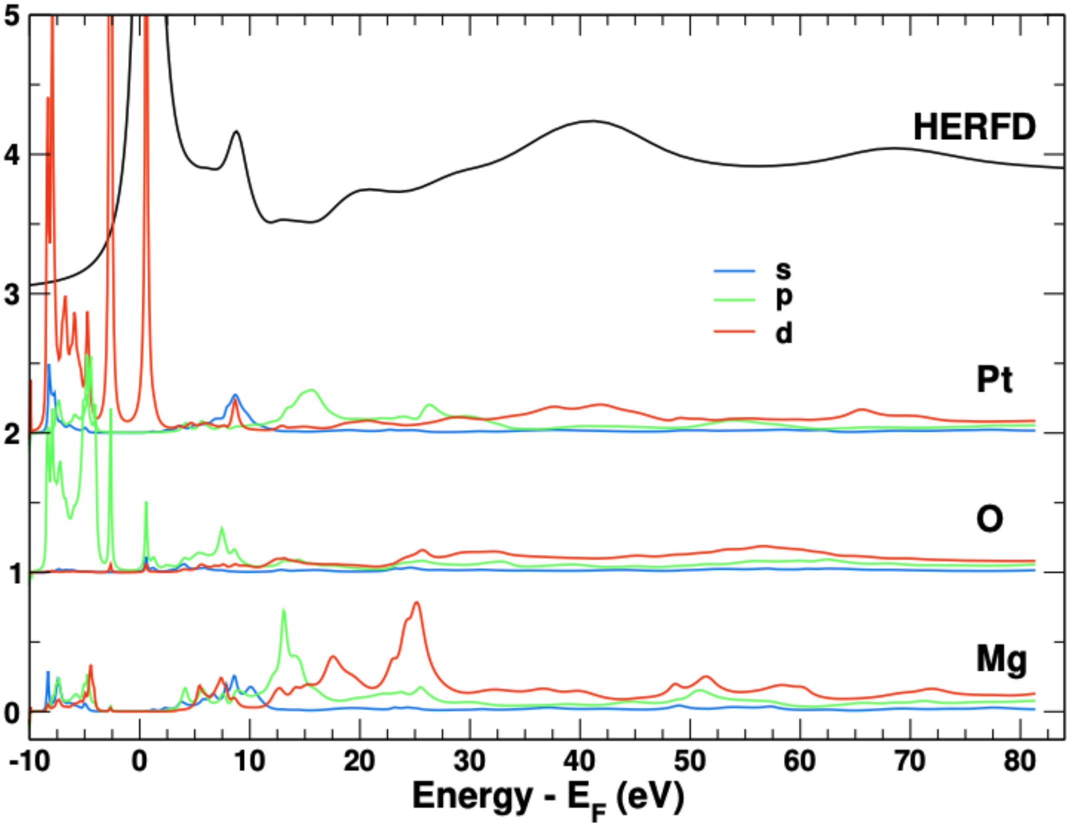

Figure 2.S13. Locally projected, l-dependent density of states for [100]Mg-vac/sub1 site with HERFD-XANES spectrum relative to the Fermi level (E_F).

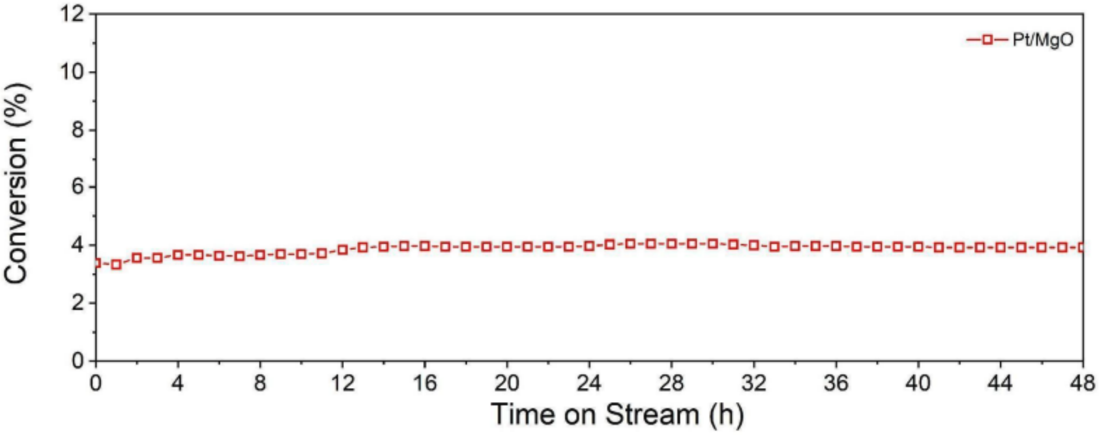

Figure 2.S14. Stability of Pt/MgO catalyst for CO oxidation in a once-through flow reactor operated at 210 °C and atmospheric pressure with a steady flow of reactant consisting of 5.0% CO in helium flowing at a rate of 4.0 mL(NTP)/min and 5.0% O_2 in helium flowing at a rate of 16.0 mL(NTP)/min.

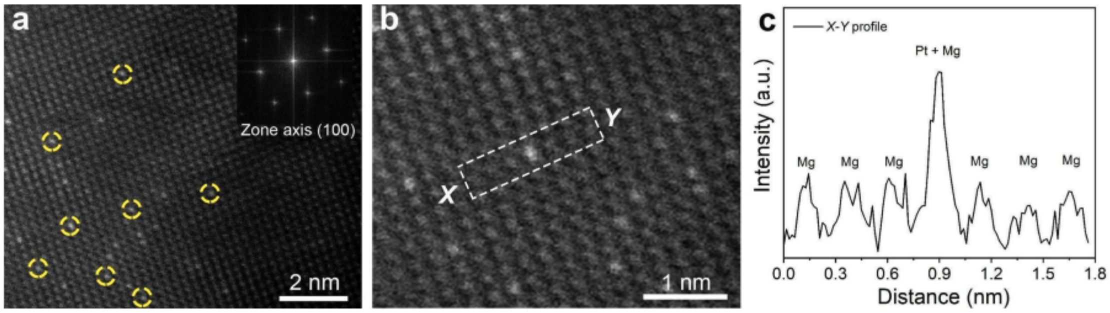

Figure 2.S15. (a) HAADF-STEM image of Pt/MgO-used sample (Pt/MgO after it had been used as a catalyst in three independent light-off CO oxidation measurements) along the (100) zone axis. Pt atoms are marked in yellow circles; the inset shows the corresponding FFT pattern. (b) Magnified HAADF-STEM image of a. (c) Corresponding intensity profile from the X–Y line scan in b.

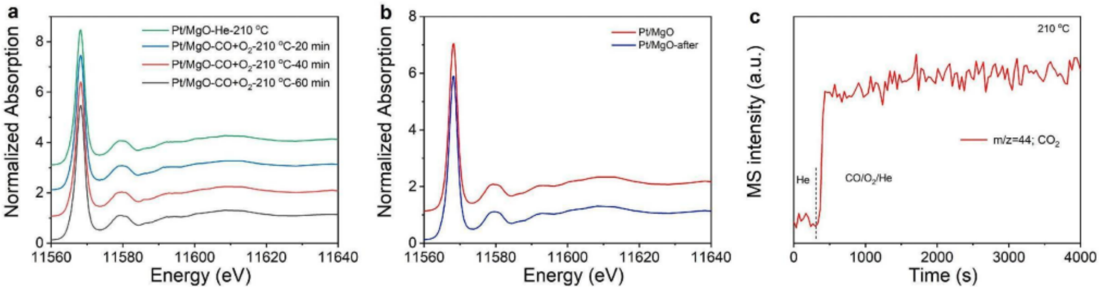

Figure 2.S16. In-operando HERFD-XANES spectra at the Pt L3 edge of Pt/MgO and mass spectrometry results. (a) HERFD-XANES data collected at 210 °C with the sample (approximately 50 mg) in helium flowing at 20 mL(NTP)/min and then after replacement of the helium stream with a mixture of CO flowing at 0.2 mL(NTP)/min + O_2 flowing at 0.8 mL(NTP)/min + He flowing at 19 mL(NTP)/min for 1 h. (b) HERFD-XANES spectra collected with sample in helium flowing at 20 mL(NTP)/min at room temperature; the data characterize Pt/MgO before and after it had been used as a catalyst for CO oxidation at 210 °C for 1 h. (c) Mass spectrometry results characterizing effluent gas recorded during in-operando HERFDXANES experiments (shown in a) characterizing Pt/MgO (mass 44 represents CO_2).

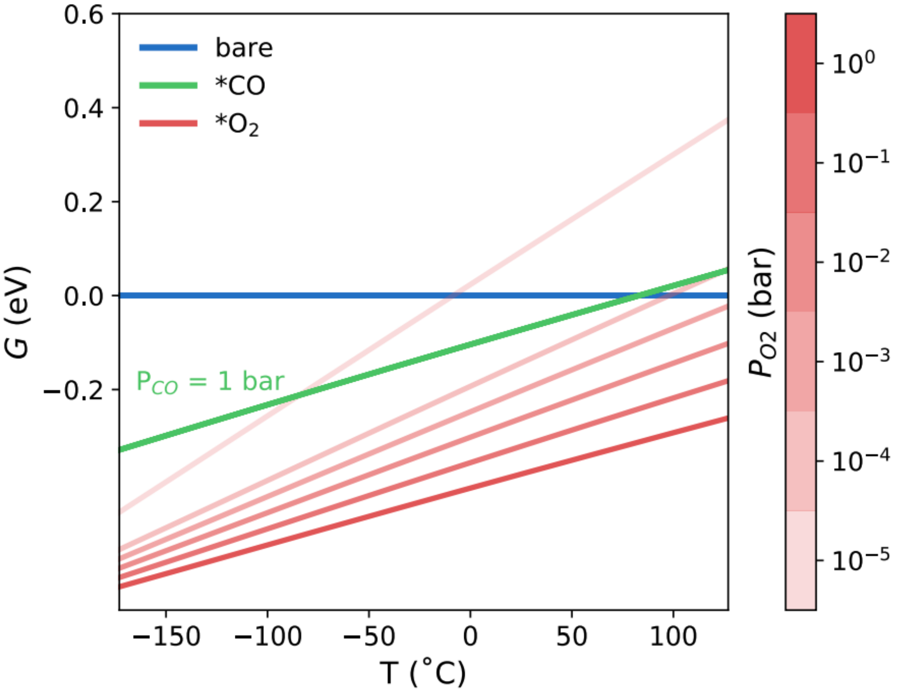

Figure 2.S17. PBESol-calculated temperature-dependent CO and O_2 adsorption on [100]/sub0 for O_2 partial pressures from 10^{-5} to 100 bar. CO adsorption is predicted until 83 °C is reached for low O_2 partial pressures.

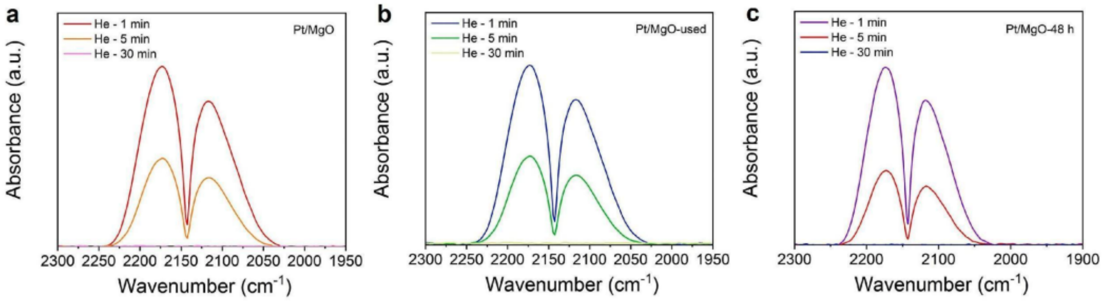

Figure 2.S18. IR spectra of (a) Pt/MgO; (b) Pt/MgO-used (Pt/MgO after it had been used as a catalyst in three independent light-off CO oxidation measurements); and (c) Pt/MgO-used (Pt/MgO after it had been used as a catalyst in three independent light-off CO oxidation measurements) in flowing helium recorded at 1, 5, and 30 min after the beginning of flow of 10% CO in helium at room temperature and 1 atm. The bands at 2174 and 2118 cm^{-}1 represent the gas-phase CO.

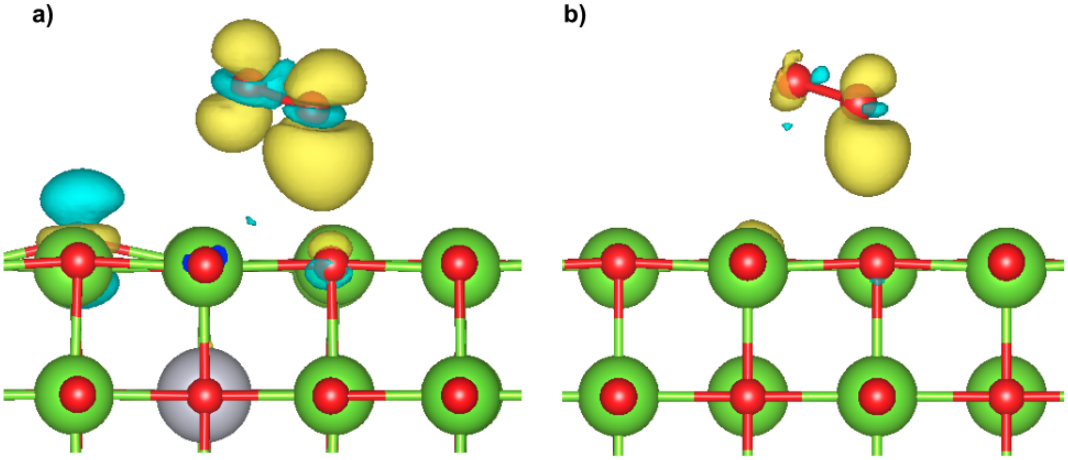

Figure 2.S19. Differences in charge density (±0.001 electron/Å^3) upon binding of O_2 on a) [100]Mg-vac/sub1 and b) pure ideally crystalline MgO. Charge gain and depletion are represented with yellow and blue, respectively. The depletion of charge between the O—O bond in Pt/ MgO enables CO insertion to form bound $*CO_3$ during CO oxidation catalysis.

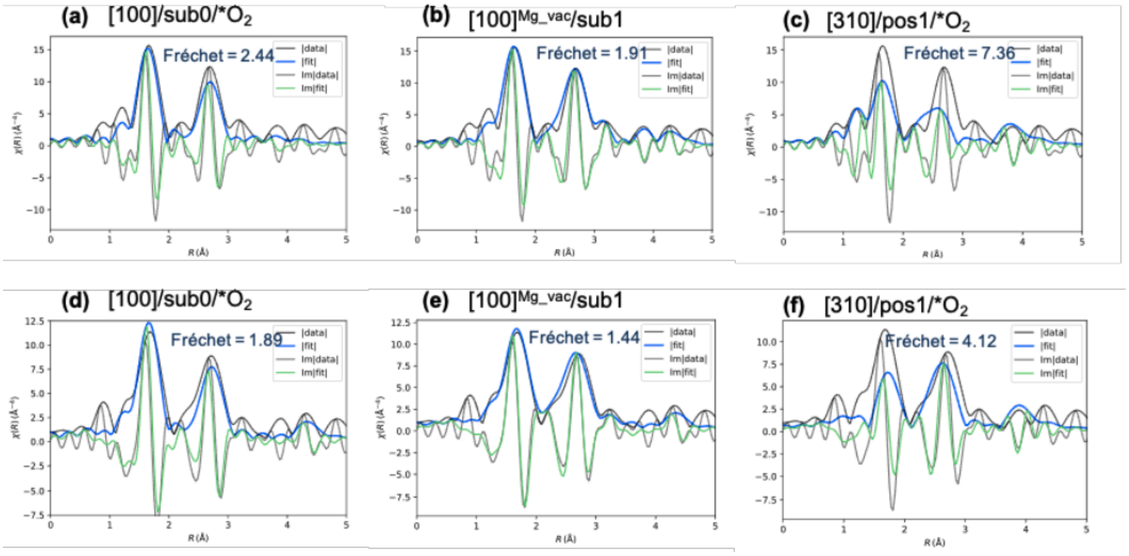

Figure 2.S20. EXAFS fits of Pt/MgO as is (a–c) (i.e., as synthesized before CO oxidation catalysis) and used (d–e) catalyst (i.e., after it had been used as a catalyst in three independent light-off CO oxidation measurements) for the three most stable structures [100]/sub0/$*O_2$, [100]Mg-vac/sub1, and [310]/pos1/$*O_2$ showing the magnitude and imaginary portions of Fourier transforms. The magnitude is shown with experimental results in black and the model in blue, and the imaginary portions are shown in black and green, respectively. The k-range of 2.2–12.5 Å^{-1} and the R-range of 1.0–5.0 Å were used for the fits.

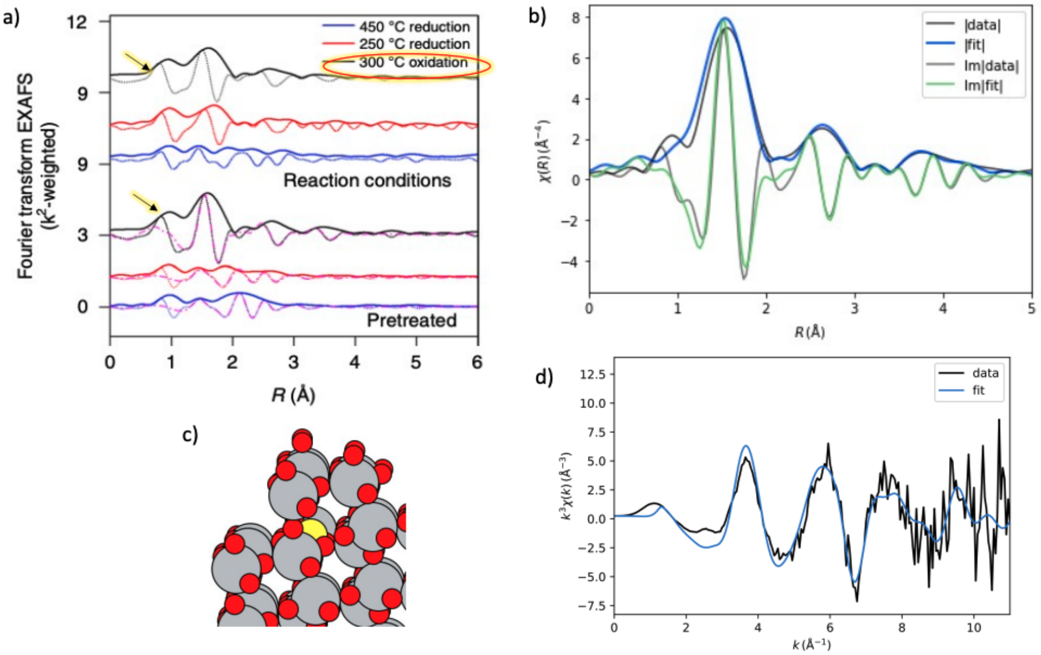

Figure 2.S21. Testing the applicability of QuantEXAFS on well-defined system (Pt/TiO$_2$) - a) EXAFS fits reported in the paper derived from conventional approach; EXAFS fits using QuantEXAFS on the same data (300 °C oxidation); fit from QuantEXAFS in b) R-space and d) k-space; c) DFT optimized structure used for fitting the data in QuantEXAFS ('hypothesized' to be representative of the Pt site in the original manuscript). Red: O, gray: Ti, and yellow: Pt. The k-range of 2.0–10.5 Å^{-1} and the R-range of 1.0–5.0 Å were used for the fits. Adapted with permission from DeRita et al., Nature Materials volume 18, pages 746–751. Copyright 2019 Springer Nature.

Chapter 3

Atomically Dispersed Platinum in Surface and Subsurface Sites on MgO Have Contrasting Catalytic Properties for CO Oxidation

Y. Chen#, R. Rana#, Z. Huang, F.D. Vila, T. Sours, J.E. Perez-Aguilar, X. Zhao, J. Hong, A.S. Hoffman, X. Li, C. Shang, T. Blum, J. Zeng, M. Chi, M. Salmeron, C.X. Kronawitter, S.R. Bare, A.R. Kulkarni, B.C. Gates

#Authors contributed equally. My contributions to this work consist of all theoretical calculations including the EXAFS and XANES spectra simulations– Figures 3.2 and 3.3 and Table 3.1 are from my contribution. All experimental work was performed by collaborators.

Adapted with permission from J. Phys. Chem. Lett., 2022, 13, 3896–3903.

3.1 Abstract

Atomically dispersed metals on metal oxide supports are a rapidly growing class of catalysts. Developing an understanding of where and how the metals are bonded to the supports is challenging because support surfaces are heterogeneous, and most reports lack a detailed consideration of these points. Herein, we report two atomically dispersed CO oxidation catalysts having markedly different metal-support interactions: platinum in the first layer of crystalline MgO powder and platinum in the second layer of this support. Structural models have been determined on the basis of data and computations, including those determined by extended X-ray absorption fine structure and X-ray absorption near edge structure spectroscopies, infrared spectroscopy of adsorbed CO, and scanning transmission electron microscopy. The data demonstrate the transformation of surface to subsurface platinum as the temperature of sample calcination increased. Catalyst performance data demonstrate the lower activity but greater stability of the subsurface platinum than of the surface platinum.

3.2 Introduction

Atomically dispersed noble metals on supports offer new catalytic properties as well as efficient use of the metals, but there is a lack of understanding of how these properties depend on the structures of the anchoring sites and the metal–support bonding.[1–4] Atomically dispersed supported metals are more nearly uniform than typical supported metal catalysts and therefore offer better opportunities for fundamental understanding.[1–4] In-operando spectroscopies and high-resolution imaging have emerged as the most informative characterization methods,[5–12] but the characterization challenges are formidable, complicated by the support surface heterogeneity and the strong tendency of atomically dispersed noble metals to be converted into metal clusters/nanoparticles under reducing conditions.[12,13] In almost all the reported work with atomically dispersed metals on metal oxide supports, the nature of the metal–support bonding has remained obscure, and the possibility of forming subsurface metal species has been largely overlooked.[3,14,15]

Herein, we report results of X-ray absorption spectroscopy (XAS), atomic-resolution electron microscopy, and density functional theory (DFT) calculations that demonstrate two distinct sites for atomically dispersed platinum on MgO. In addition to a recently reported site[3] for bonding platinum in the second layer of MgO—within the lattice—we now report platinum in a more accessible site in the first MgO layer. This newly discovered site is characterized by relatively high catalytic activity for CO oxidation but low stability. Further, we show that high-temperature calcination drives the platinum from the first MgO layer irreversibly into the second layer, where it is more stably bonded but barely accessible. These results demonstrate trade-offs between catalytic activity and stability.

3.3 Results and Discussion

Pt/MgO400 (the subscript is the calcination temperature in °C) was synthesized from K_2PtCl_4 slurried with MgO powder in ethanol-water solutions then dried and calcined in 20% O_2 in N_2 at 400 °C (Supporting Information).[3] Low metal loadings (approx. 0.05 wt%) were used in an attempt to minimize the number of different bonding sites for platinum on the support. Some of the Pt/MgO400 samples (referred to as Pt/MgO700) were subsequently calcined under more severe conditions, at 700 °C.

Transmission electron microscopy (TEM) images and X-ray diffraction (XRD) patterns show that the MgO was present as the cubic phase, consisting of 200-nm diameter crystallites; there was no evidence of crystalline metallic platinum or PtO2 (Figure 3.S1). Infrared (IR) bands of MgO surface OH groups (at 3766 and 3726 cm-1) decreased in intensity as the calcination temperature increased to 700 °C (Figure 3.S2); the resultant MgO was highly dehydroxylated.[3,16] O 1s X-ray photoelectron spectroscopy (XPS) peaks at 529.8 and 532.0 eV provide evidence of oxygen atoms in the MgO lattice and surface OH groups, respectively (Figure 3.S3).[17–19] The intensity of the 532.0 eV peak characterizing Pt/MgO700 is less than that characterizing

Pt/MgO400, consistent with IR data showing that MgO dehydroxylation took place during calcination (Figure 3.S4 and Table 3.S1). BET surface area measurements are consistent with these results.[16,20]

High-angle annular dark field (HAADF)-scanning TEM (STEM) images, Figure 3.1, show the presence of atomically dispersed platinum and the absence of clusters/nanoparticles in both Pt/MgO400 and Pt/MgO700. The bright spots in yellow circles in Figures 3.1a and 3.1d are illustrative, showing isolated platinum atoms, in agreement with reported results for the latter sample.[3] Intensity profiles along the X–Y lines in the images of Figures 3.1b and 3.1e reinforce the conclusions (Figure 3.1c and 3.1f).

The STEM images provide no information about the local bonding environment of the platinum, and so we used XAS, with in-operando spectra recorded at the platinum L_{III}-edge during the calcination as the temperature was ramped at 5 °C/min from room temperature to 700 °C with the sample in 20% O2 in helium flowing at a rate of 20 mL(NTP)/min. The X-ray absorption near edge spectra (XANES) include isosbestic points, indicating that the changes were stoichiometrically simple (Figure 3.2a). The white line intensity at the platinum L_{III}-edge characterizing the sample at room temperature in flowing helium, recorded after the 700ºC calcination, is markedly greater than that of the initial sample (Figure 3.2b), implying that the Pt species with lower oxidation state used in the synthesis was oxidized during the subsequent calcination.

Extended X-ray absorption fine structure (EXAFS) spectra at the platinum L_{III}-edge were recorded to determine the local bonding environment of the platinum before and after calcination (Figure 3.2e, 3.2f). Analysis of the data characterizing Pt/MgO400 was performed with a fitting procedure (referred to as QuantEXAFS)[3,21] that included all the relevant scattering paths in structures determined to be plausible by DFT.[22] The candidate models in the database included 47 DFT-optimized structures. The temperature-dependent phase diagram were constructed (using pMuTT, harmonic approximation for vibrational entropy) for each site (Figure 3.S5).[3,22–24] The DFT-optimized geometries (Figure 3.2c) and corresponding best fits of the data (Figure 3.2e and Table 3.1) indicate average Pt–O and Pt–Mg coordination numbers (CNPt–O and CNPt–Mg) of 6 and 8, respectively. The model that agrees best with the data, [100]/sub0/*O2 (Figure 3.2e and Table 3.1—see caption of Figure 3.2 for explanation of notation), corresponds to isolated platinum atoms on the stoichiometric [100] surface and bonded to five oxygen atoms of the MgO support and one oxygen atom inferred to have formed from O2 in the calcination treatment. In contrast, the data characterizing the sample calcined at 700 °C, PtMgO700, which were analyzed by the above-mentioned method (as already reported13) show that platinum was present in the first sub-surface layer located in the [100] MgO facet at Mg vacancy sites, with the coordination numbers CNPt–O and CNPt–Mg being 6 and 11, respectively (Figure 3.2f and Table 3.1). The corresponding DFT-optimized geometries ([100]Mg-vac/sub1) are shown in Figure 3.2d. Candidate EXAFS models that included at Pt–Pt scattering path led to nonsensical results indicating that there was no evidence of platinum clusters or nanoparticles.

The central point shown by comparing the EXAFS data characterizing the two differently calcined samples is that the Pt–O and Pt–Mg coordination numbers changed significantly as the calcination temperature increased from 400 to 700 °C, and the location of platinum changed from a bonding site in the first MgO layer to a bonding site in the second MgO layer.

To gain further insight into the structures and to help overcome the limitations associated with core-hole lifetime broadening in conventional XANES spectroscopy,[25,26] we also collected high energy resolution fluorescence detection (HERFD)-XANES

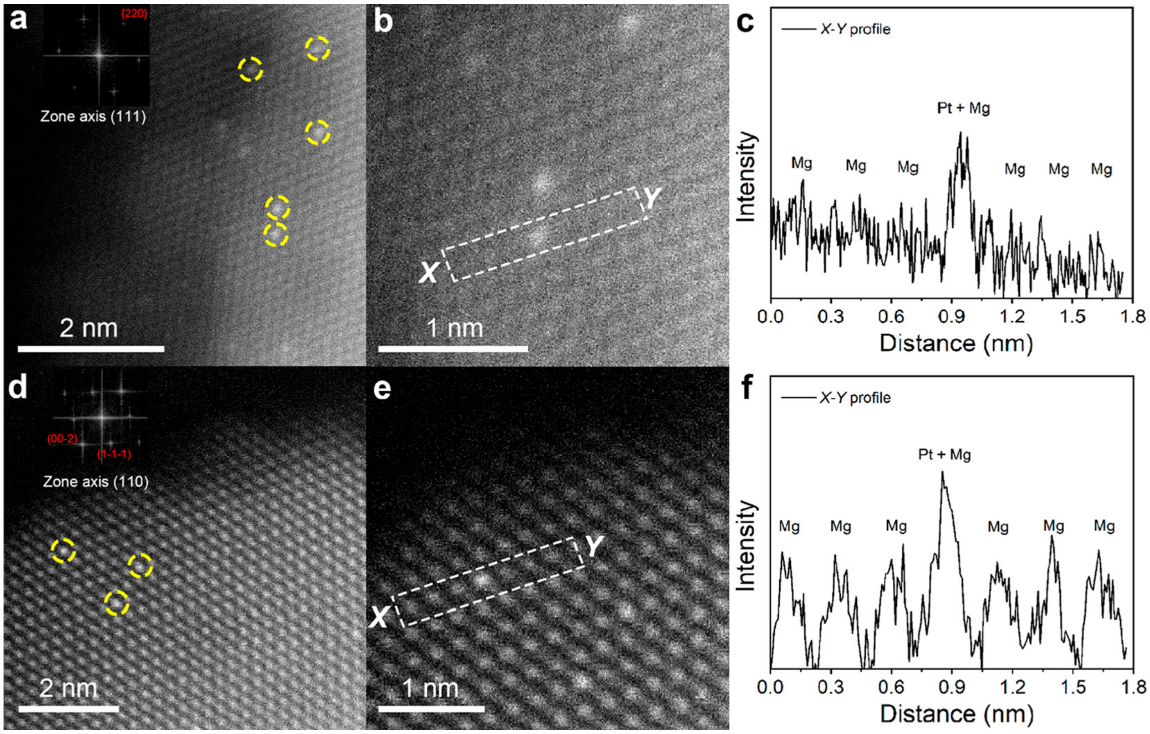

Figure 3.1. (a) HAADF-STEM image of Pt/MgO400 along the (111) zone axis. Platinum atoms are highlighted in yellow circles; the inset shows the corresponding fast Fourier transform (FFT) pattern. (b) Magnified HAADF-STEM image of Pt/MgO400. (c) Intensity profile along the X–Y axis in b. (d) HAADF-STEM image of Pt/MgO700 along the (110) zone axis. Platinum atoms are highlighted in yellow circles; the inset shows the corresponding FFT pattern. (e) Magnified HAADF-STEM image of Pt/MgO700. (f) Intensity profile along the line X–Y axis in e.

data. These data, when combined with simulated spectra, provide additional insight into the structure of the supported platinum. The HERFD-XANES data were compared with FEFF-simulated XANES spectra calculated from the above-mentioned DFT-optimized geometries (Figure 3.2g and 3.2h).[3,27,28] The structure [100]/sub0/*O2 is in good agreement with the HERFD-XANES data characterizing this sample (Figure 3.2g), with a Fréchet distance of 0.155. (Fréchet distances have been used previously to quantify the similarity between the experimental and simulated spectra.[3]) Further, the structure of [100]Mg-vac/sub1 is in good agreement with the HERFD-XANES results characterizing Pt/MgO700, as we reported before (Figure 2h).[3] Details are presented in Figure 3.S6.

The oxidation state of platinum in the subsurface sites, determined from DFT calculations using Bader charge analysis13 (qBader = +1.35e) is close to that of Pt^{4+} in $H_2Pt(OH)_6$ (qBader = +1.41e). Comparable calculations showed that the oxidation state of platinum in the first MgO layer (qBader = +1.17e) is between those of Pt^{2+} (qBader = +1.17e for Pt(acac)2) and Pt^{4+}, and thus lower than that of platinum in the second layer. These results are in good agreement with the XANES data showing that the white line intensity increased as the calcination temperature was raised from 400 to 700 °C (Figure 3.2a, 3.2b, 3.2g and 3.2h), and they are in good agreement with XANES data characterizing reference compounds (Figure 3.S8).

Table 3.1. EXAFS fitting parameters for Pt/MgO400 and Pt/MgO700 modelled using QuantEXAFS with the respective structures with the Pt–O and Pt–Mg coordination (the numbers on the sphere represent Pt–O and Pt–Mg bond distances in Å). Color scheme: O (red), Pt (gray), Mg (green), and Mg-vac (purple).

Sample	**Structures**		**ΔE_0 (eV)**	**$10^3 \times \sigma_i^2$ (Å^2)**	
Pt/MgO$_{400}$	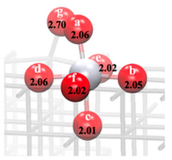	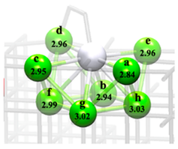	7.9 ± 1.3	Pt-O (7)	1.1 ± 0.5
				Pt-Mg (8)	1.3 ± 3.2
Pt/MgO$_{700}$	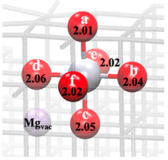	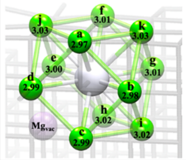	5.8 ± 1.6	Pt-O (6)	4.0 ± 1.1
				Pt-Mg (11)	4.9 ± 1.1

[a] The numbers on the spheres represent Pt−O and Pt−Mg bond distances in Å. Color scheme: O (red), Pt (gray), Mg (green), and Mg-vac (purple). Notation: ΔE_0 is the energy alignment parameter, and σ is the disorder term.

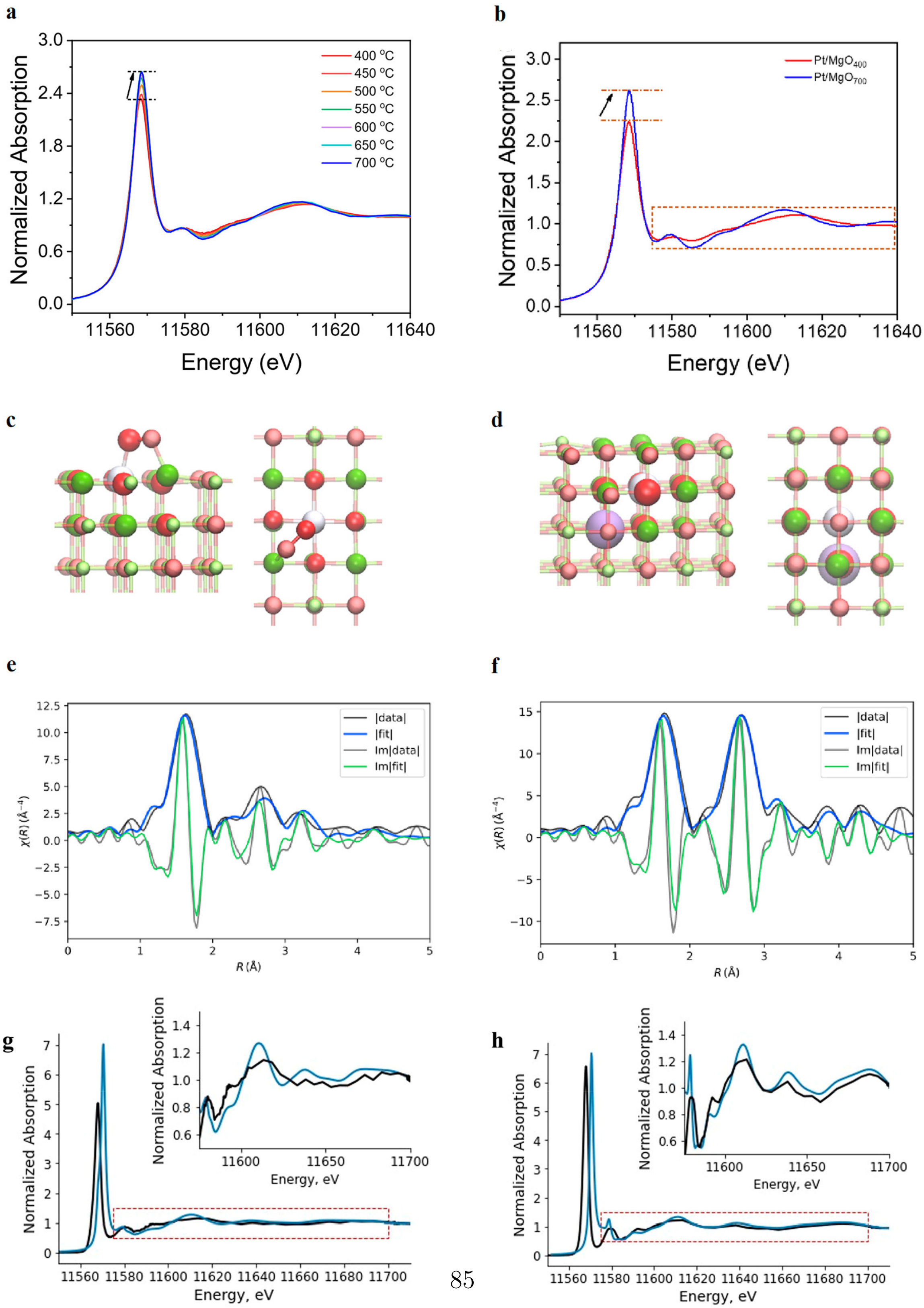

Figure 3.2. (Caption next page.)

Figure 3.2. (a) Conventional XANES spectra characterizing Pt/MgO at various temperatures, representing structural changes taking place during calcination. The sample was heated from room temperature to 700 °C at a rate of 5 °C/min as the sample was exposed to 20% O_2 in helium flowing at a rate of 20 mL(NTP)/min for 0.5 h. (b) XANES spectra characterizing Pt/MgO400 and Pt/MgO700, each in helium flowing at 20 mL(NTP)/min at room temperature. The DFT-optimized geometries of the most stable (c) surface structure: [100]/sub0/O_2 side view and top view and (d) subsurface structure [100]Mg-vac/sub1 side view and top view. EXAFS spectra characterizing (e) Pt/MgO400 and (f) Pt/MgO700 in helium flowing at 20 mL (NTP)/min at room temperature in R-space (k^3-weighted) with the corresponding EXAFS fits based on [100]/sub0/O_2 and [100]Mg-vac/sub1 structures, respectively, showing the magnitude (fit: blue; experiment: black) and imaginary portions (fit: green; experiment: black) of Fourier transforms of the data. The k-range of 2.2-12.5 $Å^{-1}$ and the R-range of 1.0-5.0 Å were used for the fits. Colors: Mg (green), O (red), and Pt (gray) (The nearest neighbors of Pt are shown in bright colors, and the other atoms are shown in faded colors.). The purple sphere represents the subsurface magnesium vacancy. Simulated (blue) and experimental (black) HERFD-XANES spectra of (g) Pt/MgO400 in helium flowing at 20 mL (NTP)/min at room temperature determined for the best-fit EXAFS data from the DFT-optimized structure [100]/sub0/O_2 and (h) Pt/MgO700 in helium flowing at 20 mL (NTP)/min at room temperature determined for the best-fit DFT structure [100]Mg-vac/sub1.

To repeat for emphasis: a comparison of the results determined for the samples calcined at 400 and at 700 °C shows that during the calcination as the temperature was raised to 700 °C, in the interval from 400 to 700 °C, the atomically dispersed platinum was converted from surface to sub-surface species.

The platinum in the subsurface sites is clearly characterized by stronger metal–support interactions than the former, as it has fewer coordinatively unsaturated sites for bonding of adsorbates than the platinum in the first layer. The results of locally projected density of states calculations shown in Figure 3.S6 bolster the conclusion.

The expectation that the different surroundings of the platinum in Pt/MgO400 and Pt/MgO700 are characterized by markedly different reactivities was confirmed by IR spectroscopy of samples exposed to CO. CO was adsorbed on Pt/MgO400

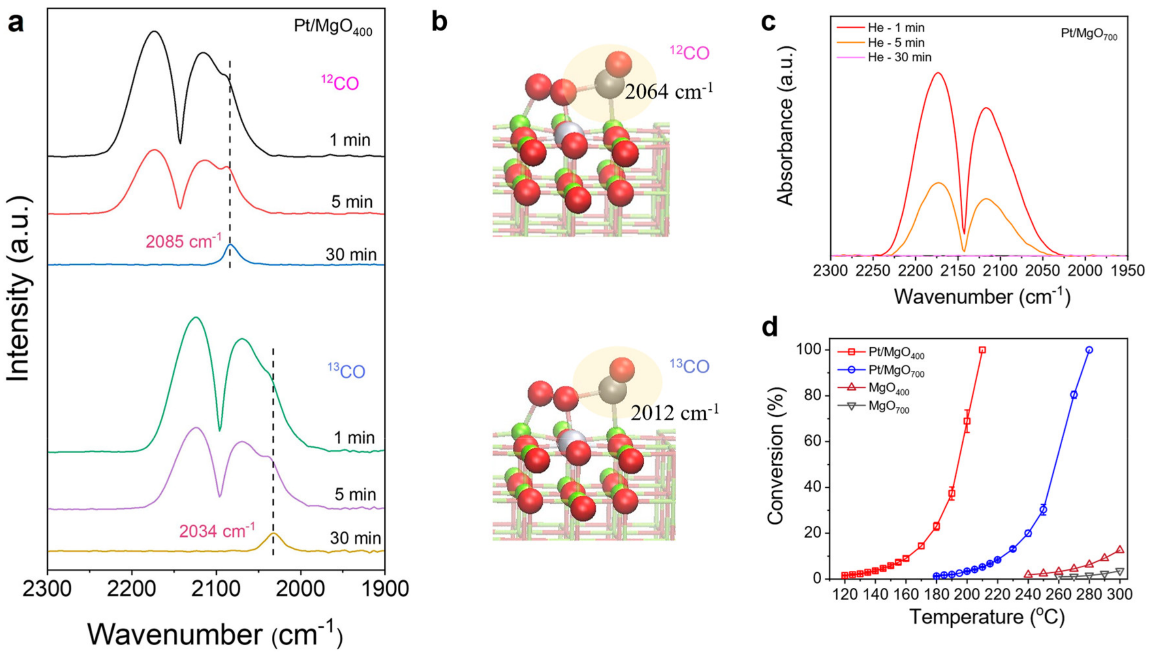

Figure 3.3. (a) IR spectra in the νCO region characterizing Pt/MgO400 recorded after the sample had been in contact with flowing 10% CO in helium for 30 min, followed by a purge of the IR cell with helium for 1, 5, and 30 min. After each of these treatments, IR spectra were recorded after exposure of the sample to a 2 min pulse of flowing 13CO, followed by a purge of the IR cell with the helium for 1, 5, and 30 min. (b) Calculated positions of peaks for possible CO and 13CO adsorbed on the [100]/sub0/*O2 structure. (c) IR spectra in the νCO region characterizing Pt/ MgO700 recorded after the sample had been in contact with flowing 10 CO in helium for 30 min, followed by a purge of the IR cell with helium for 1, 5, and 30 min. (d) Light-off curves characterizing CO oxidation catalyzed by Pt/MgO400 and PtMgO700. Error bars represent standard deviations determined from three independent measurements. The once-through plug-flow reactor was heated from room temperature to 300 °C at a rate of 2 °C/min. The feed was 5.0% CO in helium flowing at 4.0 mL (NTP)/min + 5.0% O2 in helium flowing at 16.0 mL (NTP)/min; the catalyst mass in each experiment was 100 mg (Data characterizing the supports MgO400 and MgO700 are shown for comparison).

at room temperature and found to be characterized by a band at 2085 cm-1, with a full width at half-maximum (fwhm) value of only 17 cm-1, which is assigned to CO on atomically dispersed Ptδ+.[29] The narrowness of the band implies that the species were nearly uniform in structure.[16] This band shifted to 2034 cm-1 when the sample at room temperature was exposed to 13CO, as this ligand displaced 12CO; the frequencies are consistent with the harmonic approximation and confirm the identification of terminally bonded CO on the platinum (Figure 3.2a and Table S2).[30] These results are confirmed by the DFT-predicted 12CO and 13CO frequencies (Figure 3.3b and Table 3.S2).[25,31]

In sharp contrast to these results, the subsurface platinum barely adsorbed CO at room temperature (Figure 3.S7).[3] Thus, the IR data are in good agreement with the XAS data showing that the highly coordinated Pt4+ species in the second layer of MgO ([100]Mg-vac/sub1) were less accessible to reactants than those in the first layer ([100]/sub0/*O_2).

These two samples incorporating differently coordinated platinum were compared as catalysts for CO oxidation in a conventional once-through plug-flow reactor operated at atmospheric pressure; the CO/O2 molar ratio in the feed was 1:4 (Figure 3.3c). As the temperature of Pt/MgO400 in the reactor was ramped from room temperature at a rate of 2 °C/min, CO oxidation activity was first observed at about 120 °C (and the CO conversion approached 100% at 210 °C). When the catalyst was Pt/MgO700, a much higher temperature was required for the onset of catalysis, 180 °C (Figure 3.3c).[3]

After use in three comparable independent catalysis experiments, the Pt/MgO400 sample was exposed to CO and characterized by IR spectroscopy (Figure 3.S9). The band at 2085 cm^{-1}, which is characteristic of CO on atomically dispersed platinum,[29] was still evident, but it was now accompanied by a broad absorption centered at 2056 cm^{-1}, which is assigned to CO adsorbed on metallic platinum (Figure 3.S9). The assignment of these bands as carbonyl bands was confirmed by the band shifts when each sample at room temperature was exposed to 13CO, which was observed to replace 12CO ligands on the platinum (Figure 3.S9).

STEM images of the Pt/MgO400 after use as a catalyst and EXAFS spectra recorded during catalysis confirm that the platinum sintered (Figure 3.S10 and Figure 3.S11), evidently having been reduced by CO and having migrated on the support surface, forming metallic platinum species. These results are consistent with prior observations of cluster formation from atomically dispersed supported platinum catalysts during CO oxidation,[32] implying that the atomically dispersed platinum in Pt/MgO400 is not stable under CO oxidation conditions and that metallic platinum was the active catalyst.

In contrast to these results, the IR data characterizing platinum in the subsurface sites remained unchanged after catalysis (Figure 3.S7). These less accessible platinum atoms were much less active catalytically than those in the first MgO layer—but also much more resistant to sintering than the platinum in the first MgO layer, as shown by reported XAS, IR, and STEM data characterizing the used subsurface platinum catalyst.[3]

Tradeoffs between high catalytic activity and structural stability are common in catalysis, often explained by roles of ligands stabilizing a metal center but limiting access of reactants to that center. Thus, coordinative unsaturation at metal centers is needed to allow bonding of reactants. The results reported here show that the platinum in the second layer of MgO is markedly less reactive with CO than the platinum in the first layer and correspondingly less active as a catalyst for CO oxidation. However, the platinum in the subsurface sites is much more stable—resistant to sintering—than the platinum in the first layer. The data point to a tradeoff between activity and stability of these catalysts and lead one to reflect on a rough analogy to homogeneous organometallic catalysis, illustrated by olefin hydroformylation with rhodium complexes, whereby increased encumbrance (ligation) of a rhodium center leads to lower activity but a higher selectivity for aldehyde formation.[33]

The observation of atomically dispersed platinum atoms not only in the first MgO layer but also in the second layer calls to mind reports of atomically dispersed supported metals in which the metals have been regarded as support-embedded.[34–36] The literature includes many examples of doped solid catalysts, with dopants in various and difficult to determine subsurface sites.[37,38] The term embedded commonly implies substitution of an additive or doped metal into sites such as cation vacancies of supports typified by metal oxides.[34] But this term is vague because the substitution can occur both at the surface and within the bulk of the support.[39]

Some prior catalysis investigations acknowledge that subsurface platinum could contribute to reactivity, but the authors did not explicitly consider these sites in models (e.g., ref[40–42]). Kraushofer et al.[43] reported rhodium clusters stabilized in the subsurface of single-crystal Fe_2O_3. They characterized both atomically dispersed rhodium on the surface and subsurface species formed from it by using XPS and He+ low-energy ion scattering complemented with DFT calculations. Our results are contrasted with those of Kraushofer et al.,[43] because we report a comparison of first-layer and second-layer metal catalysts that are both atomically dispersed—and characterized by evidence of their structures under working catalytic conditions.

We posit that atomically dispersed platinum on MgO powder may be regarded as a prototypical catalyst for investigating the interconversions of noble metal structures with various metal–support interactions. We envision other noble metal–support combinations that illustrate new properties including tradeoffs between catalyst stability, activity, and selectivity and perhaps structures that retain stability while providing better activity and selectivity.

3.4 References

[1] J. Liu. Catalysis by supported single metal atoms. *ACS Catal.*, 7:34, 2017.

[2] J. Hulva, M. Meier, R. Bliem, Z. Jakub, F. Kraushofer, M. Schmid, U. Diebold, C. Franchini, and G. S. Parkinson. Unraveling co adsorption on model single-atom catalysts. *Science*, 371:375, 2021.

[3] Y. Chen, R. Rana, T. Sours, F. D. Vila, S. Cao, T. Blum, J. Hong, A. S. Hoffman, C.-Y. Fang, Z. Huang, C. Shang, C. Wang, J. Zeng, M. Chi, C. X. Kronawitter, S. R. Bare, B. C. Gates, and A. R. Kulkarni. A theory-guided x-ray absorption spectroscopy approach for identifying active sites in atomically dispersed transition-metal catalysts. *J. Am. Chem. Soc.*, 143:20144, 2021.

[4] B. C. Gates. Atomically dispersed supported metal catalysts: Seeing is believing. *Trends Chem.*, 1:99, 2019.

[5] Y. Chen, H. S. Sun, and B. C. Gates. Prototype atomically dispersed supported metal catalysts: Iridium and platinum. *Small*, 17:2004665, 2021.

[6] L. DeRita, J. Resasco, S. Dai, A. Boubnov, H. V. Thang, A. S. Hoffman, I. Ro, G. W. Graham, S. R. Bare, G. Pacchioni, X. Pan, and P. Christopher. Structural evolution of atomically dispersed pt catalysts dictates reactivity. *Nat. Mater.*, 18:746, 2019.

[7] A. S. Hoffman, L. M. Debefve, S. J. Zhang, J. E. Perez-Aguilar, E. T. Conley, K. R. Justl, I. Arslan, D. A. Dixon, and B. C. Gates. Beating heterogeneity of single-site catalysts: Mgo-supported iridium complexes. *ACS Catal.*, 8:3489, 2018.

[8] L. Liu, D. Zakharov, R. Arenal, P. Concepción, E. A. Stach, and A. Corma. Evolution and stabilization of subnanometric metal species in confined space by in situ tem. *Nat. Commun.*, 9:574, 2018.

[9] S. Duan, R. Wang, and J. Liu. Stability investigation of a high number density pt1/fe2o3 single-atom catalyst under different gas environments by haadf-stem. *Nanotechnology*, 29:204002, 2018.

[10] L. Liu, D. M. Meira, R. Arenal, P. Concepción, A. V. Puga, and A. Corma. Determination of the evolution of heterogeneous single metal atoms and nanoclusters under reaction conditions: Which are the working catalytic sites? *ACS Catal.*, 9:10626, 2019.

[11] M. Moliner, J. E. Gabay, C. E. Kliewer, R. T. Carr, J. Guzman, G. L. Casty, P. Serna, and A. Corma. Reversible transformation of platinum nanoparticles into single atoms inside high-silica chabazite zeolite. *J. Am. Chem. Soc.*, 138: 15743, 2016.

[12] L. Liu and A. Corma. Metal catalysts for heterogeneous catalysis: From single atoms to nanoclusters and nanoparticles. *Chem. Rev.*, 118:4981, 2018.

[13] A. Uzun and B. C. Gates. Real-time characterization of formation and breakup of iridium clusters in highly dealuminated zeolite y. *Angew. Chem., Int. Ed.*, 47:9245, 2008.

[14] B. B. Sarma, P. N. Plessow, G. Agostini, P. Concepción, N. Pfänder, L. Kang, F. R. Wang, F. Studt, and G. Prieto. Metal-specific reactivity in single-atom catalysts: Co oxidation on 4d and 5d transition metals atomically dispersed on mgo. *J. Am. Chem. Soc.*, 142:14890, 2020.

[15] B. B. Sarma, G. Agostini, M. G. Farpón, C. Marini, N. Pfänder, and G. Prieto. Bottom-up assembly of bimetallic nanocluster catalysts from oxide-supported single-atom precursors. *J. Mater. Chem. A*, 9:8401, 2021.

[16] A. S. Hoffman, C.-Y. Fang, and B. C. Gates. Homogeneity of surface sites in supported single-site metal catalysts: Assessment with band widths of metal carbonyl infrared spectra. *J. Phys. Chem. Lett.*, 7:3854, 2016.

[17] F. Khairallah, A. Glisenti, M. M. Natile, and A. Galenda. Cuo/mgo nanocomposites by wet impregnation: An xps study. *Surf. Sci. Spectra*, 19:23, 2012.

[18] Y. R. Denny, T. Firmansyah, V. Gustiono, and S. S. Lee. Effect of substrate temperature on the electronic properties of mgo thin films on si (100) grown by electron beam evaporation. *Key Eng. Mater.*, 841:243, 2020.

[19] Y. Hao, B. Liu, L. Tian, F. Li, J. Ren, S. Liu, Y. Liu, J. Zhao, and X. Wang. Synthesis of 111 facet-exposed mgo with surface oxygen vacancies for reactive oxygen species generation in the dark. *ACS. Appl. Mater. Inter.*, 9:12687, 2017.

[20] L. M. Debefve, A. S. Hoffman, A. J. Yeh, R. C. Runnebaum, S. Shulda, R. M. Richards, I. Arslan, and B. C. Gates. Iridium atoms bonded to crystalline powder mgo: Characterization by imaging and spectroscopy. *J. Phys. Chem. C*, 124:459, 2020.

[21] M. Newville. Larch: An analysis package for xafs and related spectroscopies. *J. Phys.: Conf. Ser.*, 430:012007, 2013.

[22] G. Kresse and J. Hafner. Ab initio molecular dynamics for liquid metals. *Phys. Rev. B: Condens. Matter Mater. Phys.*, 47:558, 1993.

[23] A. H. Larsen, J. J. Mortensen, J. Blomqvist, I. E. Castelli, R. Christensen, M. Dulak, J. Friis, M. N. Groves, B. Hammer, C. Hargus, E. D. Hermes, P. C. Jennings, P. B. Jensen, J. Kermode, J. R. Kitchin, E. L. Kolsbjerg, J. Kubal, K. Kaasbjerg, S. Lysgaard, J. B. Maronsson, T. Maxson, T. Olsen, L. Pastewka, A. Peterson, C. Rostgaard, J. Schiotz, O. Schutt, M. Strange, K. S. Thygesen, T. Vegge, L. Vilhelmsen, M. Walter, Z. Zeng, and K. W. Jacobsen. The atomic simulation environment–a python library for working with atoms. *J. Phys.: Condens. Matter*, 29:273002, 2017.

[24] J. Lym, G. R. Wittreich, and D. G. Vlachos. A python multiscale thermochemistry toolbox (pmutt) for thermochemical and kinetic parameter estimation. *Comput. Phys. Commun.*, 247:106864, 2020.

[25] Y. Lu, J. Wang, L. Yu, L. Kovarik, X. Zhang, A. S. Hoffman, A. Gallo, S. R. Bare, D. Sokaras, T. Kroll, V. Dagle, H. Xin, and A. M. Karim. Identification of the active complex for co oxidation over single-atom ir-on-mgal2o4 catalysts. *Nat. Catal.*, 2:149, 2019.

[26] A. S. Hoffman, D. Sokaras, S. J. Zhang, L. M. Debefve, C.-Y. Fang, A. Gallo, T. Kroll, D. A. Dixon, S. R. Bare, and B. C. Gates. High-energy-resolution x-ray absorption spectroscopy for identification of reactive surface species on supported single-site iridium catalysts. *Chem.- Eur. J.*, 23:14760, 2017.

[27] J. J. Rehr, J. J. Kas, M. P. Prange, A. P. Sorini, Y. Takimoto, and F. Vila. Ab initio theory and calculations of x-ray spectra. *C. R. Phys.*, 10:548, 2009.

[28] J. J. Rehr, J. J. Kas, F. D. Vila, M. P. Prange, and K. Jorissen. Parameter-free calculations of x-ray spectra with feff9. *Phys. Chem. Chem. Phys.*, 12:5503, 2010.

[29] B. Qiao, A. Wang, X. Yang, L. F. Allard, Z. Jiang, Y. Cui, J. Liu, J. Li, and T. Zhang. Single-atom catalysis of co oxidation using pt1/feox. *Nat. Chem.*, 3: 634, 2011.

[30] K. Ding, A. Gulec, A. M. Johnson, N. M. Schweitzer, G. D. Stucky, L. D. Marks, and P. C. Stair. Identification of active sites in co oxidation and water-gas shift over supported pt catalysts. *Science*, 350:189, 2015.

[31] F. Maurer, J. Jelic, J. Wang, A. Gänzler, P. Dolcet, C. Wöll, Y. Wang, F. Studt, M. Casapu, and J.-D. Grunwaldt. Tracking the formation, fate and consequence for catalytic activity of pt single sites on ceo2. *Nat. Catal.*, 3:824, 2020.

[32] C. Dessal, T. Len, F. Morfin, J.-L. Rousset, M. Aouine, P. Afanasiev, and L. Piccolo. Dynamics of single pt atoms on alumina during co oxidation monitored by operando x-ray and infrared spectroscopies. *ACS Catal.*, 9:5752, 2019.

[33] S. Abbet, U. Heiz, H. Hakkinen, and U. Landman. Co oxidation on a single pd atom supported on magnesia. *Phys. Rev. Lett.*, 86:5950, 2001.

[34] J. Amsler, B. B. Sarma, G. Agostini, G. Prieto, P. N. Plessow, and F. Studt. Prospects of heterogeneous hydroformylation with supported single atom catalysts. *J. Am. Chem. Soc.*, 142:5087, 2020.

[35] W. Gil and A. M. Trzeciak. N-heterocyclic carbene–rhodium complexes as catalysts for hydroformylation and related reactions. *Coord. Chem. Rev.*, 255:473, 2011.

[36] X. Guo, G. Fang, G. Li, H. Ma, H. Fan, L. Yu, C. Ma, X. Wu, D. Deng, M. Wei, D. Tan, R. Si, S. Zhang, J. Li, L. Sun, Z. Tang, X. Pan, and X. Bao. Di-

rect, nonoxidative conversion of methane to ethylene, aromatics, and hydrogen. *Science*, 344:616, 2014.

[37] Y. Yao, S. Hu, W. Chen, Z.-Q. Huang, W. Wei, T. Yao, R. Liu, K. Zang, X. Wang, G. Wu, W. Yuan, T. Yuan, B. Zhu, W. Liu, Z. Li, D. He, Z. Xue, Y. Wang, X. Zheng, J. Dong, C.-R. Chang, Y. Chen, X. Hong, J. Luo, S. Wei, W.-X. Li, P. Strasser, Y. Wu, and Y. Li. Engineering the electronic structure of single atom ru sites via compressive strain boosts acidic water oxidation electrocatalysis. *Nat. Catal.*, 2:304, 2019.

[38] P. Aich, H. Wei, B. Basan, A. J. Kropf, N. M. Schweitzer, C. L. Marshall, J. T. Miller, and R. Meyer. Single-atom alloy pd-ag catalyst for selective hydrogenation of acrolein. *J. Phys. Chem. C*, 119:18140, 2015.

[39] L. Thum, W. Riedel, N. Milojevic, C. Guan, A. Trunschke, K.-P. Dinse, T. Risse, R. Schomäcker, and R. Schlögl. Transition-metal-doping of cao as catalyst for the ocm reaction, a reality check. *Front. Chem.*, 10:768426, 2022.

[40] N. Nilius and H.-J. Freund. Activating nonreducible oxides via doping. *Acc. Chem. Res.*, 48:1532, 2015.

[41] H. Sudrajat, M. M. Fadlallah, S. Tao, M. Kitta, N. Ichikuni, and H. Onishi. Dopant site in indium-doped srtio3 photocatalysts. *Phys. Chem. Chem. Phys.*, 22:19178, 2020.

[42] W. Tang, Z. Hu, M. Wang, G. D. Stucky, H. Metiu, and E. W. McFarland. Methane complete and partial oxidation catalyzed by pt-doped ceo2. *J. Catal.*, 273:125, 2010.

[43] F. Kraushofer, N. Resch, M. Eder, A. Rafsanjani-Abbasi, S. Tobisch, Z. Jakub, G. Franceschi, M. Riva, M. Meier, M. Schmid, U. Diebold, and G. S. Parkinson. Surface reduction state determines stabilization and incorporation of rh on α-fe2o3($1\overline{1}\overline{0}\overline{2}$). *Adv. Mater. Interfaces*, 8:2001908, 2021.

3.5 Supporting Information

Synthesis of Pt/MgO400. MgO powder (1000 mg, US Research Nanomaterials) was dispersed in 250 mL of ethanol in a 500-mL beaker with magnetic stirring. Aqueous K2PtCl4, 29 mL of 0.25 mM solution, and 31 mL of ethanol were transferred into the stirred beaker through a syringe pump at a rate of 5 mL/h.1 The resultant solid was collected by centrifugation, washed with distilled water, and then dried overnight in air in an oven at 80 °C. The resultant powder was calcined in flowing O2 (10 mL(NTP)/min) and N2 (40 mL(NTP)/min) as the temperature was ramped from room temperature to 120 °C and held for 2 h to remove any residual water and organics. The sample was then further calcined in a mixture of flowing O2 (10 mL(NTP)/min) and N2 (40 mL(NTP)/min) as the temperature was ramped at a rate of 5 °C/min until a final temperature of 400 °C was reached, which was held for 4 h.1 Synthesis of Pt/MgO700. The Pt/MgO400 samples was calcined in a mixture of flowing O2 (10 mL(NTP)/min) and N2 (40 mL(NTP)/min) as the temperature was ramped at a rate of 5 °C/min from room temperature to a final temperature of 700 °C, which was then held for 0.5 h.1

X-ray absorption spectroscopy. XAS measurements were made at the Stanford Synchrotron Radiation Lightsource (SSRL). Conventional XAS data were collected at beamline 4-1, which is a side station on a 20-pole wiggler beamline. SPEAR3 is operated in top-off mode with a storage ring energy of 3 GeV and 500 mA stored current. A Si double-crystal (220) monochromator was detuned by 20–25% of maximum intensity to minimize harmonics at the platinum L_{III} edge. XAS data were collected in fluorescence yield mode with a 30-element germanium solid-state detector array. For in-operando calcination treatment XAS measurements, approximately 50 mg of catalyst sample was loaded into a flow-through cell, a quartz tube (o.d. =

2.4 mm), connected to a line for the treatment gas. After collection of EXAFS data characterization of the Pt/MgO400 sample in helium flowing at 20 mL(NTP)/min at room temperature, the sample in a mixture of O_2 flowing at 2.0 mL(NTP)/min + helium flowing at 18.0 mL(NTP)/min was subjected to a temperature ramp from room temperature to 700 °C at a rate of 5 °C/min. Then the cell was held at 700 °C for 0.5 h with the gas flow continuing. Conventional in-operando XANES spectra were collected periodically during each of these steps. Then the reactor was cooled to room temperature, and the gas feed was switched to helium flowing at 20 mL(NTP)/min, and EXAFS spectra were collected For energy calibration, a platinum foil was placed between the transmission and reference channel ion chambers so that its spectrum was measured simultaneously with that of the sample. To characterize samples during CO oxidation catalysis, approximately 50 mg of catalyst was loaded into a flow-through cell, a Kapton tube (i.d. = 2.8 mm) through which the reactant gas stream flowed.2 After collection of data with the sample in helium flowing at 20 mL(NTP)/min at room temperature, the Pt/MgO400 sample was heated in a mixture of CO flowing at 0.2 mL(NTP)/min + O2 flowing at 0.8 mL(NTP)/min + helium flowing at 19 mL(NTP)/min as the temperature was ramped from room temperature to 150 °C at a rate of 5 °C/min. Then the cell was held at 150 °C for 2 h as CO oxidation catalysis was taking place; EXAFS spectra were collected at 150 °C with the catalyst in a mixture of CO flowing at 0.2 mL(NTP)/min + O2 flowing at 0.8 mL(NTP)/min + helium flowing at 19 mL(NTP)/min. Then the reactor was cooled to room temperature, and the gas feed was switched to helium flowing at 20 mL(NTP)/min. Thereafter, EXAFS spectra were collected at room temperature with the sample in helium flowing at 20 mL(NTP)/min. At beamline 6-2, equipped with a 56-pole, 0.9 Tesla wiggler, HERFD XANES experiments were conducted with a liquid-nitrogen-cooled double-crystal Si (311) monochromator to select the energy of the incident beam. A Rowland circle spectrometer (radius 1 m) equipped with three spherically bent Si (800) analyzers and a silicon drift detector were used to select the platinum-Lα emission line. A platinum foil was scanned in the transmission mode for initial energy calibration. In HERFD-XANES experiments, approximately 50 mg of catalyst sample was loaded into a flow-through cell, a quartz tube (i.d. = 2.4 mm), connected to a line for the treatment gas.2 The Pt/MgO400 sample was first heated in a mixture of O2 flowing at 2.0 mL(NTP)/min + N2 flowing at 18.0 mL(NTP)/min as the temperature was ramped from room temperature to 700 °C at a rate of 5 °C/min. Then the cell was held at 700 °C for 0.5 h with the gas feed continuing. Thereafter, the reactor was cooled to room temperature, and the gas feed was switched to helium flowing at 20 mL(NTP)/min. HERFD-XANES spectra were collected before and after the calcination treatment at room temperature with in helium flowing at 20 mL(NTP)/min.

IR Spectroscopy. Transmission IR spectra of the powder samples in the νO-H region were determined with a Bruker IFS 66v/S spectrometer with a resolution of 2 cm-1. Approximately 10 mg of sample was loaded between two KBr windows, and spectra were recorded at room temperature with the sample under vacuum, with an average of 128 scans per spectrum. IR spectra of samples with adsorbed CO were determined after approximately 40 mg of sample had been pressed into a wafer and loaded into a cell (In-situ Research Instruments, South Bend, IN). The resolution was 4 cm$\hat{}$1, and an average of 256 scans were recorded per spectrum. The cell served as a flow reactor fed with various gases (CO, 13CO, helium), and transmission spectra of catalysts in the presence of these gases were recorded with a liquid-nitrogen-cooled HgCdTe (MCT) detector.1

CO oxidation catalysis in a plug-flow reactor. The catalyst samples were evaluated for CO oxidation in a once-through plug-flow reactor, with products analyzed with an online mass spectrometer (Hiden Analytical HPR20) equipped with a secondary electron multiplier detector used in multiple ion detection mode. Samples of catalyst powder (100 mg) that had passed through a 40 to 60 mesh sieve were loaded into a quartz tube reactor (i.d. = 4 mm), with the upstream and downstream sections packed with quartz wool. In experiments to determine light-off curves for CO oxidation, the feed was a mixture of 5.0% CO in helium flowing at 4.0 mL(NTP)/min + 5.0% O2 in helium flowing at 16.0 mL(NTP)/min; the pressure was atmospheric. The reactor was heated from room temperature at a rate of 2 °C/min with the gases flowing and then held at 300 °C for 20 min before the reactor was cooled down. In experiments determining the dependence of conversion on time on stream, the samples were kept on stream for up to 48 h to demonstrate stability in operation at 150 °C, with the feed consisting of 5.0% CO in helium flowing at a rate of 4.0 mL(NTP)/min and 5.0% O2 in helium flowing at a rate of 16.0 mL(NTP)/min.1

TEM imaging. Transmission electron microscopy (TEM) images of as-prepared sample powders loaded onto copper grids were recorded with a Hitachi H-7700 transmission electron microscope at an acceleration voltage of 100 kV. STEM imaging experiments were done with a JEOL 200CF (NEOARM) transmission electron microscope with an acceleration voltage of 200 kV. Samples were prepared by a direct dispersion of powder samples onto lacey carbon grids. The HAADF images were acquired with a convergence angle of 28.5 mrad and an inner collection angle of 55 mrad.

Brunauer-Emmett-Teller (BET) surface area measurements. N2 adsorption isotherms were collected on a Micromeritics Tristar II 3020 instrument with each sample held at -196 °C with a liquid-nitrogen bath. Consistency criteria were adapted to choose an appropriate pressure range for BET surface area calculations. Samples under high vacuum were held at 250 °C for 6 h prior to the recording of the isotherms.

XPS measurements. The XPS measurements were performed with a K-Alpha Plus XPS/UPS analyzer from Thermo Fisher Scientific equipped with a monochromatic Al Kα X-ray source (1486.6 eV) in an ultrahigh vacuum chamber. A flood gun was used during the measurements to minimize sample charging. Samples were mounted onto conductive Ag tape for XPS measurement. The system reached a stable pressure, typically around the mid 10-10-torr range after ca. 12 h without sample, or 10-8-torr range with sample. Spectra of samples were calibrated by setting the adventitious carbon to 284.8 eV.

XRD Crystallography. XRD patterns of the samples were collected on a Philips X'Pert Pro Super diffractometer with a monochromatized Cu Kα radiation source and a wavelength of 0.1542 nm.

Elemental analysis by inductively coupled plasma mass spectrometry. The platinum loadings of the catalysts were determined by inductively coupled plasma mass spectrometry with a Thermo Scientific XSERIES 2 instrument.

DFT calculations. Periodic DFT calculations were performed using the projector augmented wave method as implemented in the Vienna *ab initio* simulation package (VASP).3 Energies were calculated using a 500 eV plane-wave cutoff with a 2 × 1 × 1 Monkhorst-Pack k-point grid. A range of generalized gradient approximation functionals (PBE, RPBE, and PBESol) were used. Electronic energies were converged to 10-̂6 eV, and all structures were relaxed until the forces were less than 0.05 eV/Å. The finite displacement method (0.02 Å) was used to calculate the entropic and zero-point energy corrections. For CO-IR frequency calculations, a 400 eV plane-wave cutoff was used with the PBE, RPBE, and PBESol functional, and scaling corrections were calculated (shown in Table S2).

XAS data analysis. The XANES data were analyzed with the Demeter package. Pre-processing of data included alignment, edge calibration, deglitching, normalization, background subtraction, and conversion of data into a chi file for data fitting, performed with Athena. The energy at the platinum L_{III} edge, determined by the first inflection point of the absorption edge data characterizing the reference platinum foil, was calibrated to the reported energy, 11564.0 eV. The EXAFS data were analyzed with QuantEXAFS1 based on the open-source X-ray Larch package. Data processing, including alignment, edge calibration, deglitching, normalization, and background subtraction, was performed using QuantEAXFS.

FEFF and DOS modeling. All HERFD simulations used DFT-optimized (PBE-D3) structures and were performed with FEFF 9 using SCF and FMS cutoff radii of 6 and 9 Å, respectively, which ensured convergence of the spectra.6,7 The representative atomic potentials were chosen to reproduce chemical distinguishability for each atom type. On the basis of our experience with Pt-containing samples, we chose not to use a core-hole in the calculations.8,9 To properly simulate HERFD rather than the default XANES in FEFF, we also removed 1.8 eV from the default core-hole lifetime broadening of 5.2 eV. The self-energy was modeled using the density-dependent MPSE (many-pole self-energy) dielectric function approach based on a weighted average of the atomic loss functions.10 Moreover, to provide converged results up to about 200 eV above the edge, the maximum angular momenta for the site basis set were raised to 5, 4, and 4 for Pt, O, and Mg, respectively. Further, vibrational disorder was added using single-scattering Debye-Waller factors based on a correlated Debye model. The Debye temperature for this model was estimated for each system using average force constants for the first-shell Pt–O bonds obtained from the DFT structural simulations.

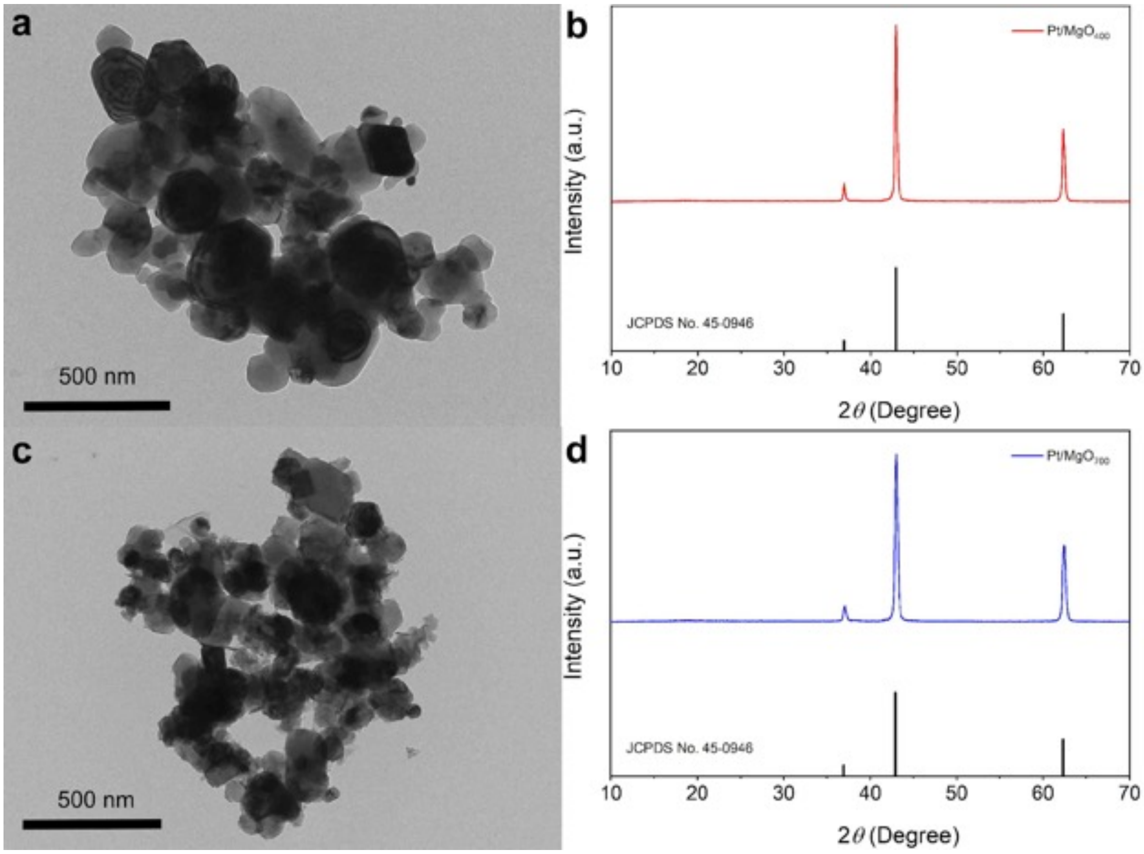

Figure 3.S1. TEM image and XRD pattern of (a, b) Pt/MgO400 sample; (c, d) Pt/MgO700 sample.

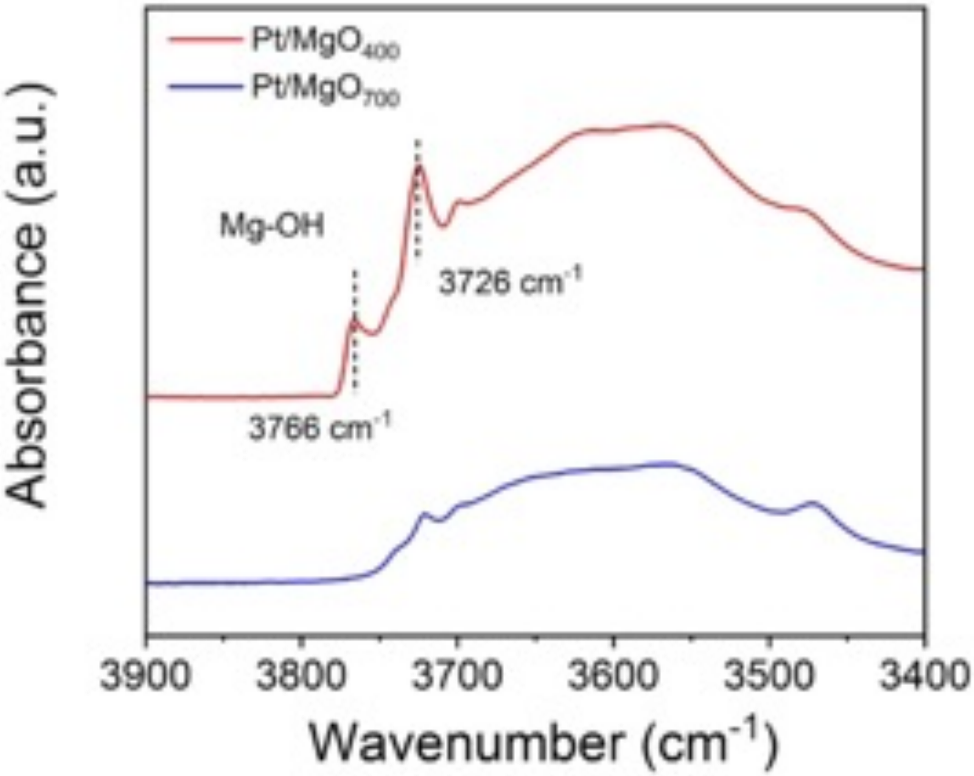

Figure 3.S2. IR spectra of ν O-H region of Pt/MgO400 and Pt/MgO700 sample.

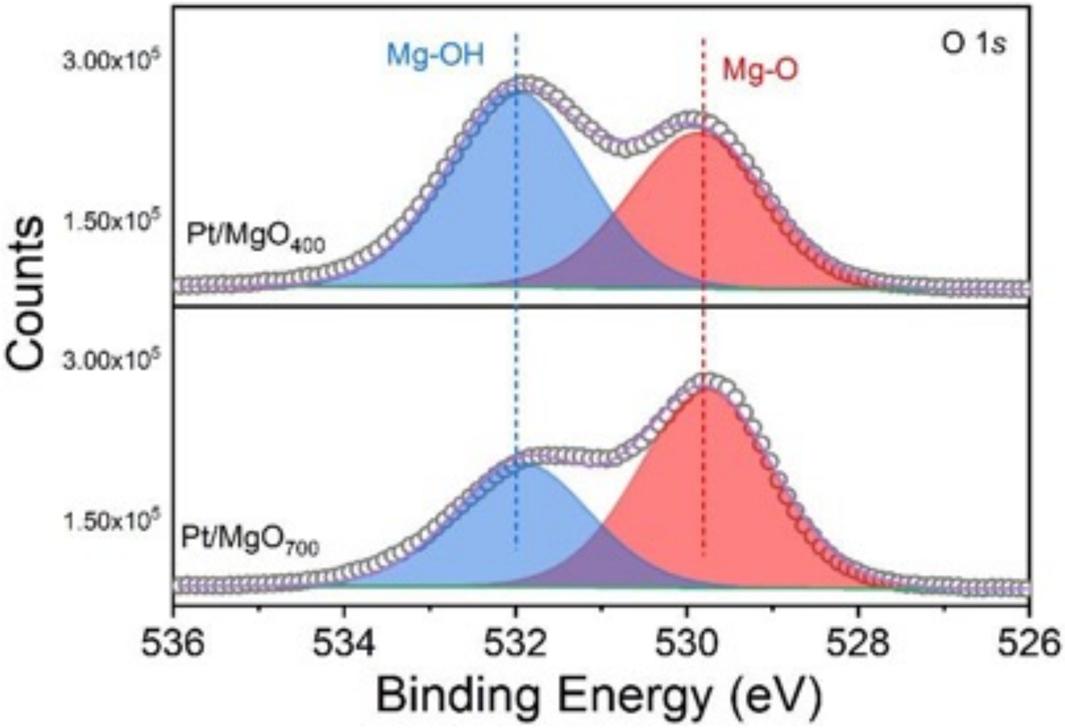

Figure 3.S3. O 1s XPS data of Pt/MgO400 and Pt/MgO700 sample.

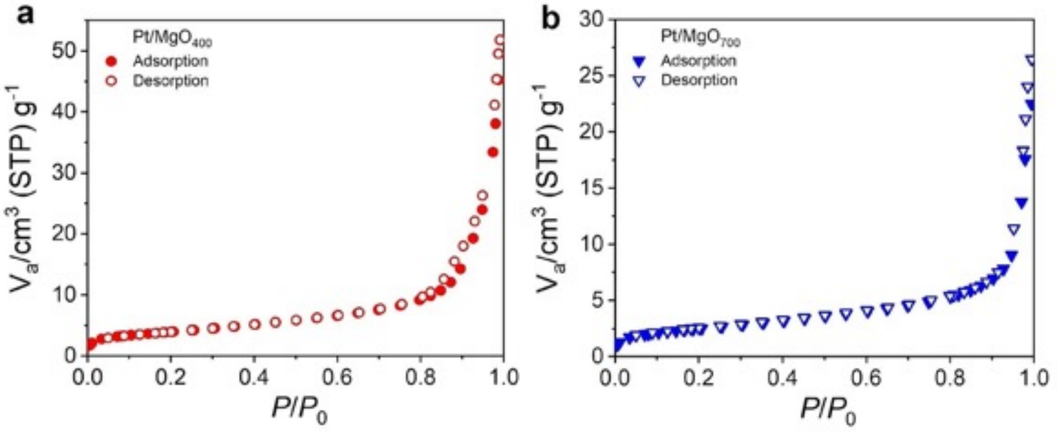

Figure 3.S4. N_2 isotherms for (a,b) Pt/MgO400 and Pt/MgO700 sample at -196°C. Adsorption showed as filled squares; desorption shown as open squares.

Table 3.S1. BET surface areas of Pt/MgO400 and Pt/MgO700.

Sample	**BET Surface area (m2̂ g-̂1)**
Pt/MgO400	14.2
Pt/MgO700	9

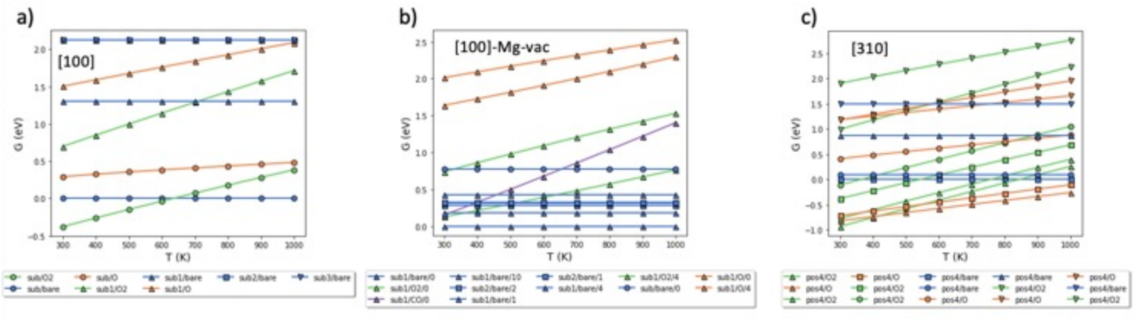

Figure 3.S5. The temperature-dependent phase diagrams are summarized in (a), (b), and (c). Notation scheme for [100] and [100]Mg-vac MgO terraces: top surface (sub0), first (sub1), second (sub2), and third (sub3) subsurface layers. For the [310] facet, we considered various step site positions including leading step edge (pos1), lower step edge (pos2), underneath step edge (pos3), and behind step edge (pos4). The phase diagrams were calculated relative to the most-stable "bare" platinum configuration (i.e., without adsorbates). All DFT-optimized structures are available as an Atomic Simulation Environment (ASE) database file in the group repository on GitHub

Theoretical HERFD vs locally projected Density of States. The figure below shows a comparison of the locally projected, l-dependent density of states (l-DOS) for the [100]Mg-vac/sub1 and [100]/sub0/*O2 systems. The l-DOS can be used to analyze the origin of the features observed in the HERFD-XANES (also shown in the figure). The spectra follow the Pt d-DOS very closely as indicated by the vertical dashed black lines that indicate the main spectral features, as expected given the selection rules for the Pt L_III edge. The white line (WL) is composed largely of this Pt d-DOS, but the l-DOS also shows contribution from the O p-DOS. Simulations show that the intensity of the WL is sensitive to the local disorder around the Pt and tends to be damped when the disorder is increased. On the other hand, the position of the WL is not greatly changed by small distortions, indicating that the intensity change is likely an indirect result of the charge density redistribution induced by different overlap with the O near-neighbors. For [100]Mg-vac/sub1, the first feature above the WL at 9 eV above the Fermi level is interesting because it has non-local contributions from both the O and Mg atoms. There is also contribution from the local Pt s-DOS, indicating that this feature arises in part from deformation of the local Pt density through bonding to the near-neighbor atoms. Local deformation analysis confirms this, showing that both the intensity and the position of this feature depends significantly on the local environment. In the case of [100]/sub0/*O2, this feature appears 9-12 eV above the Fermi level and is noticeably less intense. The lower intensity is probably related to the lower Pt d-DOS as well as less prominent non-local contributions. As expected, for high energies above the edge, the remaining features at 20, 30, 40 and 70 eV are mostly dominated by the local Pt d-DOS and are similar in both position and intensity for both structures.

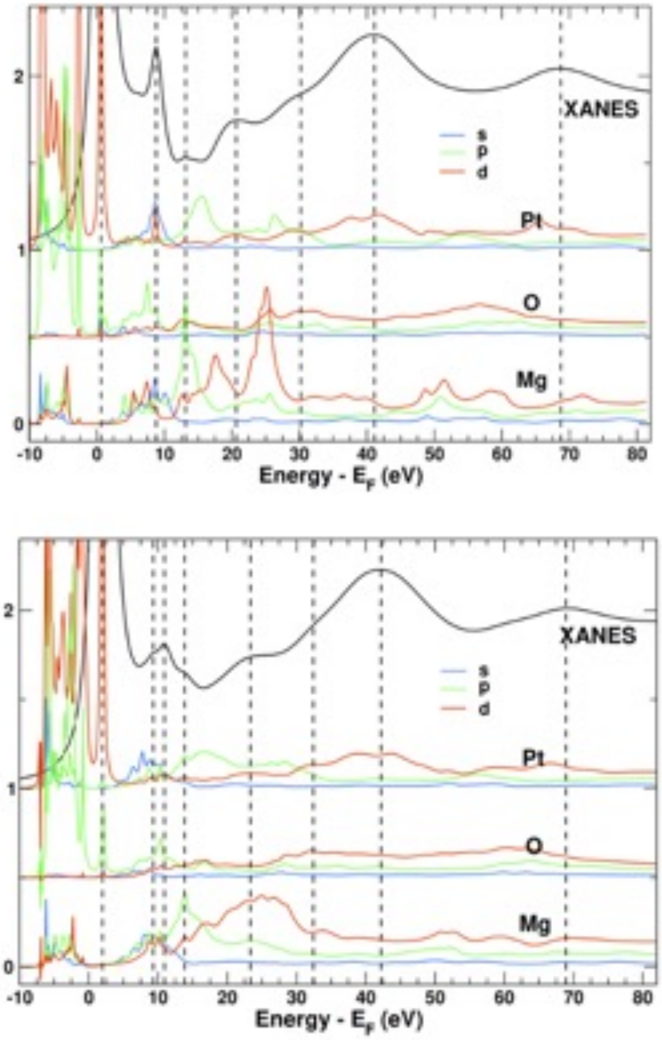

Figure 3.S6. Comparison of the theoretical HERFD-XANES (black) for the [100]Mg-vac/sub1 (top) and [100]/sub0/*O_2 (bottom) systems to the locally projected l-dependent density of states (s-blue, p-green, and d-red), relative the Fermi level (EF). The dashed vertical lines highlight the main features in the HERFD-XANES, to facilitate comparison with the l-DOS features. The l-DOS for each atom and the HERFD-XANES have been staggered vertically for clarity.

Table 3.S2. 12CO harmonic approximation calculation and scaling using various generalized gradient approximation methods confirming the presence of terminally bonded CO ligands. The error (difference between the experimental values and the scaled values) is within the acceptable range.

Method	**Frequency**[1]	**Frequency**[2]	**Frequency**[3]
Experimental	2085	-	2170
PBE	2026	2056	2140
RPBE	2010	2026	2153
PBESol	2037	2064	2142

[1] **unscaled adsorbed CO,cm-1;** [2] **scaled adsorbedCO,cm-1;** [3] **CO(g), cm-1**

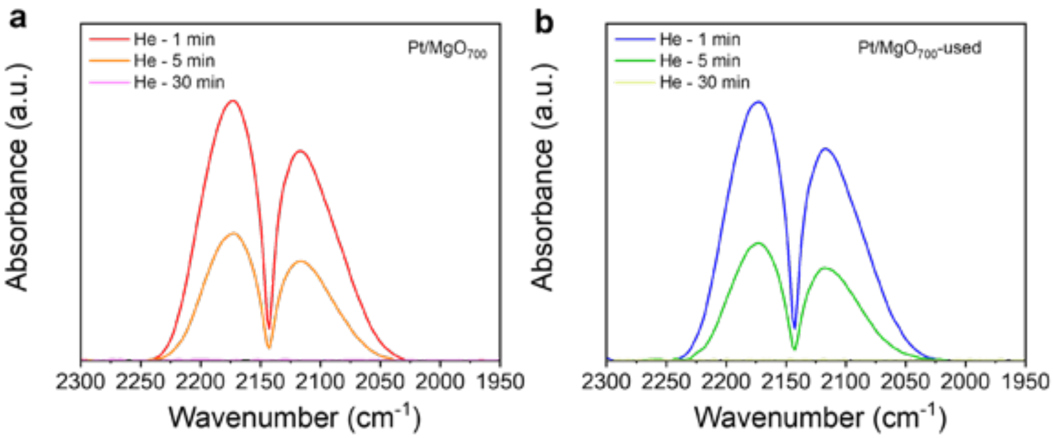

Figure 3.S7. IR spectra of (a) Pt/MgO700; and (b) Pt/MgO700-used (Pt/MgO700 after it had been used as a catalyst in three independent light-off CO oxidation measurements); in flowing helium recorded at 1, 5, and 30 min after the beginning of flow of CO at room temperature and 1 atm. The bands at 2174 and 2118 cm-1 represent the gas-phase CO.

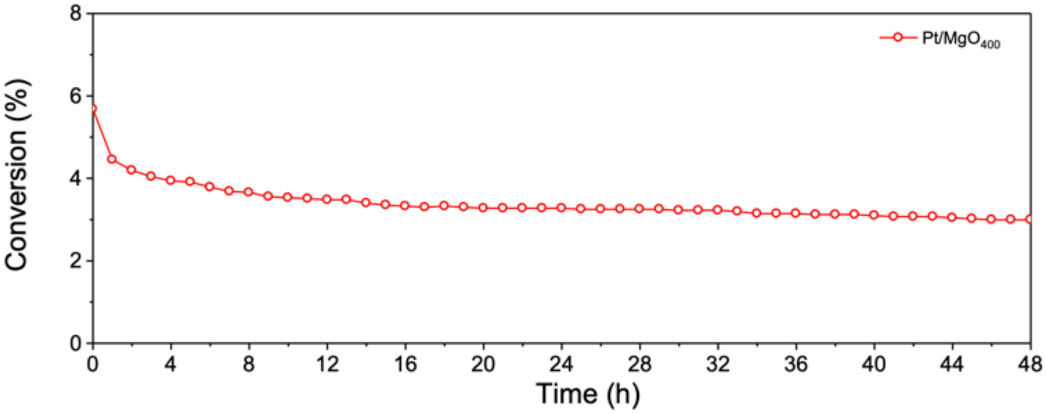

Figure 3.S8. Stability of Pt/MgO400 catalyst for CO oxidation in a once-through flow reactor operated at 150 °C and atmospheric pressure with a steady flow of reactant consisting of 5.0% CO in helium flowing at a rate of 4.0 mL(NTP)/min and 5.0% O2 in helium flowing at a rate of 16.0 mL(NTP)/min.

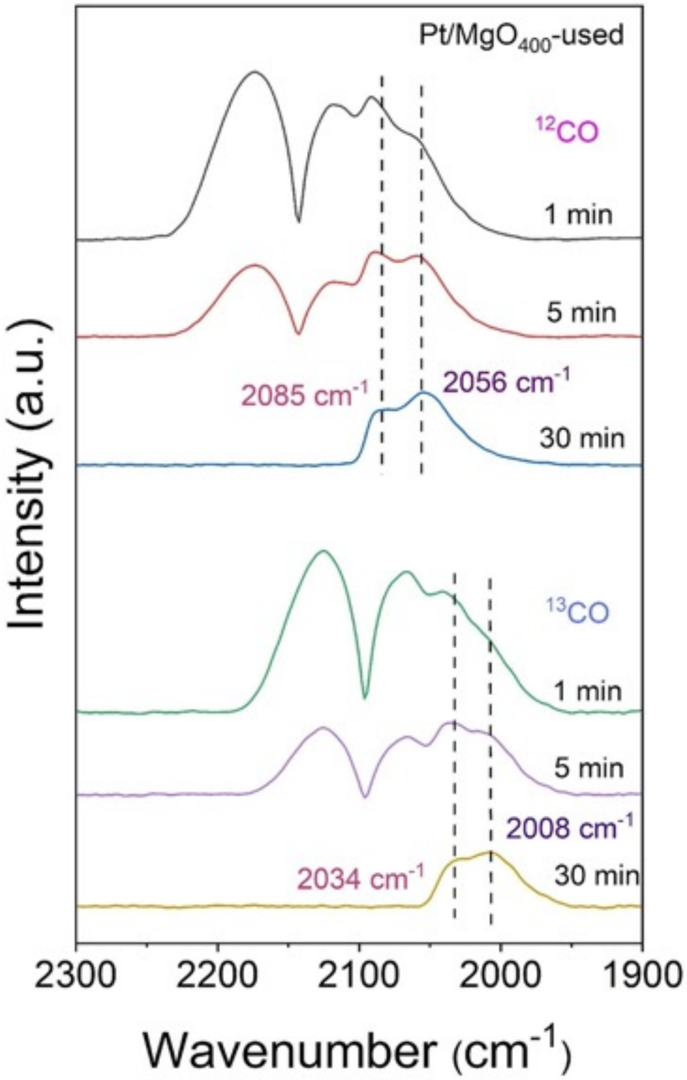

Figure 3.S9. IR spectra in the ν CO region characterizing Pt/MgO400-used (Pt/MgO400 after it had been used as a catalyst in three independent light-off CO oxidation measurements) in flowing helium recorded at 1, 5, and 30 min after the beginning of flow of CO at room temperature and 1 atm. After above experiments IR spectra of Pt/MgO400 in He recorded at 1, 5, and 30 min while the He flow continued after exposure to flowing of 13CO for 2 min at room temperature.

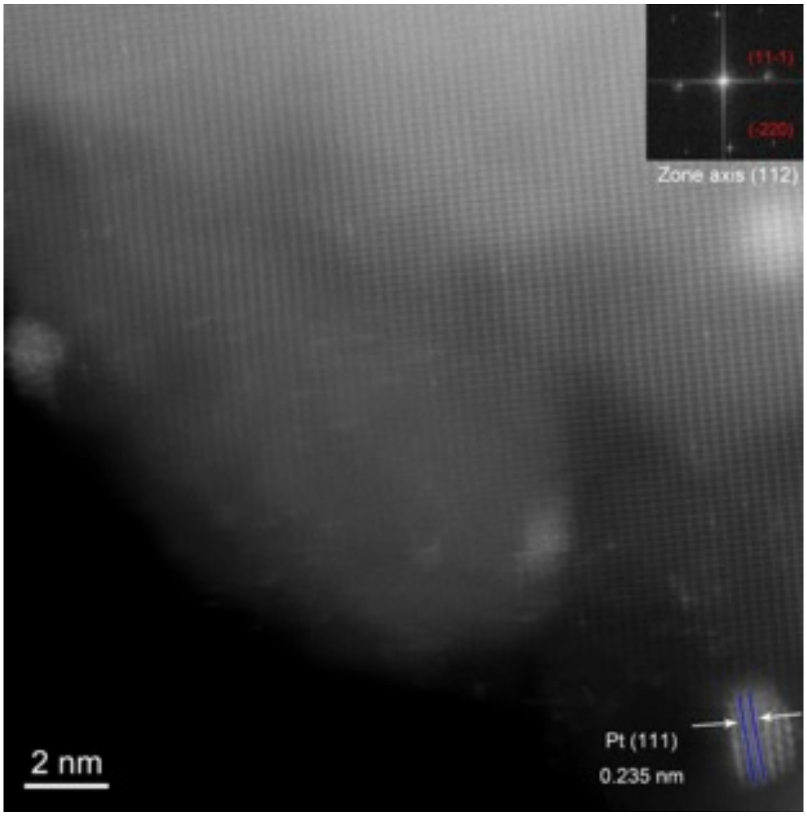

Figure 3.S10. HAADF-STEM image of Pt/MgO400-used (Pt/MgO400 after it had been used as a catalyst in three independent light-off CO oxidation measurements) sample along the (112) zone axis.

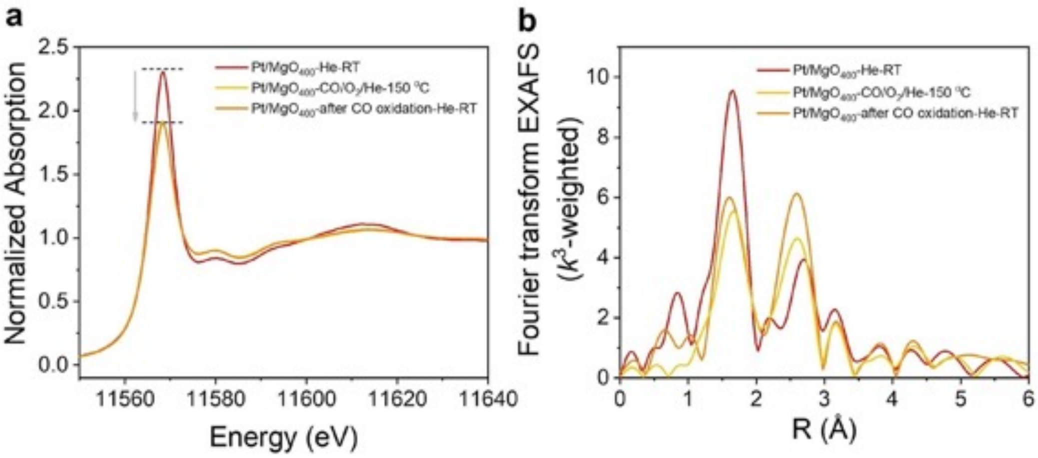

Figure 3.S11. (a) Conventional XANES spectra and (b) Fourier transform of k3-weighted EXAFS spectra characterizing PtMgO400 at various condition for CO oxidation reaction (Red line: at room temperature in helium flowing at 20 mL(NTP)/min; yellow line: at 150 oC in a mixture of CO flowing at 0.2 mL(NTP)/min + O2 flowing at 0.8 mL(NTP)/min + He flowing at 19 mL(NTP)/min; and orange line: at room temperature in helium flowing at 20 mL(NTP)/min after it had been used as a catalyst for CO oxidation at 150 °C for 2 h.

Chapter 4

Enhancing the capabilities of QuantEXAFS: Probing Site Heterogeneities in Catalytic Systems with X-ray Absorption Spectroscopy

Rachita Rana, Simon R. Bare, Ambarish Kulkarni

This chapter will be submitted in the form of a manuscript for publication.

4.1 Abstract

QuantEXAFS has been robust in identifying catalytic sites for mostly homogeneous samples. However, in case of samples with a distribution of different sites, it becomes essential to probe the fractional contribution of sites. For this purpose, we have developed Multi-site (MS) QuantEXAFS workflow that allows simultaneous fitting of DFT structures to experimental EXAFS data with mixed components in a completely automated manner. As a proof of concept, and for the purpose of benchmarking the code, known fractions of site isolated subsurface Pt/MgO (from Chapter 2) were mixed with homogeneously sized Pt nanoparticles supported on MgO. The known fractions of the physically mixed samples were compared to the results from MS-QuantEXAFS and the quantified fractions were within the range of ±5%.

4.2 Introduction

Materials consisting of isolated transition metal cations stabilized by metal oxide supports continue to be widely explored as catalysts for several chemical reactions.[1–3] These materials, which are often called atomically dispersed catalysts, could be industrially relevant as they allow increased utilization of expensive noble metals. Several examples in the literature have shown that "single atom" sites can indeed be stabilized on oxide supports.[4,5] However, important questions about the uniformity of the desired "single atom" sites as well as the potential contributions of the accompanying metallic or oxide phases remain unanswered.

Several recent studies have emphasized that different types of atomically dispersed sites can be simultaneously populated even for simple supports such as crystalline MgO; their distribution depends on synthesis conditions, the activation mechanisms, and the reaction environment.[6–9] Similar findings have been reported for other supports such as CeO_2, TiO_2 and zeolites.[3,10–14] Thus, despite the increasing number of atomically dispersed catalysts reported in the literature and the significant progress made in their characterization, unambiguously quantifying the uniformity and heterogeneity of atomically dispersed sites remains a challenging task within the community.

As a step towards overcoming this bottleneck, we now show that our recently developed analysis method (i.e., QuantEXAFS) can be used to simultaneously detect the presence of and quantify the contributions from multiple transition metal (TM) environments that may be present in a non-uniform catalyst sample. This new QuantEXAFS[6] capability, which leverages the flexibility of the xraylarch package[15], is demonstrated by preparing known physical mixtures of two different types of MgO-supported Pt catalysts. As discussed later, we show that a simultaneous multi-site fitting approach, can be used to predict the fractions of Pt-np (nanoparticles of Pt supported on MgO) and Pt-iso (subsurface isolated Pt atoms in MgO support) sites using only the DFT-optimized structure of the Pt-iso/MgO site(s) as the key input in addition to a standard Pt foil for nanoparticle.

As illustrated in Figure 4.1, five samples of "physically mixed" Pt catalysts consisting of varying amounts of Pt nanoparticles[16] (denoted as Pt-np/MgO) and isolated Pt sites (denoted as Pt-iso/MgO) were characterized using XAS. The latter materials are similar to the Pt-700/MgO catalysts reported and characterized in our previous studies , Chapter2. These mixed catalyst samples are denoted as Pt-mix-X/MgO, where X refers to the weight fraction of the Pt that exists in the nanoparticle form.

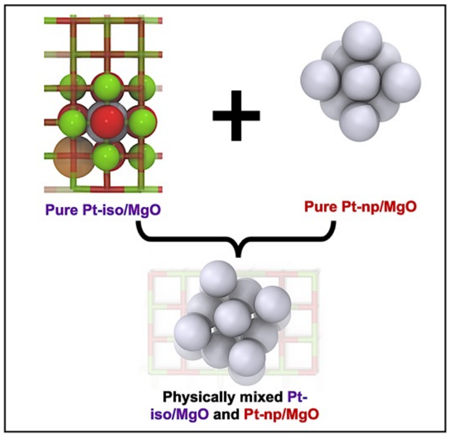

Figure 4.1. Schematic representation of platinum isolated sample and platinum nanoparticle supported on MgO. Color scheme: magnesium (green), oxygen (red), platinum (gray).

Figure 4.2 shows k^3-weighted Pt L_{III}-edge XAS data collected at the 9-3 beamline at SSRL for the two pure catalyst samples (i.e., Pt-np/MgO (red) and Pt-iso/MgO (blue)) and the XX Pt-mix/MgO catalysts. Unsurprisingly, as the weight fraction of the Pt-np increases, we observe a monotonic decrease in the intensity of the first scattering peak. This peak, as shown in the QuantEXAFS analysis of pure Pt-iso/MgO in the SI and our previous work, can be attributed to the Pt-O scattering paths. Concomitant with the decreasing intensity of the Pt-O scattering paths, we observe a gradual broadening and a shift to lower R in the position of the second peak. Based on the QuantEXAFS analysis of the pure Pt-iso/MgO material, this region arises due to the Pt-Mg scattering paths, which are gradually replaced by the increasing Pt-Pt contributions arising from the increasing weight fractions of Pt-np/MgO. Indeed, the pure Pt-np/MgO catalysts show an average coordination number of 9.2±1.3 for the first shell. The corresponding transmission electron microscopy (TEM) results show that the Pt-np/MgO material consist entirely of 2.38 ± 0.49 nm Pt nanoparticles. On the other hand, as reported previously, the Pt-iso/MgO catalyst consists of a sub-surface Pt cation that is located close to a Mg vacancy. This site is characterized by CN_Pt-O = 5 and CN_Pt-Mg = 11.

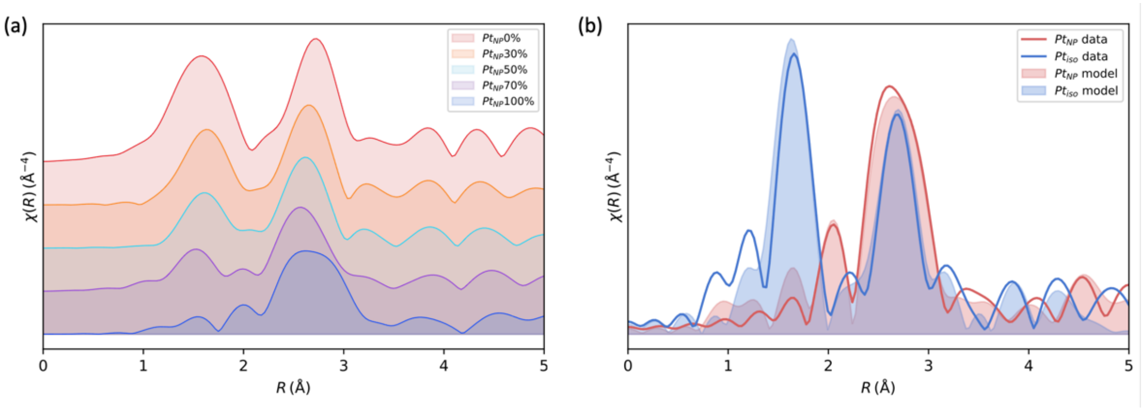

Figure 4.2. a) Experimental EXAFS data obtained for PM samples used for benchmarking the site-fractions code (the legend represents the fraction of Pt-np/MgO in each dataset), and b) EXAFS fit in R-space magnitude of the Fourier transform for Pt-np/MgO and Pt-iso/MgO data and model; the k-range used in the fits was 2.2–12 Å^{-1} and the R-range is 1.0–5.0 Å.

4.3 Results and Discussion

Implementation of MS-QuantEXAFS

Before proceeding further to the analysis of mixed samples, it is useful to emphasize the differences between the traditional EXAFS analyses and QuantEXAFS. As the experimental EXAFS spectra represents the average coordination environment around the absorbing atom, the typical EXAFS fitting approach aims to identify one or more scattering shells (i.e., average CNs at different scattering distances; including thermal disorder terms) that minimize the errors between the simulated and the experimental spectra. Here, the simulated spectra are obtained using Eq (4.1 & 4.2); details of each term in Eq (4.1 & 4.2) are presented in the tablulated summary 4.3 of symbols in EXAFS equation. As the contributions from each shell scale linearly with the corresponding CNs (used as a continuous variable), the final simulated EXAFS spectrum is a CN-weighted sum of the individual shell contributions. As discussed previously, this approach has been highly successful and is best suited for investigating materials where the absorbing atom exists in variety of coordination environments (e.g., TM nanoparticles).

Note: The variables in green are from DFT and are not changed ($CN_{i,DFT}$). As shown in the equations below, non-linear terms are observed because of CN_{iso} being a variable.

$$\chi_{\text{Pt-iso}}(k) = \sum_i \left(\frac{\text{CN}_{i,\text{DFT}} S_0^2 F_i(k) \exp(-2k^2\sigma_i^2) \exp\left(-\frac{2R_i}{\lambda}\right)}{2kR_i^2} \sin(2kR_i + \delta_i(k)) \right) \tag{4.1}$$

$$\chi_{\text{Pt-iso}}(k) = \sum_i \left[\text{CN}_{i,\text{DFT}} G(k, R_i)\right] \tag{4.2}$$

$$\chi_{\text{Pt-np}}(k) = \sum_i \left(\frac{\text{CN}_{i,\text{np}} S_0^2 F_i(k) \exp(-2k^2\sigma_i^2) \exp\left(-\frac{2R_i}{\lambda}\right)}{2kR_i^2} \sin(2kR_i + \delta_i(k)) \right) \tag{4.3}$$

$$\chi_{\text{Pt-np}}(k) = \sum_i \left[\text{CN}_{i,\text{np}}\, G(k, R_i) \right] \tag{4.4}$$

$$\chi_{\text{Pt-mix}} = x_{\text{iso}} \chi_{\text{Pt-iso}} + x_{\text{np}} \chi_{\text{Pt-np}} \tag{4.5}$$

$$\chi_{\text{Pt-mix}} = x_{\text{iso}} \left(\sum_i \left(\text{CN}_{i,\text{DFT}}\, G(k, R_i) \right) \right) + x_{\text{np}} \left(\sum_i \left(\text{CN}_{i,\text{np}}\, G(k, R_i) \right) \right) \tag{4.6}$$

$$\chi_{\text{Pt-mix}} = \left(\sum_i x_{\text{iso}}\, \text{CN}_{i,\text{DFT}}\, G(k, R_i) \right) + \left(\sum_i x_{\text{np}}\, \text{CN}_{i,\text{np}}\, G(k, R_i) \right) \tag{4.7}$$

parameter	**source**	**description**	**treatment in the fit**	
			conventional	**QuantEXAFS**
k		photoelectron wavenumber		
S_0^2	modelled	amplitude reduction factor	fixed*	fixed*
N	modelled	coordination number or path degeneracy	fit parameter	fixed
F(k)	theory	effective scattering amplitude	FEFF (paths from standard data)	FEFF (DFT-optimized structure)
δ(k)	theory	central and scattering path phase shift	FEFF (paths from standard data)	FEFF (DFT-optimized structure)
λ(k)	theory	mean free path of the photoelectron	FEFF (paths from standard data)	FEFF (DFT-optimized structure)
R	modelled	half path length	fit parameter	fixed or constrained
σ^2	modelled	mean square deviation in half path length	fit parameter	fit parameter
x	modelled	fraction of component 1 present in the sample	N/A	fit parameter

Figure 4.3. Tabulated representation of the terms in the EXAFS equation used in the conventional EXAFS analysis and in QuantEXAFS.

Complementary to the conventional analysis approach, QuantEXAFS, is best suited for studies that seek to identify single (or a few) specific sites that may be present in a potentially non-uniform sample. In contrast to the average CN approach discussed above, QuantEXAFS explicitly includes contributions from all the individual scattering paths and uses a categorization scheme to limit the number of variables being optimized. As illustrated in Eq (4.3 & 4.4), although overall spectra obtained from QuantEXAFS is also a weighted sum, here, the CNs for each scattering path are fixed and are not a changed during the optimization. As discussed below, this distinction lies at the heart of our analysis.

Specifically, we used two distinct methods to estimate the 'site-fractions' of the Pt-np and Pt-iso sites within the mixed samples. Method 1, denoted as the fixed spectrum (FS) approach, uses the pure Pt-iso/MgO and Pt-np/MgO spectra to estimate the weight fractions of each species. Here, we include two additional variables, denoted as x_{np} and x_{iso}, to scale the EXAFS contributions of Pt-np and Pt-iso sites, respectively (Eq 4.5). As the two fractions add up to unity, this approach is trivially implemented in scipy.[17] Although the FS strategy reproduces the experimental weight fractions (within ± 8%), this approach assumes that XAS measurements for the two limiting cases (i.e., 100% Pt-np and 100% Pt-iso) are available a priori (Eq. 4.6). This approach in essentially similar to the linear combination fitting of XANES as practiced conventionally. As most experimental site isolated samples could contain minor contributions from the corresponding oxides or nanoparticles (which may not be seen in microscopy images),[18–20] the practical usefulness of the FS strategy is limited. However, our results, which are consistent with previous reports in the literature,[2,21–24] serve as a proof-of-concept to show that EXAFS data can indeed be used to obtain quantitative insights.

To overcome the data availability requirements of the FS strategy, we explored an alternate approach that does not require any information about the pure Pt-iso or the Pt-np sites. Here, we modified the EXAFS analysis routines within xraylarch to include x_{np} and x_{np} (where, x_{np}= 1 - x_{iso}) within the optimization. Thus, while our previous QuantEXAFS analysis examines a set of pre-determined DFT structures (subsurface Pt adjacent to Mg vacancy in reference[6]; surface Pt bound to O_2 in reference[9]) to identify the best fit for the experimental data, here, we make two specific changes:

- We use two separate FEFF simulations to create a concatenated list of scattering paths corresponding to two Pt environments: (1) the Pt-iso sites (obtained from DFT structures) and (2) the Pt-np model (obtained using Pt foil standard from ICSD[25] database) and the structures for both Pt-iso and Pt-np were converted to feff input files using atoms2feff code from QuantEXAFS, and
- We scale the contributions from Pt-iso scattering paths with x_{iso}, and the Pt-np scattering paths with and x_{np}.

This information is summarized in Eq. 4.7 . Note that this implementation is advantageous as it allows the in-built xraylarch fitting routines and analysis tools to be used without any other changes.

A key observation from Eq. 4.7 is how the inclusion of x_{iso} and x_{np} impact of the contributions of Pt-iso and the Pt-np components. In both cases, the site-fractions terms (i.e., x_{iso} and x_{np}) decrease the contributions of the individual sites to the overall spectra (as $x_{\text{iso}} \leq 1$ and $x_{\text{np}} \leq 1$) However, while the x_{iso} term uniformly (i.e., linearly) scales the contributions of each individual path for the Pt-iso contributions, x_{np} induces addition non-linear behavior due to creation of the $x_{\text{np}}\ CN_{\text{np}}$ term. Specifically, as the CNs are used as a fitting variable in the analysis of Pt-np contributions, this approach suggests that erroneous CN_{np} values could be possible for small values of x_{np}. Practically, this means that when Pt-nps are present in small amounts, the optimization problem is not very sensitive to the value of $CN_{\rm np}$. Note that this limitation is not relevant for the Pt-iso contributions as the Pt-iso CNs are fixed during the fitting procedure.

As this procedure seeks to simultaneously optimize the EXAFS contributions from the individual paths (χ, see Table 4.S2 and 4.S3 for the fitting variables for Pt-iso and Pt-np) while also varying the fractions of the Pt-iso and Pt-np sites (i.e., $x_{\rm iso}$ and $x_{\rm np}$), we call this as the multi-site QuantEXAFS (MS-QuantEXAFS) approach. Although we only focus on mixtures of Pt-iso and Pt-np sites, we anticipate that the MS-QuantEXAFS strategy can be generalized to other combinations of atomically dispersed TM sites.

Estimating 'site-fractions' We now use the above MS-QuantEXAFS framework to study the site speciation of the 5 Pt-mix/MgO catalysts discussed earlier. Figure 4.4 a shows the experimental EXAFS spectra of the Pt-mix-50 sample (black). The results from the MS-QuantEXAFS procedure (blue) predict 47.6 ± 5% Pt-np, which are in reasonable agreement with the experimental reference value (i.e., 50%). Figure 4.4b and 4.4c also compare the values of the fitting parameters and the individual spectra as obtained from MS-QuantEXAFS with the reference values (obtained from pure Pt-iso/MgO and Pt-np/MgO.) This analysis suggests that the proposed MS-QuantEXAFS approach correctly predicts the "shape" and the contributions from the two types of Pt-environments presents in the sample. Here, the "shape" of the spectra refers to the simulated spectra obtained using the fitting values obtained from the MS-QuantEXAFS routine for the Pt-mix-50 sample and the pure Pt-iso and Pt-np catalysts (Eq. 4.7).

Sensitivity Analysis

To examine the robustness of the above approach, we perform two additional analyses. Firstly, explore the sensitivity of MS-QuantEXAFS to the Pt-iso structure

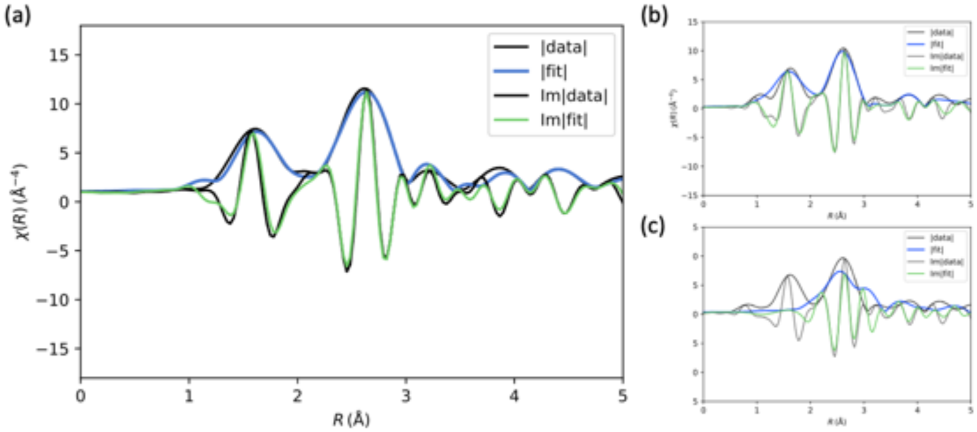

Figure 4.4. Experimental EXAFS spectra of the Pt-mix-50 sample (black), a) fit from MS-QuantEXAFS using both Pt-iso/MgO and Pt-np/MgO, b) using only the Pt-iso/MgO structure and c) using only the Pt-np/MgO structure.

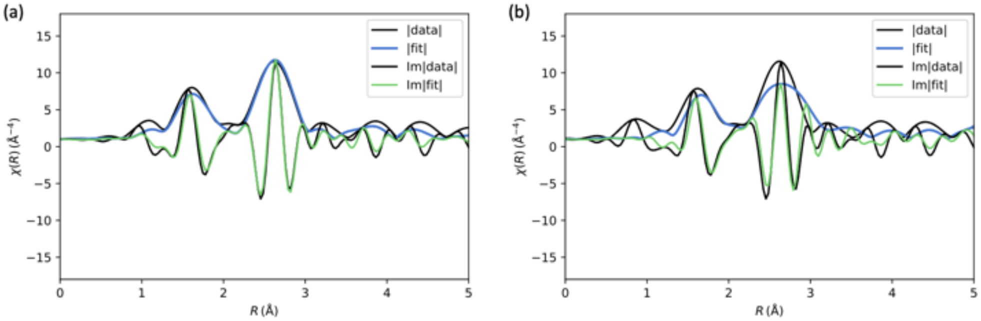

Figure 4.5. Experimental EXAFS data obtained for PM Pt-np/MgO 50% samples and EXAFS fit in R-space magnitude of the Fourier transform using a) [100]/sub0/$*O_2$, and b) [310]/pos1/$*O_2$ model of Pt-iso/MgO; the k-range used in the fits was 2.2–12 Å^{-1} and the R-range is 1.0–5.0 Å.

used in the fitting. Here, we repeat the above analysis with Pt-mix-50, but instead of the Pt-subsurface site-1 Figure 4.1, we use surface Pt-iso ([100]/sub0/*O_2) and Pt-iso at the MgO steps (i.e., [310]/pos1/*O_2 structure) as inputs (see Figure 4.S4). Our results show that neither structure captures the experimental spectra accurately or the correct site-fractions of the mixed sample.

Specifically, although the Pt-iso surface site (Figure 4.S4 a, [100]/sub0/*O_2) gives a reasonable overall fit (Figure 4.5 a), this analysis incorrectly estimates that 86% contributions arise from the Pt-iso site (the ground truth is 50%) and also results in unrealistic values σi^2 for Pt-iso. In fact, the performance of the step Pt-iso site is even worse. Here, the predicted contributions of Pt-iso are better (i.e., 57 wt% for [310]/pos1/*O2 structure.) However, both the R-space plot (Figure 4.5 a and 4.5b) and the fit parameters indicate that this site is unlikely to be present in the experimental sample.

It is important to note that both the quality of fit (measured by R-factor or reduced χ^2) and reasonable values of the fit parameters must be carefully considered while performing a MS-QuantEXAFS analysis. Even if reasonable agreement between the fit spectra and the experimental measurements is observed, illogical values of the fit parameters (e.g., σi^2 for surface Pt-iso) suggest that other possible structures, in our case Pt-iso structures, should be explored.

In addition to the above site-sensitivity analysis, we also studied the sensitivity of the procedure to the coordination numbers of the Pt-np. Here, we fix the coordination number for Pt-iso sites (50 wt%, optimized parameters in Table 4.1), and plot the simulated spectra for using several different fixed values of CN_{np}p. We use CN_{np}=1,3,6 and 9, where CN_{np}=9.2 corresponds to the experimental Pt-np sample. Thus, in this analysis, the contributions from Pt-np only depend on the values of σ^2_{np}, which represents the thermal disorder for Pt-Pt scattering paths.

As summarized in Figure 4.6, we find that reasonable fits are observed for all values of CN_{np}. However, as highlighted in Table 4.1 (marked in red text), the $\sigma_n p^2$,values become non-sensical especially for multiple scattering paths within 3.1–3.5 Å. This is because, in addition to the metallic Pt–Pt scattering paths (which originate from Pt-np), the 3.1–3.5 Å region also includes contributions from the Pt–Mg paths from the Pt-iso site. Thus, as the weight fractions of the two sites and CNs of the Pt-iso are fixed, our Fréchet distance analysis (which measures of similarity between two curves) shows a high-confidence in its predictions for site fractions.

Note that an inverse study, where the contributions of the Pt-nps are held constant, is not possible as the CNs of the Pt-iso sites, which are obtained from DFT, are not allowed to change. In summary, the above sensitivity analyses suggests that while the MS-QuantEXAFS algorithm will generally provide reasonable fits in several scenarios (as additional degrees of freedom are introduced), obtaining reliable physical insights (e.g., site-fractions and structural information) requires careful analysis of the fitting parameters.

Table 4.1. EXAFS fit parameters for fixed CN_{np} = 1,3,6,9 for the first Pt-Pt coordination shell (fits are shown in Figure 4.6).

CN	Np(%)	Pt–O path*	Pt–O–Mg path*	MS paths*	Pt–Pt first path*
1	60.2	0.005	0.099	5.7×10^{-12}	0.097
3	46.0	0.003	0.015	2.2×10^{-13}	0.003
6	45.9	0.004	0.099	2.2×10^{-15}	0.006
9	60.6	0.002	0.013	0.002	0.008

Note: * denotes the σ_i^2 (Å^2) values represent the Debye-Waller factors for each of the scattering paths mentioned and MS denotes multiple scattering.

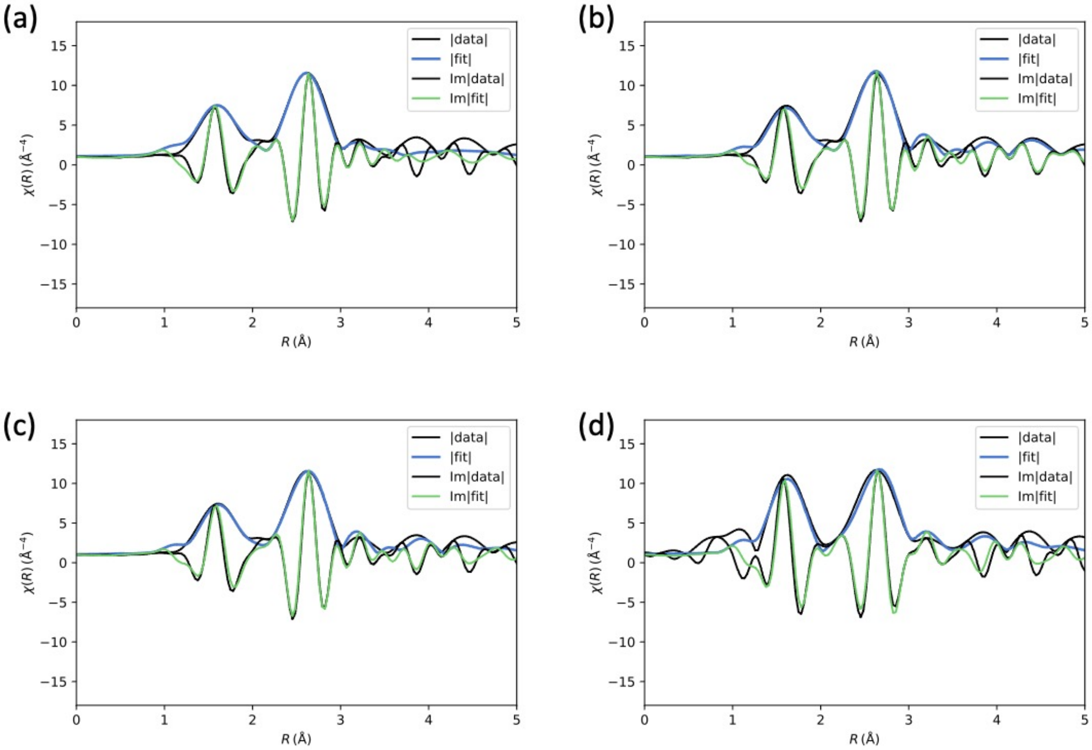

Figure 4.6. EXAFS fits in R-space magnitude of the Fourier transform for Pt-np/MgO 50% for fixed $CN_{\mathrm{np}} = 1, 3, 6, 9$ for the first Pt-Pt coordination shell; the k-range used in the fits was 2.2–12 Å^{-1}, and the R-range is 1.0–5.0 Å.

Extension to other Pt-mix-X catalysts Having established the robustness and sensitivity of the proposed approach and tested it on different fractions of physically mixed Pt-iso/MgO and Pt-np/MgO , Figure 4.7, we now explore the generalizability of this MS-QuantEXAFS to the other Pt-mix/MgO materials in our study. As summarized in Figure 4.7, MS-QuantEXAFS successfully reproduces the experimental weight fractions for our entire experimental dataset. As recommended above, chart 4.3 shows that values of the fitting parameters remain reasonable. MS-QuantEXAFS was more accurate in predicting the site fractions with an error of ±5%. While the model was fairly accurate in quantifying the fractions of the sites, the prediction of χ_{-}(Pt-mix) needed further analysis to account for accuracy. A statistical analysis of the dependence of χ_{-}(Pt-mix) when used as a multiplier to the fractional term is shown in Figure 5. This method is more robust and can be used in multiple iterations of different plausible structures selected to be representative of the experimental sample based on structure stability that can be evaluated using DFT and realistic (but not perfect) EXAFS fits.

We also reversed the above fitting approach. Specifically, we fixed the wt% of the Pt-np to ‘XX’ values (where ‘XX’ was the known fraction of Pt-np/MgO mixed with Pt-iso/MgO) and attempted to fit the coordination number for the first shell of the Pt-np across all the Pt-mix-X samples. The predicted CN_{np} values (i.e., 9.7 ± 1.2) are in close agreement with the ground truth (i.e., 9.2 ± 1.3) obtained from the conventional EXAFS analysis of the pure sample. This shows coordination numbers can be predicted based on site fractions or vice versa – this is important is cases when non-homogeneous distributions of nanoparticle sizes are expected. However, the CNs for Pt-np are predicted with a large error in the fit report as we decrease the fractions of the NPs. Hence the value of CN corresponding to 0% Pt-np is 9 ± 11 from the EXAFS fits and this is an outlier data point. However, this effect comes from the fact that the fractions are direct multipliers to the CN in the site-fractions code. Hence, even though the code predicts the fractions accurately ($R^2 = 0.996$), it has a lower efficiency in predicting CN_{np} with ($R^2 = 0.197$) and hence the fractions predicted need to be multiplied to the CN_{np} values to get the scaled values of CN_{np} which is much accurate ($R^2 = 0.997$).This analysis is shown in Figure 4.8.

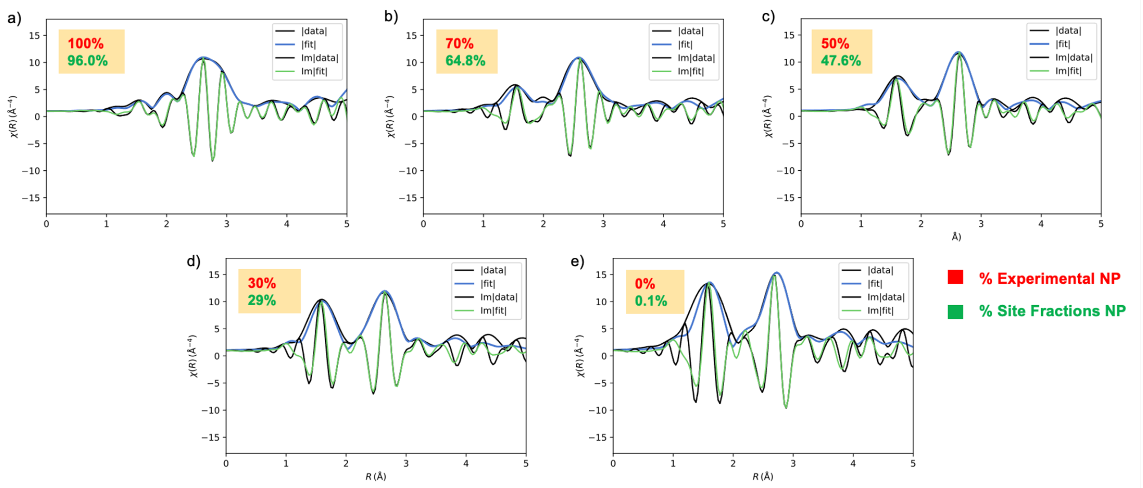

Figure 4.7. EXAFS R-space magnitude of the Fourier transform for PM Pt-np/MgO and Pt-iso/MgO data and model; the k-range used in the fits was 3.0–11.8 Å^{-1} and the R-range is 1.0–5.0 Åfor a) 100% (pure) Pt-np/MgO, b) 70% Pt-np/MgO and 30% Pt-iso/MgO, c) 50% Pt-np/MgO and 50% Pt-iso/MgO, d) 30% Pt-np/MgO and 70% Pt-iso/MgO, and e) 100% (pure) Pt-iso/MgO.

Transferability of MS-QuantEXAFS to other materials. To demonstrate the generalizability of this approach, we have extended this study to other atomically dispersed systems including simulated Pt-iso/MgO (simulated spectra) and Pt-iso/TiO_2. Here, we considered the Pt-iso/TiO_2 catalysts from Finzel et al.[26] and simulated Pt-np/MgO and Pt-iso/MgO data. Apart from the benchmarked system presented in Figure 4.7, the site fractions of more simulated data of Pt-iso/TiO_2 and Pt-np were tested using site fractions and the results are presented in the Figure 4.S5 with the sample details in Table 4.S4. Additional datasets, with different mixes

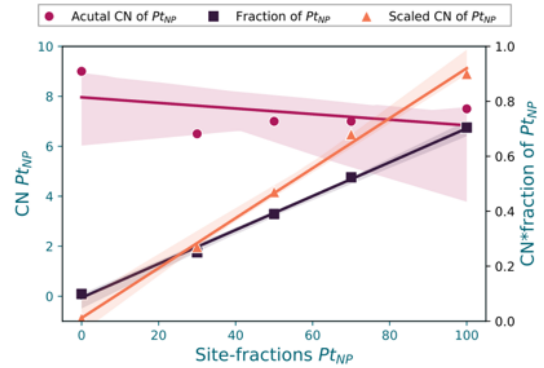

Figure 4.8. Statistical analysis of the dependence of predicted CN_{np}.

of spectra were simulated from the experimental data collected on Pt-iso/MgO and Pt-np/MgO system; and MS-QuantEXAFS was used to predict the fractional contributions. The results are included in the SI (Figure 4.S6) with sample details in Table 4.S5. In all cases, the predicted site fractions from MS-QuantEXAFS captured the composition and structures of the mixed samples.

4.4 Conclusion

Several recent studies have illustrated the challenges associated with the characterization of atomically dispersed catalysts. Within this community, conventional EXAFS analysis has been typically used to obtain the averaged local coordination around the absorbing atom. The conventional fitting approach, however, may be confounded by the presence of small quantities of metallic or oxides phases in the experimental sample. To address the above challenges, here, we have extended the previously reported QuantEXAFS approach to facilitate simultaneous fitting of multiple distinct sites. The resulting strategy (denoted as MS-QuantEXAFS) was experimentally validated using known physical mixtures of Pt-iso/MgO and Pt-np/MgO catalysts. Impressively, we show that MS-QuantEXAFS can quantitatively predict the composition and structural properties of the Pt-iso and Pt-np sites that are present the mixed catalyst samples. Importantly, our detailed numerical analysis shows that MS-QuantEXAFS is robust and sensitive to the structure of the Pt-iso site (which is obtained from DFT) used in the fitting procedure. While lower accuracies are expected for CN_np (due to creation of non-linear terms within the fitting equations), careful analysis coupled of fitting parameters can be used to overcome this limitation. We have also demonstrated the generalizability of this approach to other materials such as Pt/TiO_2 and Pd/MgO. Thus, in summary, we anticipate that the proposed MS-QuantEXAFS approach will expand the scope of how theory can be used to quantitatively guide the structural interpretation of complex catalyst materials where conventional EXAFS analysis remains limited

4.5 References

[1] Simon Mitchell and Javier Pérez-Ramírez. Single atom catalysis: A decade of stunning progress and the promise for a bright future. *Nature Communications*, 11(1):10–12, 2020. doi: 10.1038/s41467-020-18182-5.

[2] Yujing Lu, Chun-Teh Kuo, Libor Kovarik, Adam S. Hoffman, Alexey Boubnov, David M. Driscoll, John R. Morris, Simon R. Bare, and Ayman M. Karim. A versatile approach for quantification of surface site fractions using reaction kinetics: The case of CO oxidation on supported Ir single atoms and nanoparticles. *Journal of Catalysis*, 378:121–130, 2019. doi: 10.1016/j.jcat.2019.08.023.

[3] Leo DeRita, Joaquin Resasco, Sheng Dai, Alexey Boubnov, Ho Viet Thang, Adam S Hoffman, Insoo Ro, George W Graham, Simon R Bare, Gianfranco Pacchioni, Xiaoqing Pan, and Phillip Christopher. Structural evolution of atomically dispersed Pt catalysts dictates reactivity. *Nature Materials*, 18(7):746–751, 2019. doi: 10.1038/s41563-019-0349-9.

[4] Joaquin Resasco, Leo Derita, Sheng Dai, Joseph P. Chada, Mengen Xu, Xiaoyue Yan, Joshua Finzel, Steve Hanukovich, Adam S. Hoffman, George W. Graham, Simon R. Bare, Xiaoqing Pan, and Phillip Christopher. Uniformity is key in defining structure-function relationships for atomically dispersed metal catalysts: The case of Pt/CeO_2. *Journal of the American Chemical Society*, 142 (1):169–184, 2020. doi: 10.1021/jacs.9b09156.

[5] Bruce C. Gates. Atomically dispersed supported metal catalysts: Seeing is

believing. *Trends in Chemistry*, 1(1):99–110, 2019. doi: 10.1016/j.trechm.2019.01.004.

[6] Yizhen Chen, Rachita Rana, Tyler Sours, Fernando D. Vila, Shaohong Cao, Thomas Blum, Jiyun Hong, Adam S. Hoffman, Chia-Yu Fang, Zhennan Huang, Chunyan Shang, Chuanhao Wang, Jie Zeng, Miaofang Chi, Coleman X. Kronawitter, Simon R. Bare, Bruce C. Gates, and Ambarish R. Kulkarni. A theory-guided x-ray absorption spectroscopy approach for identifying active sites in atomically dispersed transition-metal catalysts. *J. Am. Chem. Soc.*, 143(48): 20144–20156, 2021. doi: 10.1021/jacs.1c07116.

[7] Louise M. Debefve, Adam S. Hoffman, Alexander J. Yeh, Ron C. Runnebaum, Sarah Shulda, Ryan M. Richards, Ilke Arslan, and Bruce C. Gates. Iridium atoms bonded to crystalline powder MgO: Characterization by imaging and spectroscopy. *J. Phys. Chem. C*, 124(1):459–468, 2020. doi: 10.1021/acs.jpcc.9b08592.

[8] Xin Tao, Bing Nan, Yunan Li, Meng Du, Ling ling Guo, Chen Tian, Luozhen Jiang, Lu Shen, Nannan Sun, and Li-Na Li. Highly active isolated single-atom Pd catalyst supported on layered MgO for semihydrogenation of acetylene. *ACS Appl. Energy Mater.*, 2022. doi: 10.1021/acsaem.2c02076.

[9] Yizhen Chen, Rachita Rana, Zhennan Huang, Fernando D. Vila, Tyler Sours, Jorge E. Perez-Aguilar, Xiao Zhao, Jiyun Hong, Adam S. Hoffman, Xu Li, Chunyan Shang, Thomas Blum, Jie Zeng, Miaofang Chi, Miquel Salmeron, Coleman X. Kronawitter, Simon R. Bare, Ambarish R. Kulkarni, and Bruce C. Gates. Atomically dispersed platinum in surface and subsurface sites on MgO

have contrasting catalytic properties for CO oxidation. *J. Phys. Chem. Lett.*, 2022. doi: 10.1021/acs.jpclett.2c00667.

[10] Bidyut B Sarma, Philipp N Plessow, Giovanni Agostini, Patricia Concepción, Norbert Pfänder, Liqun Kang, Feng R Wang, Felix Studt, and Gonzalo Prieto. Metal-specific reactivity in single-atom catalysts: CO oxidation on 4d and 5d transition metals atomically dispersed on MgO. *J. Am. Chem. Soc.*, 142(35): 14890–14902, 2020. doi: 10.1021/jacs.0c03627.

[11] John Jones, Haifeng Xiong, Andrew T. Delariva, Eric J. Peterson, Hien Pham, Sivkumar R. Challa, Gongshin Qi, Se Oh, Michelle H. Wiebenga, and Abhaya K. Datye. Thermally stable single-atom platinum-on-ceria catalysts via atom trapping. *Science*, 353(6295):150–154, 2016. doi: 10.1126/science.aaf8800.

[12] Noah Felvey, Jiawei Guo, Rachita Rana, Le Xu, Simon R. Bare, Bruce C. Gates, Alexander Katz, Ambarish R. Kulkarni, Ron C. Runnebaum, and Coleman X. Kronawitter. Interconversion of atomically dispersed platinum cations and platinum clusters in zeolite ZSM-5 and formation of platinum gem- dicarbonyls. *J. Am. Chem. Soc.*, 144(30):13874-13887, 2022. doi: 10.1021/jacs.2c05386.

[13] Long Kuai, Zheng Chen, Shoujie Liu, Erjie Kan, Nan Yu, Yiming Ren, Caihong Fang, Xingyang Li, Yadong Li, and Baoyou Geng. Titania supported synergistic palladium single atoms and nanoparticles for room temperature ketone and aldehydes hydrogenation. *Nat. Commun.*, 11(1):1–9, 2020. doi: 10.1038/s41467-019-13941-5.

[14] John C. Matsubu, Vanessa N. Yang, and Phillip Christopher. Isolated metal active site concentration and stability control catalytic CO_2 reduction selectivity. *J. Am. Chem. Soc.*, 137(8):3076–3084, 2015. doi: 10.1021/ja5128133.

[15] Mathew Newville. Larch: An analysis package for XAFS and related spectroscopies. *J. Phys. Conf. Ser.*, 430(1):0–7, 2013. doi: 10.1088/1742-6596/430/1/012007.

[16] Baraa Werghi, Liheng Wu, Amani M. Ebrahim, Miaofang Chi, Haoyang Ni, Matteo Cargnello, and Simon R. Bare. Selective catalytic behavior induced by crystal-phase transformation in well-defined bimetallic Pt-Sn nanocrystals. *Small*, 19(20):2207956–2207965, 2022. doi: 10.1002/smll.202207956.

[17] Scipy documentation. `https://docs.scipy.org/doc/scipy/reference/generated/scipy.optimize.minimize.html`, 2001. (accessed 2023-07-01).

[18] Susannah L. Scott, T. Brent Gunnoe, Paolo Fornasiero, and Cathleen M. Crudden. To err is human; to reproduce takes time. *ACS Catal.*, 12:3644–3650, 2022. doi: 10.1021/acscatal.2c00967.

[19] Vogt Charlotte and Bert M. Weckhusen. The concept of active site in heterogeneous catalysis. *Nature Chemistry Reviews*, 6:89–111, 2022. doi: 10.1038/s41570-021-00340-y.

[20] Bert M Weckhusen. Determining the active site in a catalytic process: Operando spectroscopy is more than a buzzword. *Phys. Chem. Chem. Phys*, 5:4351–4360, 2003. doi: 10.1039/b309650p.

[21] David F. Yancey, Samuel T. Chill, Liang Zhang, Anatoly I. Frenkel, Graeme Henkelman, and Richard M. Crooks. A theoretical and experimental examination of systematic ligand-induced disorder in Au dendrimer-encapsulated nanoparticles. *Chemical Science*, 4:2912–2921, 2013. doi: 10.1039/c3sc50614b.

[22] Samuel T. Chill, Rachel M. Anderson, David F. Yancey, Anatoly I. Frenkel, Richard M. Crooks, and Graeme Henkelman. Probing the limits of conventional extended x-ray absorption fine structure analysis using thiolated gold nanoparticles. *ACS Nano*, 9:4036–4042, 2015. doi: 10.1021/acsnano.5b00090.

[23] Zhiyao Duan, Yuanyuan Li, Janis Timoshenko, Samuel T. Chill, Rachel M. Anderson, David F. Yancey, Anatoly I. Frenkel, Richard M. Crooks, and Graeme Henkelman. A combined theoretical and experimental EXAFS study of the structure and dynamics of Au147 nanoparticles. *Chemical Science and Technology*, 6:6879–6885, 2016. doi: 10.1039/c6cy00559d.

[24] Joaquin Resasco, Leo DeRita, Sheng Dai, Joseph P Chada, Mingjie Xu, Xingxu Yan, Jordan Finzel, Sergei Hanukovich, Adam S Hoffman, George W Graham, Simon R Bare, Xiaoqing Pan, and Phillip Christopher. Uniformity is key in defining structure–function relationships for atomically dispersed metal catalysts: The case of Pt/CeO_2. *Journal of the American Chemical Society*, 142(1): 169–184, jan 2020. doi: 10.1021/jacs.9b09156.

[25] Igor Levin. *NIST Inorganic Crystal Structure Database (ICSD)*. NIST, 2013.

[26] Jordan Finzel, Kenzie M. Sanroman Gutierrez, Adam S. Hoffman, Joaquin Resasco, Phillip Christopher, and Simon R. Bare. Limits of detection for exafs characterization of heterogeneous single-atom catalysts. *ACS Catal.*, 13:6462–6473, 2023. doi: 10.1021/acscatal.3c01116.

4.6 Supporting Information

EXPERIMENTAL AND COMPUTATIONAL METHODS

Synthesis of Atomically dispersed Platinum in MgO support.Atomically dispersed subsurface platinum (Ptiso) was synthesized as previously reported by us [cite JACS]. Briefly, aqueous K_2PtCl_4, 20 mL of 0.25 mM solution in 40 mL of ethanol, were transferred to a beaker containing 1000 mg of MgO powder (manufacturer-specified specific surface area of 25 m2/g) and 250 mL ethanol. The resultant solid was centrifuged and dried at overnight in air in an oven at 80 °C. The dried powder was calcined until a final temperature of 700 °C was reached, which was held for 4 h in the presence of O2 (10 mL(NTP)/min) and N2 (40 mL(NTP)/min).

Synthesis of Platinum nanoparticles on MgO support.- Platinum nanoparticles (PtNP) were synthesized using Pt(acac)2 (78.7 mg), trioctylamine (10 mL), oleic acid (2.5 mL), and oleylamine (0.7 mL) in a 3-neck flask connected to lab Schlenk line. The chemicals were mixed using a magnetic stirring at room temperature and vacuum degassed (¡2 Torr) for 15 mins. In the next step, 0.05 mL of trioctylphosphine was added to the mixture and under vacuum the temperature of the flask was increased to 120 °C maintained for another 30 min to remove moisture and air. Later, N2 was introduced in the flask, and the temperature was raised to 250 °C at a rate of 15 °C/min, and maintained at 250 °C for 30 min and then cooled down to room temperature. Pt NPs obtained were isolated and precipitated in 20 mL of ethanol and 20 mL of 2-propanol, and collected via centrifugation (8000 rpm, 8 min). The NPs were washed with hexanes and acetone and redispersed in 4 mL of hexanes. The nanoparticles were then dispersed on MgO support with a loading of 0.05 wt% of Pt.

Transmission electron microscopy.Transmission electron microscopy (TEM) images of Pt nanoparticles dispersed on MgO were recorded at Stanford University on a FEI Tecnai transmission electron microscope equipped with an Orius CCD camera operating at 200 kV. STEM images of the pure isolated platinum samples were reported in our previous work 2.

XAS experimental setup. X-ray absorption spectroscopy data (XAS) was collected at beamline 9-3 in Stanford Synchrotron Radiation Lightsource (SSRL), which is a side station on a 16- pole 2-tesla wiggler beamline, the ring SPEAR3 was operated in top-offmode with a storage ring energy of 3 GeV and 500 mA stored current. A Si double-crystal (220) monochromator was detuned by 25% of maximum intensity to minimize harmonics at the platinum L3 edge. XAS data were collected in fluorescence yield mode with a 100-element germanium solid-state detector array, each sample pressed into a pellet at 25 °C. A platinum foil was placed between the transmission and reference channel ion chambers for energy calibration. A cryostat filled with liquid nitrogen was installed and the samples were loaded on the sample holder and the holder was immersed in the cryostat to diminish thermal attenuations in EXAFS signal. Known quantities of PtNP and Ptiso were mixed and pellets were made. Ex-situ EXAFS data was collected for the pellets at Pt L_III-edge.

Reproducibility of the atomically dispersed subsurface platinum site. The EXAFS of the sample was collected at three different times. Details are included in the SI along with the EXAFS fits.

XAS data analysis using QuantEXAFS. A detailed overview of our QuantEXAFS workflow with the example of the subsurface platinum site identification was illustrated in our 2021 paper. This method moves from an empirical approach for EXAFS analysis to a more structure-driven and quantitative approach. Considering we have our atoms2feff code that converts a DFT file format to a feff.inp format we are able to run FEFF calculations for all the structures on-the-fly. Motivated to further the capabilities of QuantEXAFS from homogenous sites-identification, to quantifying site heterogeneities, we developed MS-QauntEXAFS.

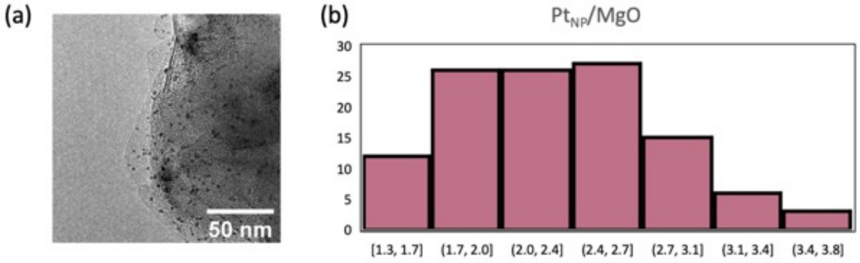

Figure 4.S1. TEM image and histogram of Pt size distribution of PtNP/MgO.

To test the reproducibility of the catalytic site formed by our recipe to synthesize atomically dispersed subsurface Pt sites the in-situ and ex-situ spectra of different samples made from the same synthesis method was collected during different beamtimes and fits are shown in Figure 4.S2.

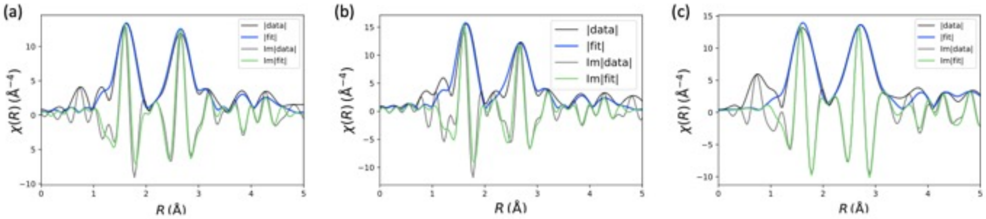

Figure 4.S2. EXAFS fits in R-space (a), (b), and (c) showing the magnitude (fit: blue, experiment: black) and imaginary portions (fit: green, experiment: black) of Fourier transforms. The k-range of 2.2-12.5 $Å^{-1}$ and the R-range of 1.0-5.0 Åwere used for the fits. The fits are based on the [100]Mg-vac/sub1 structure as shown in the main text Figure 4.1.

Table 4.S1. Experimental details of the physically mixed samples that we studied using ex-situ EXAFS to test the site fractions prediction capabilities of QuantEXAFS. The know fractions from the data as shown in the table were compared to the fractions determined from QuantEXAFS. NP(wt%) is the weight percentage of the Pt nanoparticles on MgO physically mixed with the weight percentage of the atomically dispersed Ptiso/MgO (Iso (wt%)).

Sample	NP (wt%)	Iso (wt%)
PtNP0%	0	100
PtNP30%	30	70
PtNP50%	50	50
PtNP70%	70	30
PtNP100%	100	0
PtNP30%*	30	70
PtNP50%*	50	50

[1]

---

[1] *Repeated experiments to account for reproducibility of the analysis.

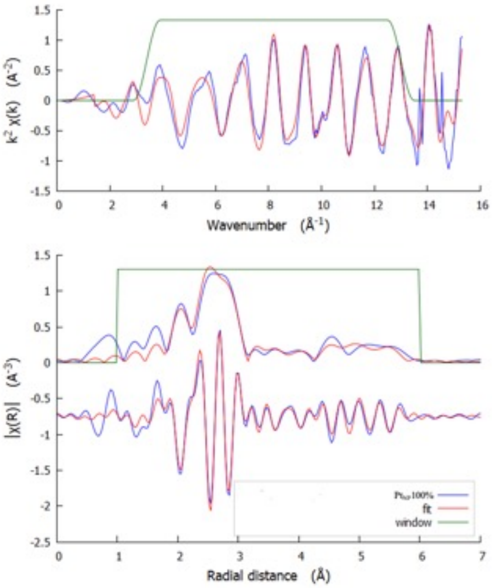

Figure 4.S3. Conventional EXAFS analysis of pure Pt nanoparticle on MgO, Pt-np/MgO (100%). R-space of 1-6 Åand k-space of 3.4-13.0 Å^{-1}.

Table 4.S2. Summary of EXAFS fit parameters characterizing pure Pt-np/MgO 100%.

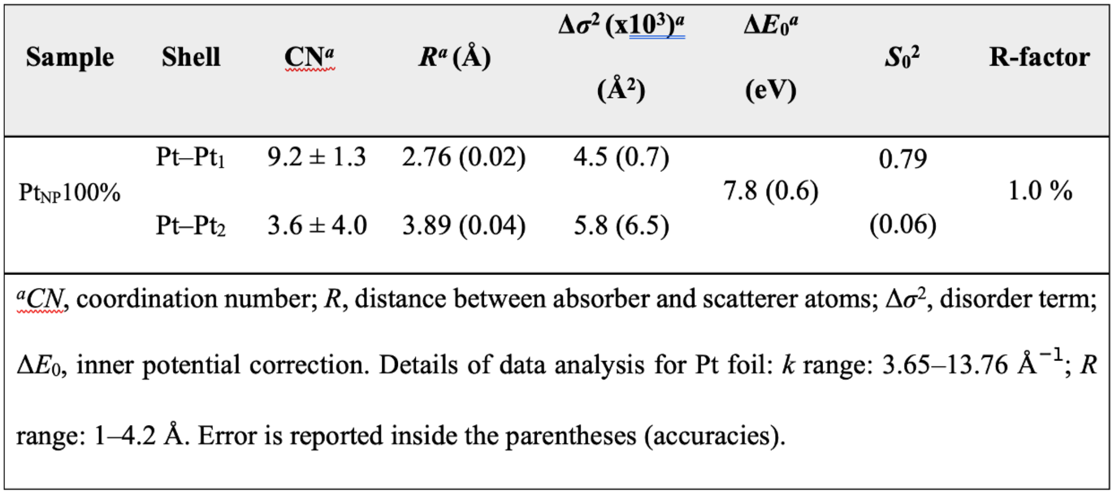

Sample	Shell	CN^a	R^a (Å)	$\Delta\sigma^2$ (x10^3)^a (Å^2)	ΔE_0^a (eV)	S_0^2	R-factor
Pt$_{NP}$100%	Pt–Pt$_1$	9.2 ± 1.3	2.76 (0.02)	4.5 (0.7)	7.8 (0.6)	0.79 (0.06)	1.0 %
	Pt–Pt$_2$	3.6 ± 4.0	3.89 (0.04)	5.8 (6.5)			

^{a}*CN*, coordination number; *R*, distance between absorber and scatterer atoms; $\Delta\sigma^2$, disorder term; ΔE_0, inner potential correction. Details of data analysis for Pt foil: *k* range: 3.65–13.76 Å^{-1}; *R* range: 1–4.2 Å. Error is reported inside the parentheses (accuracies).

Table 4.S3. Summary of hierarchical approach used to classify all possible scattering paths into five different categories. Only 9 parameters (shown in red) are optimized in the automated EXAFS analyses.

Category	**Classification criterion**	**Number of paths**	**Variables**		
1	$R_{eff} < 3.2$ Å and Pt–O scatter	6	ΔE_0	α_1	$\sigma^2_{1,Pt-O}$
2	$R_{eff} < 3.2$ Å and Pt–Mg scatter	11			$\sigma^2_{1,Pt-Mg}$
3	3.2 Å $< R_{eff} <$ 4 Å	41		α_2	σ^2_3
4	4 Å $< R_{eff} <$ 4.5 Å	58		α_3	σ^2_4
5	4.5 Å $< R_{eff} <$ 5 Å	42			σ^2_5

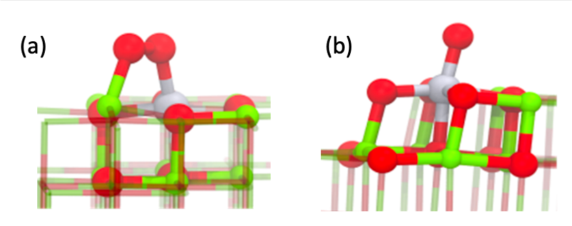

Figure 4.S4. Representative strcutures for the other thermodynamically stable a) terrace ([100]/sub0/*O_2) and b) step site ([310]/pos1/*O_2) for Pt-iso/MgO taken from the database in Chapter 2, Color scheme: magnesium (green), oxygen (red), platinum (gray).

Table 4.S4. Simulated sample details for atomically dispersed Pt/TiO_2 and Pt nanoparticle.

Sample Name	% Pt in ADCs QuantEXAFS	Target % Ptiso
1.00-ADC_Pt-Pt	100	100
0.90-ADC_Pt-Pt	86	90
0.80-ADC_Pt-Pt	74	80
0.70-ADC_Pt-Pt	64	70
0.60-ADC_Pt-Pt	55	60
0.50-ADC_Pt-Pt	46	50
0.40-ADC_Pt-Pt	37	40
0.30-ADC_Pt-Pt	28	30
0.20-ADC_Pt-Pt	19	20
0.10-ADC_Pt-Pt	10	10

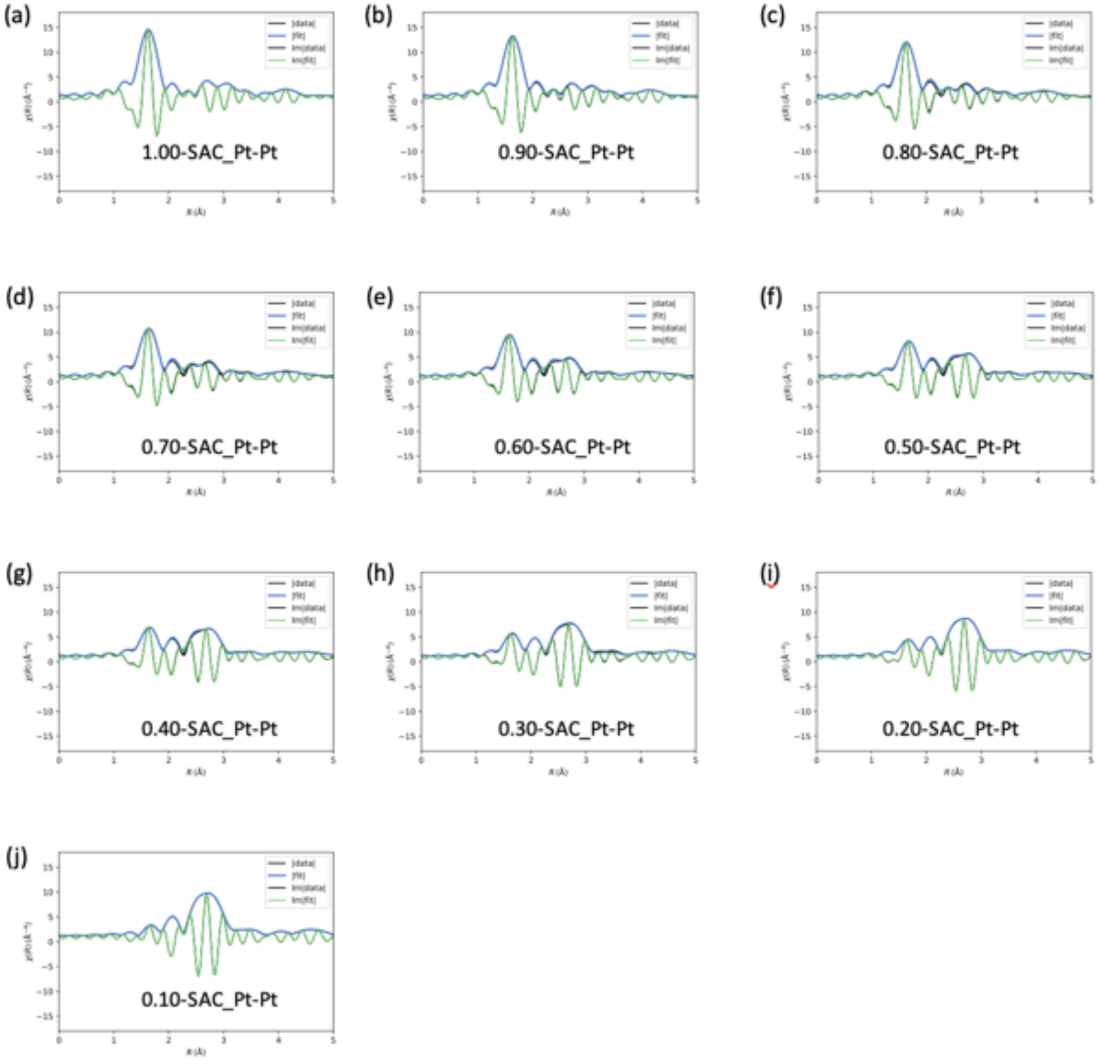

Figure 4.S5. (a-j) EXAFS fits of the data from Table 4.S4 in R-space showing the magnitude (fit: blue, experiment: black) and imaginary portions (fit: green, experiment: black) of Fourier transforms. The k-range of 3.0-11.8 $Å^{-1}$ and the R-range of 1.0-5.0 Åwere used for the fits.

Table 4.S5. Simulated sample details for atomically dispersed Pt/MgO and Pt nanoparticle.

Sample Name	% Pt in ADCs QuantEXAFS	Target % Ptiso
1.00-ADC_Pt-Pt	91	100
0.90-ADC_Pt-Pt	88	90
0.80-ADC_Pt-Pt	78	80
0.70-ADC_Pt-Pt	69	70
0.60-ADC_Pt-Pt	67	60
0.50-ADC_Pt-Pt	59	50
0.40-ADC_Pt-Pt	50	40
0.30-ADC_Pt-Pt	39	30
0.20-ADC_Pt-Pt	28	20
0.10-ADC_Pt-Pt	19	10

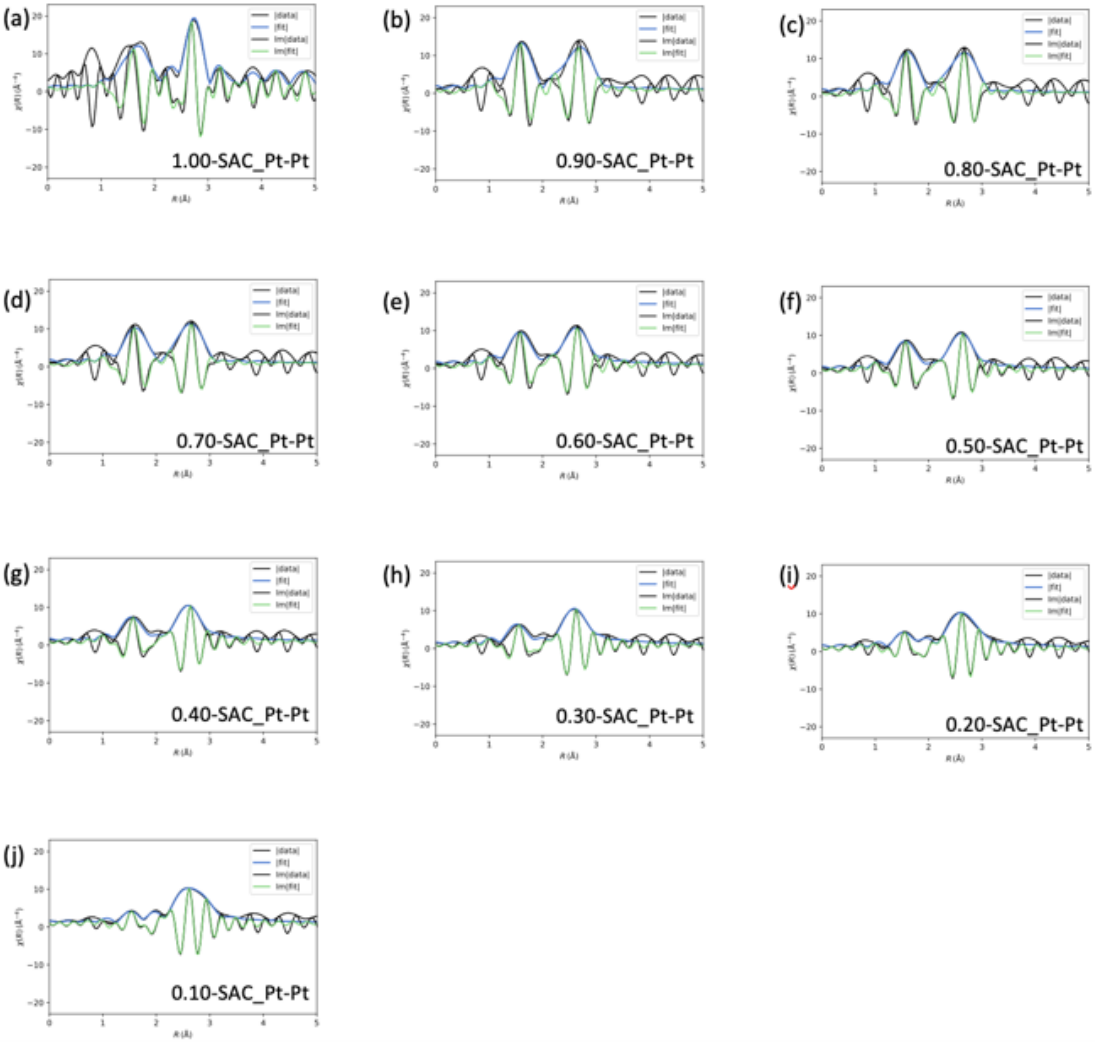

Figure 4.S6. (a-j) EXAFS fits of the data from Table 4.S5 in R-space showing the magnitude (fit: blue, experiment: black) and imaginary portions (fit: green, experiment: black) of Fourier transforms. The k-range of 3.0-11.8 Å^{-1} and the R-range of 1.0-5.0 Åwere used for the fits.

Chapter 5

Summary and Future Directions

5.1 Overall summary

This dissertation employs a collaborative computational and experimental approach to explore the structure-function characteristics of precisely synthesized catalytic systems, particularly atomically dispersed catalysts. A significant contribution from this study is the development of QuantEXAFS, an automated EXAFS analysis tool utilizing quantum chemistry calculations (DFT, MD, etc.) for a quantitative assessment of EXAFS data. This method proves highly beneficial for scenarios where a precise understanding of catalytic sites is crucial. Utilizing atomistic simulations for catalytic site identification enhances the study's depth, facilitating reaction barrier calculations and other theoretically driven analyses. This approach surpasses conventional guesswork based on averaged information, providing a more accurate representation of catalytic sites. Specifically, the study discussed in Chapter 2 successfully employed various techniques, including STEM, IR spectroscopy, XAS, XPS, and others, in conjunction with theoretical calculations, leading to the identification of a challenging-to-discern site: atomically dispersed subsurface platinum supported on MgO.

The research conducted highlights the effectiveness of a comprehensive investigation and cross-validation of hypothesized sites, particularly when employing an extensive library of DFT structures. This approach allows for a detailed understanding of the binding environment and stabilities of catalytic sites, utilizing phase diagrams and Boltzmann fractions. In this Chapter 5, a succinct summary of conclusions and the broader implications of this research is presented, accompanied by suggestions for future research directions.

5.2 General Conclusions

In this dissertation, we have employed a multi-faceted approach—utilizing well-defined, uniformly synthesized, atomically dispersed catalysts, alongside DFT calculations and XAS, specifically—to understand the structure-function relationship.[1] Additionally, we studied the impact of synthesis conditions, such as temperature, injection time of the metal precursor, and the effect of weight loadings, using both DFT and experimental approaches. Beamtime experiments at SSRL were conducted to gain insights into the applicability of the QuantEXAFS code, seeking its scientific merit for atomically dispersed catalysts.

- Our motivation to bridge the gap between the computational catalysis and experimental (XAS) community was conveyed through a perspective article 1.[2] This article addressed current knowledge gaps and future prospects for the synchrony between theory and XAS, emphasizing the importance of data sharing and reproducibility, with a focus on DFT and XAS results. Significant contributions from the field were discussed, with a focus on accelerating techniques to better understand catalytic systems.

- Recognizing the relevance of the two communities working together, we developed the QuantEXAFS tool,[3] utilizing a database of DFT-optimized structures for one-to-one mapping of experimental EXAFS data with models from DFT structures. This method was tested on Pt/MgO, and the details are discussed in Chapter 2. Employing multiple techniques, we identified the actual catalytic site, facilitating the study of probe reactions such as CO oxidation, ethylene hydrogenation, and complex reactions like propelyne epoxidation using this well-defined catalyst. Exhaustive characterization and computational studies demonstrated how multiple techniques can lead to converging results with accurate site identification.

- The next step was to understand the dynamic evolution of these atomically dispersed catalysts. A subsequent study using Pt/MgO, where the calcination temperature was varied, helped identify the impact of different synthesis parameters on the Pt atom's anchoring to the MgO support. When Pt/MgO was calcined at a lower temperature (400°C), the Pt atom was in the surface layer of MgO and was active for CO oxidation, unlike the subsurface Pt.[4] The major finding of this work was published and is presented in Chapter 3. As a side project, an exhaustive theory-driven screening was conducted to predict the diffusion of all transition metals (TMs) in the periodic table to the unique subsurface site in the lattice of MgO. It was found that the atomic radii of the TM, the oxidation state of the metal, along with its interaction with the lattice O_2 atoms, played a key role in defining site formation.

- As a step towards adding more capabilities to QuantEXAFS, XANES analysis code, a theoretical calculation of Debye-Waller factors workflow, and quantitative probing of site heterogeneities in catalysts were developed. Chapter 4 presents the key capabilities and bench-marking of the multi-site (MS) Quant-

EXAFS code that predicts the site heterogeneities in catalytic systems. The D-W factor code can be used in combination with DFT calculations to create a dynamic matrix, the theoretically calculated D-W can be compared to the experimentally fitted EXAFS disorder parameter (σ^2). This is extremely valuable in the simulation of EXAFS spectra.

- As part of side projects, the application of QuantEXAFS was tested on multiple systems, such as atomically dispersed Pd/MgO, Mo/ZSM5, Pt/ZSM5, and Ni/MgO. All these studies provided insights into the dynamic site evolution and helped predict the properties of the sites using theory. In addition to addressing the important scientific question, these studies provided proof of concept that methods like QuantEXAFS are robust. Depending on the catalytic system studied, these methods can be leveraged to extract important information, such as the spatial orientation to atoms, rather than just the average coordination numbers and average bond distances.

- This work presents a unique platform for understanding catalytic systems, using engineered sites from controlled synthesis and detailed characterization to theory-driven insights. Different examples, ranging from using TMs (atomically dispersed) in/on MgO to using a variety of supports, were used to demonstrate the applicability of the method we developed— QuantEXAFS. The mechanistic insights gained were important and were only possible due to the identification of the specific catalytic sites. Challenges pertaining to site heterogeneities were addressed by adding new capabilities to QuantEXAFS (MS-QuantEXAFS). These findings open the doors to design and understand catalytic systems with targeting properties and their operando evolution under reaction conditions, using techniques like XAS.

5.3 Outlook on Future Research

This research is dedicated to developing a quantitative method for XAS data analysis using quantum chemistry tools, namely QuantEXAFS, and evaluating its applicability. QuantEXAFS holds significant potential for a wide range of catalytic studies, making it imperative to explore and enhance its capabilities continually. However, it is crucial to acknowledge the limitations concerning the catalytic systems suitable for study using QuantEXAFS. Care must be taken to avoid overfitting models or misunderstanding XAS concepts, emphasizing scrutiny of fit parameters, DFT calculations, and model sensitivity to generated scattering paths. Additionally, meticulous preprocessing of XAS data and thorough examination at each step are essential despite QuantEXAFS handling much of the data fitting.

Atomically dispersed catalysts offer invaluable insights into various catalytic reactions,[5–9] and this work showcases numerous examples of detecting active sites, spectators, and minority species, which can be active sites in specific cases. Tools like QuantEXAFS enable the exploration of catalytic reactions using uniformly synthesized atomically dispersed or small metal cluster catalysts. There is potential for testing these materials in industrially relevant reactions, improving catalyst performance, and gaining deeper insights into issues such as catalyst selectivity and deactivation. Furthermore, conducting a comprehensive synthesis study to validate DFT predictions and understand the impact of synthesis parameters on site formation in atomically dispersed catalysts can contribute to predictive site synthesis.

In conclusion, QuantEXAFS emerges as a powerful tool with substantial advantages for the catalysis community. The development of a user-friendly packaged version accessible to non-theory audiences would enhance its utility. Active development, expanding its applicability to diverse systems, and increased utilization of the code will prove beneficial for both the catalysis and XAS user communities.

References

[1] Leo DeRita, Joaquin Resasco, Sheng Dai, Alexey Boubnov, Ho Viet Thang, Adam S Hoffman, Insoo Ro, George W Graham, Simon R Bare, Gianfranco Pacchioni, Xiaoqing Pan, and Phillip Christopher. Structural evolution of atomically dispersed Pt catalysts dictates reactivity. *Nature Materials*, 18(7):746–751, 2019. doi: 10.1038/s41563-019-0349-9.

[2] Rachita Rana, Fernando D. Vila, Ambarish R. Kulkarni, and Simon R. Bare. Bridging the gap between the x-ray absorption spectroscopy and the computational catalysis communities in heterogeneous catalysis: A perspective on the current and future research directions. *ACS Catalysis*, 12(22):13813–13830, 2022. doi: 10.1021/acscatal.2c03863.

[3] Yizhen Chen, Rachita Rana, Tyler Sours, Fernando D. Vila, Shaohong Cao, Thomas Blum, Jiyun Hong, Adam S. Hoffman, Chia-Yu Fang, Zhennan Huang, Chunyan Shang, Chuanhao Wang, Jie Zeng, Miaofang Chi, Coleman X. Kronawitter, Simon R. Bare, Bruce C. Gates, , and Ambarish R. Kulkarni. A theory-guided x-ray absorption spectroscopy approach for identifying active sites in atomically dispersed transition-metal catalysts. *J. Am. Chem. Soc.*, 143(48): 20144–20156, 2021. doi: 10.1021/jacs.1c07116.

[4] Yizhen Chen, Rachita Rana, Zhennan Huang, Fernando D. Vila, Tyler Sours, Jorge E. Perez-Aguilar, Xiao Zhao, Jiyun Hong, Adam S. Hoffman, Xu Li, Chunyan Shang, Thomas Blum, Jie Zeng, Miaofang Chi, Miquel Salmeron, Coleman X. Kronawitter, Simon R. Bare, Ambarish R. Kulkarni, and Bruce C. Gates. Atomically dispersed platinum in surface and subsurface sites on MgO have contrast-

ing catalytic properties for CO oxidation. *J. Phys. Chem. Lett.*, 2022. doi: 10.1021/acs.jpclett.2c00667.

[5] Joaquin Resasco, Leo Derita, Sheng Dai, Joseph P. Chada, Mengen Xu, Xiaoyue Yan, Joshua Finzel, Steve Hanukovich, Adam S. Hoffman, George W. Graham, Simon R. Bare, Xiaoqing Pan, and Phillip Christopher. Uniformity is key in defining structure-function relationships for atomically dispersed metal catalysts: The case of Pt/CeO_2. *Journal of the American Chemical Society*, 142(1):169–184, 2020. doi: 10.1021/jacs.9b09156.

[6] Bruce C. Gates. Atomically dispersed supported metal catalysts: Seeing is believing. *Trends in Chemistry*, 1(1):99–110, 2019. doi: 10.1016/j.trechm.2019.01.004.

[7] Simon Mitchell and Javier Pérez-Ramírez. Single atom catalysis: A decade of stunning progress and the promise for a bright future. *Nature Communications*, 11(1):10–12, 2020. doi: 10.1038/s41467-020-18182-5.

[8] John Jones, Haifeng Xiong, Andrew T. Delariva, Eric J. Peterson, Hien Pham, Sivakumar R. Challa, Gongshin Qi, Se Oh, Michelle H. Wiebenga, Xavier Isidro Pereira Hernández, Yong Wang, and Abhaya K. Datye. Thermally stable single-atom platinum-on-ceria catalysts via atom trapping. *Science*, 353(6295): 150–154, 2016. doi: 10.1126/science.aaf8800.

[9] Bidyut Bikash Sarma, Philipp N. Plessow, Giovanni Agostini, Patricia Concepción, Norbert Pfänder, Liqun Kang, Feng Ryan Wang, Felix Studt, and Gonzalo Prieto. Metal-specific reactivity in single-atom catalysts: CO oxidation on 4d and 5d transition metals atomically dispersed on MgO. *J. Am. Chem. Soc.*, 142(35):14890–14902, 2020. doi: 10.1021/jacs.0c03627.